3D SHAPE ANALYSIS: CONSTRUCTION, CLASSIFICATION AND MATCHING

DISSERTATION FOR THE DEGREE OF
DOCTOR OF PHILOSOPHY IN SYSTEM ENGINEERING

SHAOJUN LIU

OAKLAND UNIVERSITY

2007

3D SHAPE ANALYSIS: CONSTRUCTION, CLASSIFICATION AND MATCHING

by

SHAOJUN LIU

A dissertation submitted in partial fulfillment of the
requirements for the degree of

DOCTOR OF PHILOSOPHY IN SYSTEM ENGINEERING

2007

Oakland University
Rochester, Michigan

APPROVED BY:

Jia Li, Ph.D., Chair	Date
Ishwar K. Sethi, Ph.D.	Date
László Lipták, Ph.D.	Date
Andrzej Rusek, Ph.D.	Date

To My Father and Mother

ACKNOWLEDGMENTS

Here I would like to thank my advisor Dr. Jia Li for her support and guidence throughout my Ph.D. research. Starting from research ABC, she lead me into this challenging area of 3D shape analysis. As an active researcher herself, she pointed me to promising directions and we frequently discussed various problems together. I benefit enormously from her insight and rich knowledge in this area. She is also a friend in life. Her kind support enables me to devote myself to research whole-heartly. Without the favorable environment she created, it would be impossible for me to do Ph.D. research.

I sincerely thank my Ph.D. advisory committee members, Dr. Ishwar K. Sethi, Dr. László Lipták, and Dr. Andrzej Rusek. Their insightful suggestions and teaching helped me to accomplish this Ph.D. research. Special thanks to Dr. Sethi for inviting me to his lab meetings and introducing me into a summer project on fetal imaging in Beaumont hospital.

I am grateful to Dr. Wesley Lee, Dr. Russel Deter and Ms. Beverley Mc Nie for their support on the fetal imaging project. I wish to express my gratitude to Dr. Mingkun Li, Dr. Jun Tan and Dingguo Chen for their help on pattern recognition techniques, and REU students Bryan Bonvallet and Nikolla Griffins for their enlightening discussions on 4D hyperspherical harmonics. I appreciate my colleague Weihong Niu for assisting me with lab environments, and Chiayang Hung in programming issues.

Last I thank my parents and my dear wife for their love, support and sacrifices on my Ph.D. research.

SHAOJUN LIU

ABSTRACT

3D SHAPE ANALYSIS: CONSTRUCTION, CLASSIFICATION AND MATCHING

SHAOJUN LIU

Chair: Jia Li, Ph.D.

Surface construction is a widely studied topic in computer graphics and vision. Polygonal meshes generated by surface construction process are extensively used in various graphic areas, such as scene rendering and texture mapping. Marching Cubes (MC) method is the most popular method in surface construction. Existing MC methods require sample values at cell vertices to be non-zero after thresholding or modify them otherwise. The modification may introduce problems to a constructed surface, such as topological changes, representation error, and preference to positive or negative values. This dissertation presents a generalized MC algorithm for surface construction. It constructs surface patches by exploring cycles in cells without changing sample values at vertices, thus allows cell vertices with zero sample values to lie on the constructed surface. The simulation results show that the proposed Zero-Crossing MC (ZMC) method better preserves topologies of implicit surfaces that pass through cell vertices and represents the surfaces more accurately. Its efficiency is comparable to existing MC methods in constructing surfaces.

As available 3D models on the Internet increase dramatically, efficiently searching relevant shape models is requested by many applications such as computer animation, computer aided design (CAD) and protein matching. Shape-based retrieval of 3D data has been an active research area in disciplines such as computer vision, mechanical engineering and chemistry. The performance of 3D shape search engine, however, is far behind that of text, such as Google search engine. A new method for

three dimensional (3D) genus-zero shape classification is proposed. It conformally maps a 3D mesh onto a unit sphere and uses normal vectors to generate a spherical normal image (SNI). Unlike Extended Gaussian Image (EGI) which has an ambiguity problem, SNI is unique for each shape. Spherical harmonics coefficients of SNIs are used as feature vectors and self-organizing map is adopted to explore the structure of a shape model database. Since the method compares only SNIs of different objects, it is computationally more efficient than methods that compare multiple 2D views of 3D objects. The experimental results show that the proposed method can discriminate collected 3D shapes very well, and is robust to mesh resolution and pose difference.

For general shape classification and matching, rotation invariant methods based on concentric spheres model (CSM) cut 3D objects along radii. As a result, components with internal rotation yield the same shape descriptor. To solve this ambiguity, we proposed a new shape descriptor using 4D hyperspherical harmonics (HSH). It maps a 3D object onto a 4D unit hypersphere without cutting the object. We adopt support vector machine (SVM) in shape classification process and integrate classification predictions into distance weights to improve shape matching performance. Experiments show that the proposed 4D HSH shape desciptor has better shape classification and matching performance over CSM descriptors at the same vector length.

TABLE OF CONTENTS

TABLE OF CONTENTS—Continued

TABLE OF CONTENTS—Continued

LIST OF TABLES

LIST OF FIGURES

CHAPTER 1

INTRODUCTION

1.1 Motivation

With the increasing computing power of modern computers, 3D graphics technologies find more and more applications in various fields. For example, 3D animation techniques can produce spectacular movie scenes that are difficult if not impossible by traditional techniques. Virtual reality graphics can help to train pilots for planes or space shuttles. In computer aided diagnose, surface construction methods can render a 3D view of specific organs based on a series of CT scans to help physicians evaluate the symptoms intuitively. The shape of physical objects can be digitalized by laser scans into shape database, from which engineers design various components using computer aided design (CAD) software.

3D graphics research covers broad areas including surface construction, shape modeling, scene rendering, animation, user interaction, shape classification and matching. 3D graphics technologies are popular topics in many subjects such as computer graphics and vision, computational geometry and image processing.

3D shape analysis is the basis for many 3D graphics technologies. For example, only with correct 3D shape model can one render a real sensed scene. This dissertation focuses on 3D surface construction, shape classification and matching in shape analysis. We will also discuss involved supporting technologies such as image segmentation, conformal mapping and pattern recognition.

1.1.1 Surface Construction

Surface construction refers to the process in which an implicit surface is constructed from 3D volumetric data. It is an inevitable step for 3D data, such as segmentation results on 3D image, to be evaluated intuitively by human eyes. Surface construction is a widely studied topic in computer graphics and computer vision. Polygonal meshes representing constructed surfaces are widely used in various areas, such as scene rendering and texture mapping. After surface construction we can derive many geometric features, such as genus, curvature, surface area and volume, which are basis for shape analysis.

An ideal surface construction should meet many requirements due to its importance. First, the original topology of an implicit surface should be preserved. In other words, the connectivity of surface parts should not be changed. Secondly, no ambiguous surface should be generated, i.e. one and only one surface can be determined from a set of volumetric data. Thirdly, the generated surface is desired to be adaptive to surface details. In other words, relative flat surface is represented by a small number of big polygons while cute or detail rich surface is constructed by more small polygons. Finally, surface construction method should be highly efficient for large volumetric data.

Many surface construction methods have been proposed, but none meets all the above requirements. Among them, marching cubes (MC) method, proposed by Lorensen and Cline in 1987, is the most popular due to its efficiency in constructing high resolution surfaces and simplicity in implementation [1]. But it also has defects, such as topological ambiguities and representation inaccuracy. Surface construction methods are being improved to meet its requirements.

1.1.2 Shape Classification and Matching

We can get 3D models through surface construction or through digitalization of physical objects by laser scan techniques. The generated 3D models are widely

used in many fields of computer graphics, such as objects in animation scenes, components in computer aided design (CAD), or protein chain in matching database. As available 3D models on the Internet increase dramatically, efficiently searching relevant shape models is desired by many applications.

Ideal shape classification and matching method should meet following requirements. Firstly, the method should find as many as possible 3D models similar to input shape and exclude dissimilar ones. Secondly, it should eliminate variance from pose difference of 3D models, such as shift, scale and rotation. Thirdly, retrieval results should be insensitive to noise, disturbance, and mesh resolutions of 3D models. Finally, a hierarchical approach is desired for 3D models in multiple resolutions. In other words, the method adopts coarse classification and matching for models in low resolution, while fine classification and matching for those in high resolution.

Shape-based retrieval of 3D data has been an active research area in disciplines such as computer vision, mechanical engineering and chemistry. The performance of 3D shape search engine, however, is far behind that of text, such as Google search engine.

1.2 Related Work

1.2.1 Surface Construction

Among many existing surface construction methods, we only review those relevant in our research in Marching Cubes (MC) methods. In the original MC method, proposed by Lorensen in 1987, Nielson and Hamann reported an ambiguous case on a cube face with two diagonally opposite positive vertices and two diagonally opposite negative vertices [1][9]. They proposed an asymptotic decider to solve the ambiguity. Chernyaev and Natarajan independently found an internal ambiguous case under trilinear interpolation in a cube interior [2][10]. Chernyaev used 33 configurations to discriminate the ambiguous cases, while Natarajan used the value of a body saddle point to solve the ambiguity. Matveyev also addressed the internal ambigu-

ity by analyzing the types of surface intersections with a cube diagonal [11]. Nielson made a comprehensive analysis of trilinear interpolation of isosurfaces, in which 56 ambiguous cases were characterized and classified into three levels [12]. And 9 cases contain triangles entirely on a cell face, which may lead to non-manifold surfaces. In the context of this dissertation, the term surface and isosurface are exchangeable to each other.

To improve representation accuracy, Lopes and Brodlie added a small number of key points in a cell interior [13]. These critical points help to represent different surface topologies including tunnels inside a cell. Theisel used cubic Bezier patches to represent exact contours of piecewise trilinear interpolation [14]. The exact contours were then modified to be globally G^1 continuous. To reduce representation error around sharp geometric features, Kobbelt et al. proposed an extended MC method by using extra information of normals [15]. And the extended MC method was adopted in adaptive grids by Ju et al. in [16]. The adaptive approaches, such as octree based methods, use a small step size around sharp geometric features while reduce the number of polygons overall [17][18][19]. For the same purpose, Montani et al. proposed a discretized MC method that merges small facets into large coplanar polygons [20][21]. And Cuno et al. adopted a hierarchical approach based on radial basis functions [22].

The MC method was originally applicable only to manifold surfaces, which are locally homomorphic to a two dimensional disk everywhere. A polygonal mesh representing a manifold surface should satisfy the continuity condition that a polygon edge should be shared by exactly two polygons, or lie in an external face of the entire volume [23]. Non-manifold surfaces, such as contacting or intersecting surfaces, contain edges of degree three, four or more. Bloomenthal and Ferguson proposed to polygonize non-manifold surfaces by decomposing a cell into tetrahedras, which requires multiple intersections per cell edge [24]. Hubeli and Gross extended fairing operations on non-manifold models in a multiresolution approach [25]. In the

context of MC method, Hege et al. used a probability interpolation model to polygonize non-manifold surfaces [26]. Their look-up table was adopted by Yamazaki et al. in a MC method based on discontinuous distance field for non-manifold surfaces [27].

However, one of the original MC assumptions, in which sample values should be nonzero after thresholding, has not been addressed by existing MC methods. In other words, it is assumed cell vertices lie either inside or outside an isosurface, not on the isosurface. Even in MC methods of non-manifold surfaces that contain multiple regions, an isosurface is still not assumed to pass through cell vertices. The assumption was introduced to ensure that the number of cases an isosurface intersects a cell could be easily enumerated. Otherwise, case enumeration in existing MC methods are incomplete and too many cases need to be added. This assumption, however, does not hold in some situations. For example, volumetric data generated by level set method may contain zero sample values, i.e. isosurface of level sets pass through grids. Integer-valued isosurfaces of integer-valued data sets or synthetic data may also meet zero sample values. In one of our experiments in the later chapter of this dissertation, the cases with zero sample values take up to 7% of total cases. Actually, the assumption to exclude zero sample values is regarded as a technical problem in [23], and one of the several major artifacts in most existing isocontour software in [28]. Zero sample values are also discussed in [29], but no specific MC method was proposed.

To handle the situation with zero samples, many existing MC methods modify zero sample values. For example, when level sets pass through grids, Han et al. changed sample values at such grid points from zero to negative [28]. This kind of modification has defects from following aspects.

First, it may introduce obvious topological changes or representation error to an isosurface, as shown in Fig. 1.1. Changing zero sample values in the top row of Fig. 1.1 to negative introduces patches as shown in the bottom row of Fig. 1.1. Thick lines in the figure represent intersections of isosurfaces and a cell face. Fur-

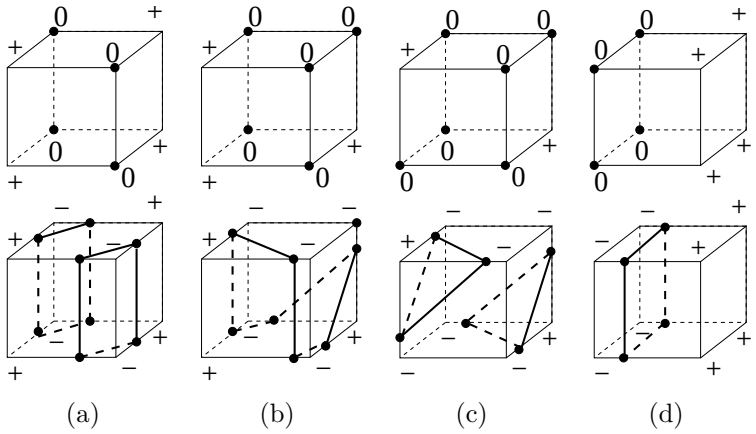

Figure 1.1: Topological changes caused by sample value modification. In each subfigure, the figure on the top shows original sample values, while the figure at the bottom shows a possible topological change.

thermore, modification on zero sample values may change surface topology from non-manifold to manifold. One example is shown in Fig. 1.2(a), in which one edge is shared by four polygons on two contacting "V" shape surfaces. The two contacting surfaces are separated after modifying sample values at contact points from zero to negative.

Finally, constructed isosurface should be neutral to either positive or negative sample values. In other words, the generated isosurface should not be changed if we multiply sample values with -1. However, modifying zero sample values introduces preference on positive or negative values and leads to two different topological results. For example, if the positive sample values in the top row of Fig. 1.1 are negative instead, the same modification in Fig. 1.1 does not introduce any new patches. In Fig. 1.2(b), the two "V" shape surfaces contacting from top and bottom are merged into one after the same modification, when the sample values in Fig. 1.2(a) are multiplied with -1.

One might argue that zero sample values might be treated as negative without modification. Nevertheless, it introduces degenerated patches in Fig. 1.1(a) and 1.1(b) where patch vertices or edges converge. Enumerating all the possibilities of

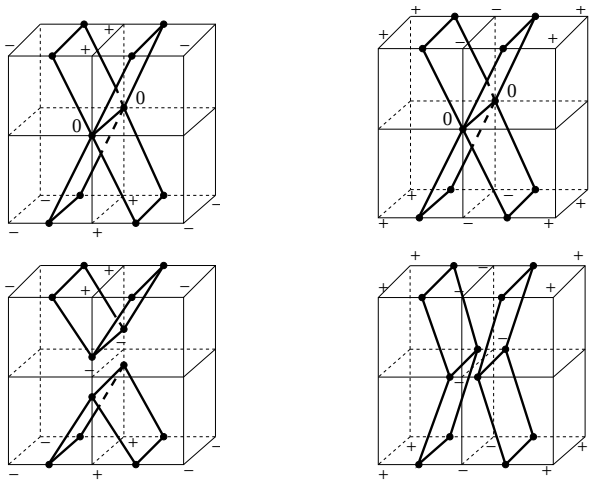

Figure 1.2: Topologies inconsistency caused by modifying sample values at contact points from zero to negative in existing MC method.

degenerated patches in MC cases is also tedious. And it still brings obvious topologic changes to Fig. 1.1(b), 1.1(c) and 1.1(d).

This dissertation proposes a more general MC method that does not modify sample values. It constructs isosurfaces by exploring cycles in two dimensions to avoid enumerating all the cases directly [30]. We adopt bilinear interpolation and introduce zero vertex, zero edge and zero face to solve ambiguous cases. The proposed method is also applicable to some non-manifold surfaces.

1.2.2 Shape Classification and Matching

The comparison of shape similarity is the basis for shape recognition, classification and matching. In retrospect, similarity comparison methods have evolved from 2D to 3D. 2D methods discriminate shapes based on 2D contours obtained at different viewing angles. Most of them can not be generalized to 3D shape matching directly. On the other hand, 3D methods extract shape features from 3D models to match similar models [31]. Many survey papers summarized the development of 3D

shape comparison techniques [32][31][33]. As a large mount of 3D methods exist and belong to various classes, we just mention a few related to our research.

Methods based on shape distribution enjoy the benefits of invariant properties and distinguish models in broad categories well. For example, shape distribution method, proposed by Osada et al., is robust to translations, rotations, scales, mirrors, and tessellations [5]. However, they are not good at discriminating shapes that have similar gross shape but vastly different detailed shape properties as indicated in [31].

Spatial map based methods use map representation, which corresponds to the physical locations of an object, and preserve the relative positions of features in the object. They are able to capture detailed shape properties and have shown good retrieval results [31]. For example, Hebert et al. used a deformed spherical mesh, which was wrapped onto the 3D shape, and compared the shape similarity based on geometric features on the sphere [34]. The method handles complex curved surfaces and supports partial matching. Nevertheless, it uses an expensive registration step, in which data structures of all possible rotation of samples in the library are pre-generated and stored. Moreover, shape estimation error was introduced during reconstruction of original surface.

Among the spatial map based methods, spherical harmonic (SH) representation has been used in 3D shape modeling and retrieval [35][36]. Kazhdan et al. used a rotation invariant SH representation based concentric spheres model (CSM) in shape classification [7]. And Vranić proposed to use multiple radial distances instead of volumetric values to preserve more surface details [37].

Methods based on 2D visual similarity require multiple views of a 3D object [38]. Gu et al. proposed a 2D geometry image to represent a 3D mesh [39]. It cuts the 3D mesh open and maps it onto a unit square. Based on geometry images, Laga et al. proposed a shape matching method to save comparison of multiple 2D views [40]. However, similar 3D shape models are not guaranteed to have the same

cut since there are multiple choices of cutting paths. As a result their geometry images may be quite different due to different cutting, adding variance to the similarity comparison based on geometry images.

Extended Gaussian Images (EGI) uses normal vectors as geometric features to compare shape similarity [41]. However, EGI is not unique to non-convex objects, referred as an ambiguity problem, and EGI does not incorporate local spatial maps either.

We propose a new shape similarity comparison method based on spherical normal images (SNI). Normal vectors are stored in the conformal map of a 3D mesh over a unit sphere, which is one to one mapping without cutting the 3D mesh open. The overall approach follows the sequence of pose alignment, conformal mapping, feature extraction, and similarity search. We use self-organizing map to classify 3D models collected from the Internet. The proposed method applies to genus-zero objects that are sphere-like without holes or handles.

For general shape classification and matching, geometric features or processes should not be limited to specific classes of shapes. For example, as object volume applies to only closed shapes, methods involving volumes need to convert open shapes to closed shapes [42].

As for feature extraction processes, graph based methods represent geometric features using a graph, such as model graphs, reeb graphs and skeletons [43]. As efficient comparison of general 3D shapes using graph metrics is very difficult, they are not suitable in our context [31].

The rotation invariant shape descriptors based on CSM cut a 3D object along radii [7]. If internal components of the object rotate around the mass center, which results a different object, the shape descriptor will not reflect this change. In other words, the CSM shape descriptor is ambiguous to objects that differ in internal components rotation. To solve this problem, we propose a new shape descriptor based on 4D hyperspherical harmonics (HSH). It maps a 3D object directly onto a unit hy-

persphere without cut. The shape and matching processes using 4D HSH descriptor involve voxelization, conversion from Cartesian coordinates to Polar coordinates, feature extraction, classification and matching.

1.3 Contributions

In this dissertation we proposed a new generalized marching cubes method for isosurface construction.

- It allows zero values to prevail cell vertices after thresholding. Therefore the proposed method best preserves the original topology and improves representation accuracy of isosurfaces that pass cell vertices, since it does not modify sample values.
- By constructing isosurfaces with cycles in cells, it avoids enumerating a large number of cases introduced by zero cell vertices.
- And the efficiency of the proposed ZMC method is comparable to that of existing MC methods in constructing isosurfaces.

We also proposed a new approach for 3D shape classification based on spherical normal images (SNI).

- The SNI incorporates local features by conformal mapping over a unit sphere and is unique to each shape without ambiguity.
- The proposed method using SNI can discriminate collected shapes very well and performs better than that using spherical curvature images or spherical geometry images.
- The SNI based method is also robust to mesh resolution and pose variance.
- And we used the SVD method to compute SH offline to shorten the response time of online retrieval.

For general shape classification and matching, we proposed a rotation invariant shape descriptor based on 4D hyperspherical harmonics (HSH).

- The 4D HSH shape descriptor maps a 3D object onto a 4D unit hypersphere without cut along radii, thus avoid the ambiguity introduced by components with internal rotation.

- At the same vector length, the proposed 4D HSH descriptor performs better than those based on concentric spheres model (CSM) in shape classification and matching.

- We adopted support vector machine (SVM) in shape classification and integrate classification predictions into shape distance weights in similarity comparison. Experiments show the distance weights improved shape matching performance.

- We also used the SVD method to compute HSH offline to facilitate online retrieval response.

1.4 Organization of Dissertation

This dissertation is organized as follows. In Chapter 2, we briefly introduce background information of marching cubes (MC), propose a new isosurface construction method, zero-crossing marching cubes (ZMC) and solve its ambiguous cases. We also discuss non-manifold surfaces in this chapter. Then we verify ZMC cases by experiments. Synthetic data is used in a series experiments to demonstrate the correctness of ZMC method. Chapter 3 presents an application of ZMC method on measured data, 3D image segmentation results. And we also compare its performance with existing MC methods.

In Chapter 4 we discuss shape classification methods. The background of pose alignment and spherical conformal mapping of a 3D meshes are briefly described in Chapter 4. Then we propose a new feature, spherical normal image (SNI), for

shape classification. Spherical harmonic representation (SH) of SNI and self-organizing map (SOM) is used in the proposed approach, which are discussed in following sections of Chapter 4. We also present experimental results and analysis.

Chapter 5 discusses general shape classification and matching. We briefly review some popular shape classification and matching methods. Then we propose a new shape descriptor based on 4D hyperspherical harmonics (HSH). We use support vector machine (SVM) as the classifier and present experimental results and analysis on classification and matching.

Chapter 6 concludes the proposed methods for surface construction, shape classification and matching. We also discuss directions of future work related to this research.

CHAPTER 2

SURFACE CONSTRUCTION

2.1 Introduction

Surface construction is a crucial step to analyze volumetric data. Even 3D models represented by voxels in volume graphics needs surface construction to be appreciated by human eyes.

The object of surface construction is to generate a mesh representing an iso-surface. A mesh M is a pair (K, V), where K is a simplicial complex representing the connectivity of the vertices, edges and faces, thus determining the topological type of the mesh, and $V = \{v_1, \ldots, v_m\}, v_i \in \Re^3$ is a set of vertex coordinates defining the shape of the mesh in $\Re^3$.

The input of surface construction is volumetric data, which has a sample value associated with each grid point. Eight adjacent data samples enclose a cubical region, called a *cell* or *unit cube*. Cell corners are called *cell vertices* or *grid points*. Samples at cell vertices are thresholded before surface construction. Hereafter sample value is referred as that minus a threshold. And we call a cell vertex with positive/negative/zero sample value a *positive/negative/zero* cell vertex, which lies outside/inside/on the implicit surface respectively.

In this chapter we discuss methods to construct a surface, the basis for shape analysis in the later part of this dissertation. We begin with the most popular surface construction method, Marching Cubes (MC), and elaborate our improvement on MC methods. Various ambiguous cases and non-manifold surfaces are discussed.

2.1.1 Marching Cubes

If sample values are either positive or negative, the isosurface is limited to intersect a cell in $2^8 = 256$ ways since each of the eight cell vertices can lie either inside or outside the isosurface. Under this assumption, zero sample values are either avoided by carefully selected threshold or modified into small positive or negative values.

By exploiting the symmetries in the 256 ways, Lorensen et al. summarized the cases into 15 patterns, as shown in Fig. 2.1, in the original Marching Cubes (MC) method [1]. Each case is encoded and stored in a lookup table. For a given cell, it is classified into one of these 15 patterns based on its sample values. And a piece of isosurface is generated from the lookup table. The whole isosurface is constructed piecewise after processing all the cells.

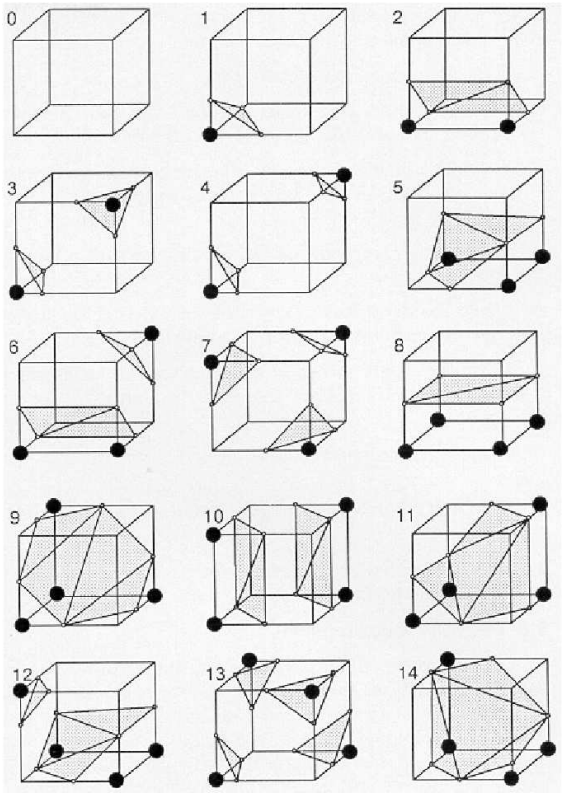

Figure 2.1: 15 cases in original marching cubes where dots represent cell vertices with different sign, figure from [1].

2.1.2 Ambiguous Cases

Nielson et. al reported that a surface hole may be generated between two adjacent cells as shown in Fig. 2.2 [9]. The hole is due to different connections of vertices on the common cell face in the two adjacent cells. The cell face with two diagonal positive vertices and two diagonal negative vertices has ambiguous connections. They proposed an asymptotic decider to solve this ambiguity.

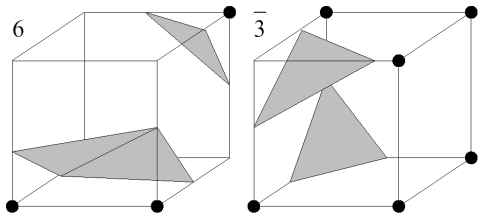

Figure 2.2: A hole between two adjacent cells. The figure is from [2].

Let ϕ_{00}, ϕ_{01}, ϕ_{10} and ϕ_{11} represent sample values at the four corners of a cell face. Value at a logical coordinate (u, v) is obtained by bilinear interpolation,

$$\begin{aligned}\phi(u,v) = \phi_{00}(1-u)(1-v) + \phi_{01}(1-u)v \\ +\phi_{10}u(1-v) + \phi_{11}uv\end{aligned} . \tag{2.1}$$

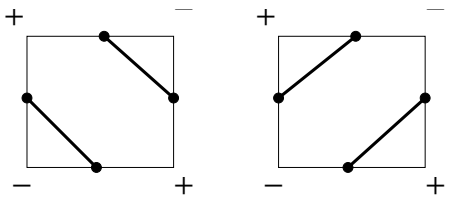

Figure 2.3: Two cases of a cell face with diagonal positive vertices and diagonal negative vertices.

From (2.1) it is easy to get that curve $\phi(u, v) = 0$ is a hyperbola on a cell face with diagonal positive vertices and diagonal negative vertices, as shown in Fig. 2.3. We then compute the interpolation value at the intersection point of the hyperbola asymptotes,

$$\phi(u_0, v_0) = \frac{\phi_{00}\phi_{01} - \phi_{10}\phi_{11}}{\phi_{00} + \phi_{01} - \phi_{10} - \phi_{11}}. \tag{2.2}$$

If $\phi(u_0, v_0) > 0$ then positive cell vertices are connected as Fig. 2.3(a); Otherwise they are separated as Fig. 2.3(b). As a result, 29 ambiguous cases are found and solved with equation (2.2) in case 3, 6, 7 12 and 13 of Fig. 2.1 [9].

Chernyaev found that, if a cell interior is estimated by trilinear interpolation, internal ambiguity, i.e. tunnel connection, may exist as shown in Fig. 2.4 [2].

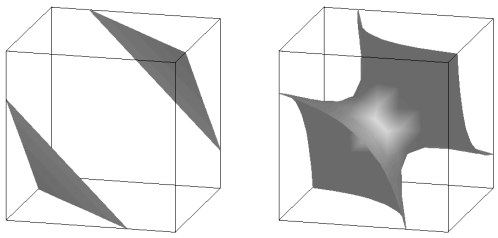

Figure 2.4: Possible tunnel connection within a cell. The figure is from [2].

A squared inequality was proposed to detect whether tunnel connection exists or not. And Chernyaev found 23 internal ambiguous cases in case 3, 4, 6, 7, 10, 12 and 13 of Fig. 2.1 [2].

2.2 Zero-Crossing Marching Cubes (ZMC)

2.2.1 Background

If sample value at a cell vertex is allowed to be zero, then each of the eight cell vertices has three instead of two possible positions relative to an isosurface, i.e. inside, outside or on the isosurface. Thus the isosurface intersects a cell in a total of $3^8 = 6561$ ways. To enumerate all these cases and reduce their symmetries manually, as what has been done in [1], are extremely tedious and error-prone to human. Without modifying sample values we are going to eliminate the original assumption of excluding zero vertices, which is used by existing MC methods. To avoid enumerating all the 6561 cases directly, we go back to check two dimensional cases instead. We name the proposed method zero-crossing MC method (ZMC).

A vertex in the mesh of an isosurface is the intersection point of the isosurface and a cell edge. The vertex position is obtained by linearly interpolating sample values of adjacent cell vertices so that the constructed isosurface is close to the desired object boundary. Vertices at two ends of a cell edge are *adjacent*. ZMC method starts from two basic assumptions as following.

Separation Assumption If two adjacent cell vertices are positive and negative respectively, an isosurface passes between them once. The two cell vertices are separated.

Connection Assumption If two adjacent cell vertices are both positive or negative, an isosurface does not pass between them. The two cell vertices are connected.

Theoretically, an isosurface can pass through two adjacent cell vertices with opposite sign in odd number of times. We introduce the above two assumptions to ensure smoothness of the isosurface. As for a zero cell vertex, the isosurface may or may not pass through it. An isolated zero cell vertex can be regarded as a degenerated isosurface. We will discuss zero cell vertices later.

For convenience of discussion, we define some terms that will be used frequently in the discussion. A *patch* is the close intersection of an isosurface and a cell, a polygon formed by connecting adjacent surface mesh vertices. A *patch edge* is the intersection of an isosurface with a cell face, whose end points are two adjacent surface mesh vertices on the cell edge. And a vertex *degree* is the number of patch edges incident on the surface vertex within one cell. Note the vertex degree here is different from typical definitions of the vertex degree, which is the total number of patch edges incident on the vertex. The vertex degree here only counts patch edges in one cell.

The definition of topology can be found in [44]. In this paper we use topology to abstract inherent connectivity of objects depicted by their boundaries or isosurfaces. Modifying zero sample values or regarding them as positive or negative ones, as shown in Fig. 1.1 and 1.2, may change this connectivity property.

2.2.2 ZMC Procedure

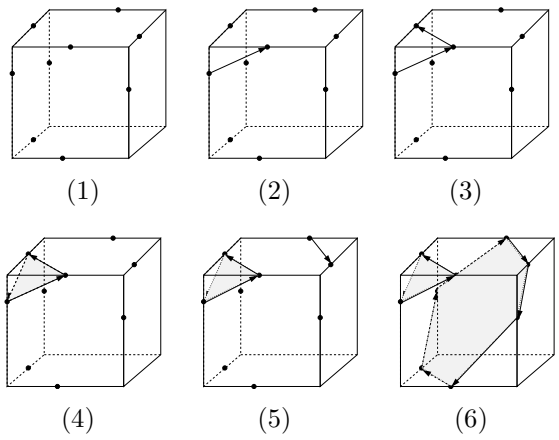

Figure 2.5: An example of one possible way to find 2 patches in a cell by exploring cycles.

As mentioned in Section 2.2.1, a cell may hold patches in 6561 different ways if taking zero cell vertices into consideration without excluding symmetric cases. Instead of enumerating all these cases, we go back to two dimensions to examine all the possible cases of how an isosurface may intersect a cell face, i.e. how a patch edge may be created. As a patch is enclosed by patch edges, the enclosure forms a graph cycle that uses each graph edge exactly once. This suggests patches in a cell can be found by exploiting cycles in the cell. The basic idea of ZMC method is following. We start from any of the surface vertices, find another coface surface vertex if possible, draw a patch edge between them, and continue with the found vertex until we return to the original vertex. After one cycle, or a patch, is completed, repeat the process until all the patch vertices in the cell have been visited. Then we find all the patches in the cell. An example of one possible way to find 2 patches is illustrated in Fig. 2.5.

However the procedure brings two questions. The first one is, how to guarantee the procedure will return to the origin vertex? In other words, how to avoid dangling edges? The second question is, how many ways there are to define patch edges on a cell face and how to make our choice? As more than two surface vertices may lie on a cell face, there are multiple ways to define the patch edges, in which the constructed patches in the cell would be completely different.

2.3 ZMC Ambiguous Cases

To answer the first question, we check the cycles that form patches in a cell. The cycles are separated without sharing common cell vertices since patches do not intersect with each other in the cell. Obviously the cycles are a simple kind of Eulerian circuits. According to the Eulerian circuit condition, a graph has Eulerian circuits if and only if it has no graph vertices of odd degree. In other words, to ensure that patches found by ZMC method are complete, the degree of surface vertex in the cell should be even. We prove later that ZMC method generates even number of

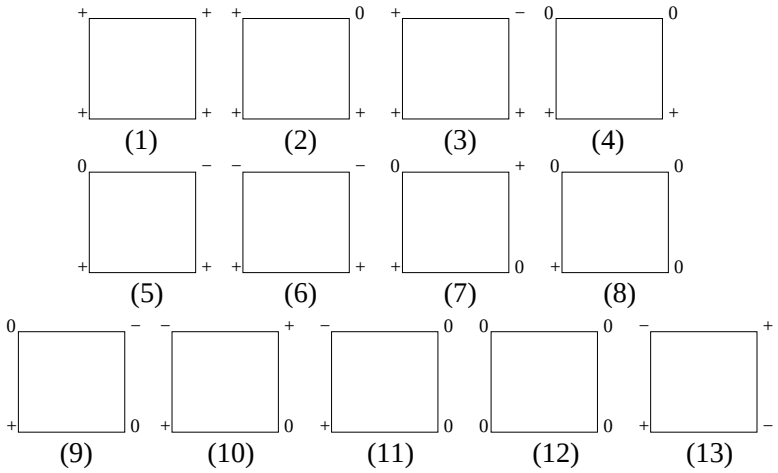

Figure 2.6: 13 cases of squares with zero cell vertices.

patch edges incident on each surface vertex in one cell. For the second question, we use the result by Banks et al. in counting cases to produce substitopes in MC methods [29]. They enumerated 13 distinct cases in two dimensions with zero cell vertices as shown in Fig 2.6, in which symmetries between positive and negative cell vertices have been eliminated. Hereafter, we refer case number to that in Fig. 2.6, unless the case number is explicitly stated otherwise. Many of these cases, however, allow ambiguous ways to connect patch edges. We will discuss these ambiguous cases in the following sections. Below is a summary of our algorithm.

1. Use bilinear interpolation on a cell face to determine patch edges for 9 of 13 cases in Fig. 2.6.

2. Define zero edge in the rest 4 cases, i.e. case 4, 8, 11 and 12 in Fig. 2.6. And solve ambiguity using two cell faces incident on the zero edge.

   (a) Enumerate all the combinations of case 4, 8 and 11 for the two cell faces, and determine patch edges based on the assumptions of separation and connection.

   (b) For case 12, use symmetry to reduce the number of configurations to 13, and solve them using previous results and the two assumptions.

3. Define zero face and determine when to insert a zero face for cases involving case 11 and 12.

2.3.1 Bilinear Cases

If the underlying functions of an isosurface are known, we can easily determine the correct topology of the isosurface and the corresponding patch edges. In case that sampled data is obtained through physical measurements, it is often impossible to know its true topology. And various methods have been proposed to solve the ambiguity of the topology.

We first adopt bilinear interpolation as in (2.1) to solve the ambiguity [9]. It satisfies the separation and connection assumptions and solves most cases in Fig. 2.6, as shown in Fig. 2.7(a). The choice between ambiguous sub-cases 13.a and 13.b can be made according to (2.2) by the asymptotic decider method proposed in [9]. Hereafter sub-case of a case is indexed by an alphabetic letter attached to the case number.

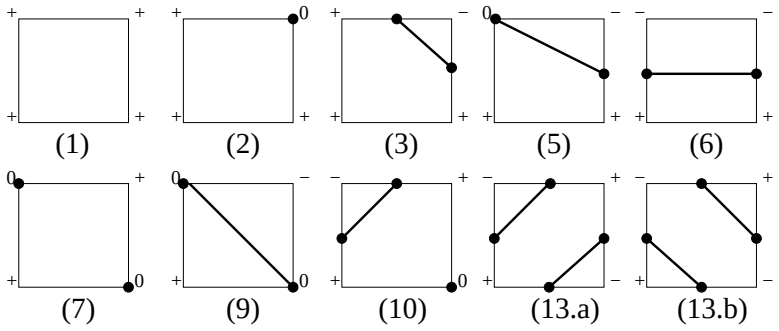

(a) 10 successful cases.

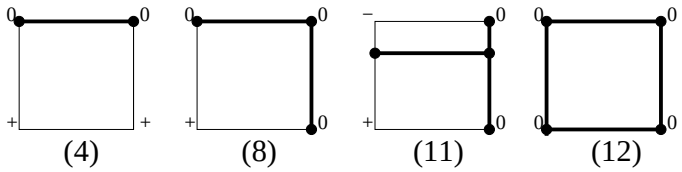

(b) 4 unsuccessful cases.

Figure 2.7: Bilinear interpolation results of 13 cases in Fig. 2.6

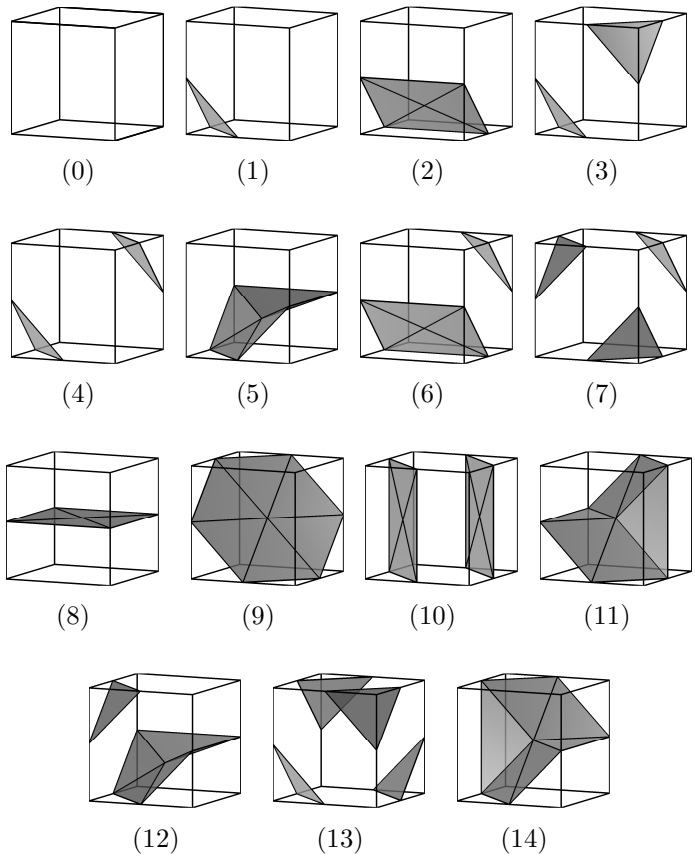

Figure 2.8: 15 cases in original MC method can be solved by ZMC correctly.

Case 1, 3, 6, 13.a and 13.b of Fig. 2.7(a) correspond to all the 15 cases in the original MC method [1]. To show that the proposed method covers all the cases of the original MC method, we use the 15 cases in the original MC method as input of ZMC method and get the same patches in Fig. 2.8 as those in Fig. 2.1 , though the triangulation is different. ZMC method also generates the same results for all the possible configurations with ambiguous faces as those in [9]. Due to page limit, we do not list the result here.

Note that the proposed method uses bilinear interpolation to determine vertices connections by patch edges on a cell face. It finds patches by cycles without specifying underline functions inside a cell and constructs isosurfaces piecewise. ZMC

method does not use trilinear interpolation, by which an internal ambiguity might exist with a tunnel connection inside a cell [2].

With the bilinear interpolation of cell faces, we have the following case rule for cases with zero cell vertices.

Case Rule of Bilinear Interpolation Using Fig. 2.7(a), we can determine the patch edges of case 1,2,3,5,6,7,9,10 and 13.

2.3.2 Zero Edge Cases

However, ambiguities in case 4, 8, 11 and 12 are not solved well by the bilinear interpolation, as shown in Fig. 2.7(b). In case 11, one patch edge intersects another between its endpoints, resulting in a discontinuous isosurface. And patch edges between two adjacent zero cell vertices, which are called *zero edges*, are not ensured to lie on the boundary of two regions with different signs.

To avoid separating two regions with the same sign, both cell faces incident on a possible zero edge should be checked. For example, to connect a zero edge α on a cell face A, as shown in Fig. 2.9, we need to check both the cell face A and B incident on α. The zero edge in case 11 is converted to either an edge β or γ to avoid self-intersection, where β or γ separates a positive or negative cell vertex from the rest of a cell face. To restate the problem, let $S_F(e)$ represents the set of face configurations, in which a cell face F contains a patch edge e. We need to solve $S_A(\alpha)$, $S_A(\beta)$ and $S_A(\gamma)$ for case 4, 8, 11 and 12.

According to the definitions of α, β, and γ, we have the following properties.

Property 1 $S_A(\alpha) = S_B(\alpha)$.

Property 2 $S_A(\alpha) \cap S_A(\beta) = \emptyset$, $S_A(\alpha) \cap S_A(\gamma) = \emptyset$, and $S_A(\beta) \cap S_A(\gamma) = \emptyset$.

Property 3 $S_A(\beta) \cap S_B(\gamma) = \emptyset$ and $S_A(\gamma) \cap S_B(\beta) = \emptyset$.

Property 1 indicates criteria to draw a zero edge α is equivalent in the adjacent cell faces A and B incident on α. According to Property 2, α, β and γ are repulsive to

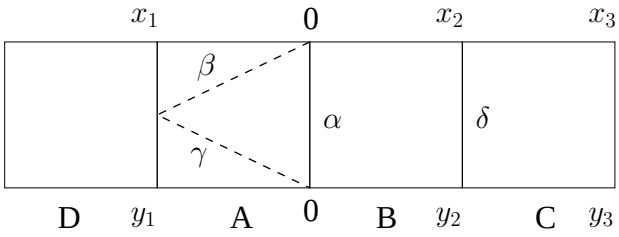

Figure 2.9: Solving zero edges. Four cell faces are unfolded with possible zero edges on a cell face A.

each other, i.e. at most one of them appears on a cell face. If A and B are of case 11, as shown in Property 3, they both separate positive cell vertices or negative cell vertices.

If we regard cell vertices at the two sides of a zero edge adjacent, we can decide patch edges based on the separation and connection assumptions in Section 2.2.1. We only need to check the combinations of adjacent cell faces of case 4, 8, 11, and 12 incident on α.

2.3.2.1 Case 4, 8 and 11

The results for the combinations of case 4, 8, and 11 are shown in Fig. 2.10, with symmetries between positive and negative vertices eliminated. Only the two cell faces incident on a zero edge among the six cell faces are used in solving zero edges. For simplicity, we unfold the two cell faces incident on the zero edge and enumerate their cases in 2D. For example, case 4 has five sub-cases from 4.a to 4.e with regard to cell faces incident on a possible zero edge. Note a case with two different ambiguous faces are indexed by two labels accordingly. For example, the second subfigure in Fig. 2.10 contains cell faces of case 4 and case 8, which is indexed by 4.b or 8.a respectively. As each of the sub-cases of case 8 has two potential zero edges, we need to check two combinations of the adjacent cell faces incident on the two potential zero edges respectively.

For ambiguous sub-cases 11.c.1, 11.c.2, 11.e.1 and 11.e.2, we want positive vertices to be connected if positive sample values take dominance. Therefore, if the absolute product of positive sample values is no less than that of negative ones, we choose 11.c.1 and 11.e.1, otherwise 11.c.2 and 11.e.2.

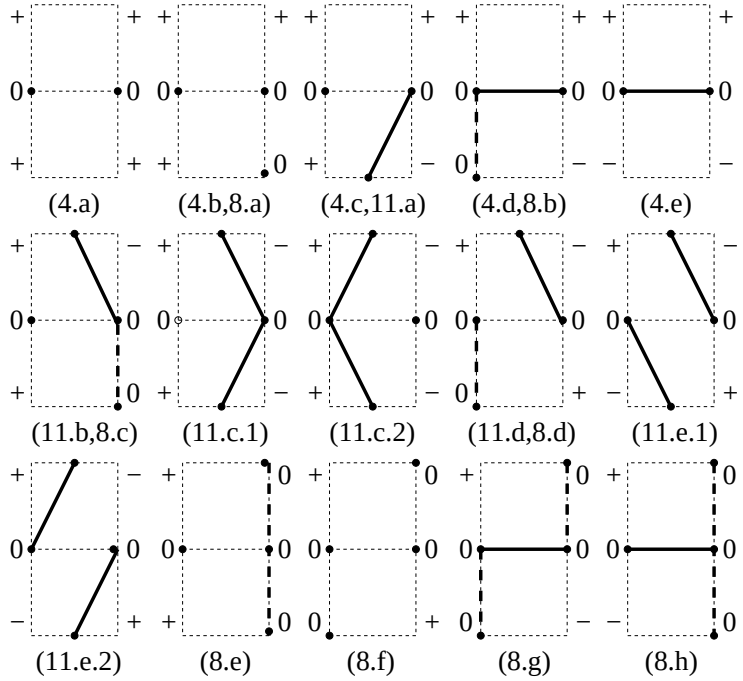

Figure 2.10: Solving ambiguities in case 4, 8 and 11 of Fig. 2.6. Two cell faces incident on the zero edge are unfolded, in which solid line stands for patch edge while dotted line for undecided patch edge.

2.3.2.2 Case 12

The results for the combinations with case 12 are shown in Fig. 2.11. Due to symmetry, the other eight cell vertices in the cell consist of 13 distinct configurations as shown in Fig. 2.6, we only need to solve these 13 configurations and illustrate them directly in 3D. Fig. 2.11 shows patch edges for the twelve sub-cases of case 12 in 3D. Note sub-case 12.a represents the configurations in which the other

eight vertices in the cell are of the case 1, 2, 4, 7, 8 or 12 in Fig. 2.6. To select between ambiguous sub-cases, we want positive vertices to be connected or take more space if positive sample values take dominance. Therefore, if the absolute product of positive sample values is no less than that of negative ones, we choose 12.d.1, 12.e.1, 12.g.1 or 12.h.1, otherwise 12.d.2, 12.e.2 or 12.g.2 or 12.h.2.

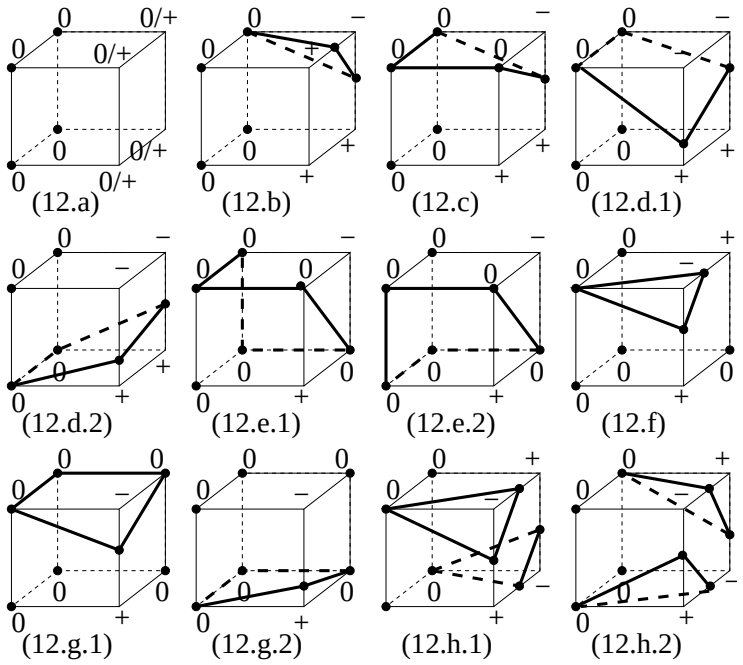

Figure 2.11: Solving ambiguities in case 12 of Fig. 2.6. Solid and dotted lines stand for patch edge.

The procedure to get the results in Fig. 2.10 and 2.11 is presented in Appendix A. We get the following case rule.

Case Rule of Zero Edge Case 4, 8, 11 and 12 with zero edges can be solved according to Fig. 2.10 and 2.11.

For previous example in section 1.2.1, Fig. 1.1(a) corresponds to case 7 in Fig. 2.7(a) and case 4.a in Fig. 2.10. Fig. 1.1(b) corresponds to case 7 in Fig. 2.7(a),

case 8.a and 8.f in Fig. 2.10. Fig. 1.1(c) corresponds to case 8.f in Fig. 2.10. Fig. 1.1(d) corresponds to 12.a in Fig. 2.11. They generate no patches within the cell.

By solving all the 13 cases of Fig. 2.6 according to the case rules of bilinear interpolation and zero edge, we can decide patch edges for all the 6561 cases in 3D. This answers the second question. To ensure that ZMC method can find all the patches by exploiting the cycles in the cell, we have the following theorem.

Theorem If patch edges are determined by the case rules of bilinear interpolation and zero edge, the degree of a surface vertex is either zero or two.

The proof is shown in Appendix B. Since a vertex degree is at most two, ZMC procedure visits a vertex at most once. In other words, midway vertices besides an origin vertex do not form any loops. So we can stop searching when all the surface vertices in a cell have been visited. The surface vertex of zero degree is regarded as isolated and simply ignored. This can answer the first question.

2.3.3 Zero Face Cases

In the case rules of bilinear interpolation and zero edge, an isosurface intersects a cell face with zero cell vertices, or zero edges. Nevertheless, the intersection may be a face, i.e. an entire patch lies on the cell face, which is called $zero\ face$. Zero faces happen on cell faces of case 12, or cell faces of case 11 with different patch edges in two adjacent cells. Similar to zero edges, to ensure a zero face is on the boundary of two regions with different signs, two adjacent cells incident on the zero face need to be checked. If we treat cell vertices in the two cells incident on a zero face adjacent, we can derive the following case rule from the separation and connection assumptions in Section 2.2.1.

Case Rule of Zero Face

1. If a zero face of case 12 separates two regions of different signs, a patch is inserted between the two adjacent cells as illustrated by Fig. 2.12(a); Otherwise, no patch is inserted.

2. If a cell face of case 11 results in a different patch edge in two adjacent cells, a patch is inserted as shown in Fig. 2.12(b).

In Fig. 2.12(a), if the right cell contains all zero vertices, the zero face is not solved in two cells. In such an extreme case with regions of zero vertices, we "shift" the left cell to right until the zero face can be solved. By inserting a zero face between two adjacent cells, we avoid the duplication from generating a zero face in each cell. And the zero face inserted between adjacent cells does not affect the theorem of vertex degree in Section 2.3.2.

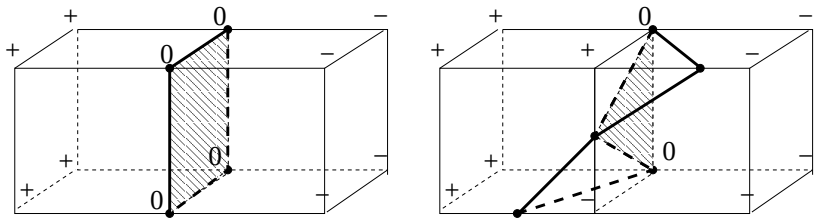

(a) Case 12 (b) Case 11

Figure 2.12: Insert a zero face between two adjacent cells represented by the shaded region.

The orientation of patch vertices is adjusted to keep the patch normal pointing outward the isosurface consistently. Once all the patches are found, we complete the whole front isosurface. As triangular meshes are extensively used in graphics applications, we triangulate patches by converting polygons to triangles. To avoid self-intersections between patches within one cell [23], we add a new vertex, the average

of patch vertices, as a common triangle vertex for a polygon with more than three edges.

Banks and Linton also counted cases with zero cell vertices in three dimensions in MC methods by numerical algorithms [29]. They found 147 cases in total with the symmetries between positive and negative vertices eliminated. However, it is unrealistic to manually verify this result by comparing the 147 found cases with the 6561 original cases. And they did not specify how to generate meshes for the 147 cases or their ambiguous cases. Hege et al. found 58 different topological cases if a cell vertex belongs to three different types that are symmetric to each other [26]. Nevertheless, zero vertex is not symmetric to positive or negative vertex. Their enumeration does not cover cases with zero vertices as Banks and Linton do. And Hege's method does not include ambiguous cases either. The advantage of ZMC method is to generate meshes by exploring cycles without enumerating all the 6561 cases. In Fig. 2.7(b), Fig. 2.10 $\sim$ Fig. 2.12, ZMC has 39 cases including ambiguous cases, much less than the 147 cases by Banks and Linton.

2.4 Non-manifold Surface

Isosurfaces constructed by existing MC methods typically separate regions with positive vertices from those with negative vertices. In other words, it is a binary space partition that generates only manifold surfaces. By modifying zero sample values into positive or negative values, existing MC methods convert a possible non-manifold surface into a manifold surface. As shown in Fig. 1.2, contacting implicit surfaces are either separated or merged if constructed by existing MC methods.

ZMC method is able to depict this type of non-manifold surfaces correctly by preserving zero cell vertices. One example of volume and surface is shown in Fig. 2.13(a). At intersection A, the space is partitioned into four parts. ZMC method depicts the intersecting sphere and square without separating or merging the two surfaces.

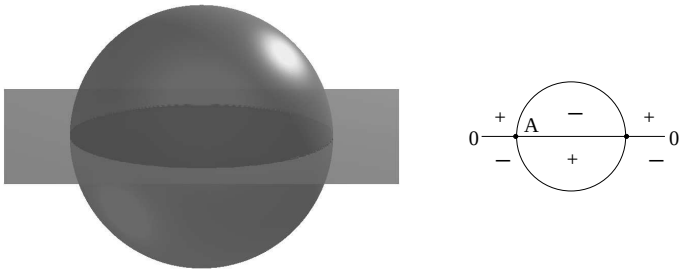

(a) A sphere and a square of four space partitions.

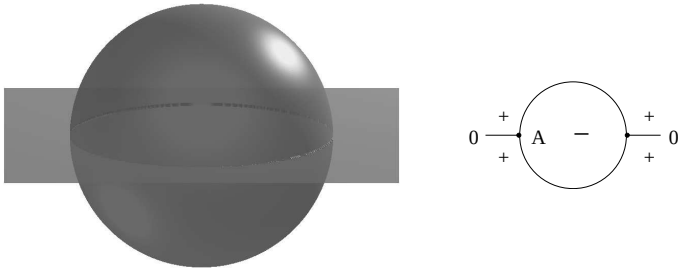

(b) A sphere and a square of three space partitions.

Figure 2.13: An example of volume and surface.

In the case rule of zero face, we insert no zero face between two adjacent cells when cell vertices at two sides of a zero face are of the same sign. Consequently two contacting surfaces with a common surface are merged into one. Nevertheless, the merging effect may be not desirable in some applications. For example, when two individual parts are assembled together, it would be better to keep their common mating face in the mesh representation. This requires partitioning a space into three regions. ZMC method can easily realize the partition by modifying the case rule of zero face a little bit. We insert a zero face between two adjacent cells incident on a zero face of case 12, regardless of the signs of cell vertices at two sides of the zero face. To illustrate, we still use the sphere and square example in Fig. 2.13(b), in which the square is viewed as a mating face of two parts. At the intersection A, the space is partitioned into three parts. And the sphere in Fig. 2.13(b) is connected instead of being separated by the square in the middle in Fig. 2.13(a).

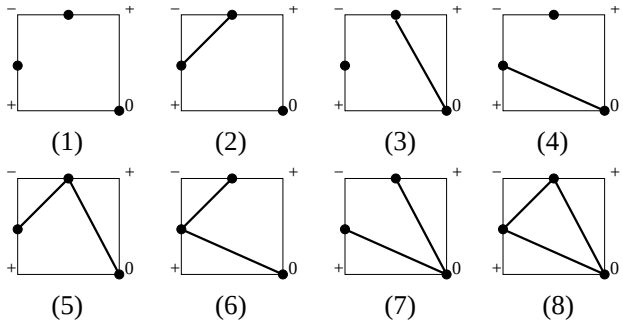

Figure 2.14: Case 10 initially has 8 possible ways to connect patch edges.

The limit of ZMC method in constructing non-manifold surfaces is inherited from the separation and connection assumptions in Section 2.2.1. For example, case 10 initially allows 8 ambiguous ways to connect patch edges as shown in Fig. 2.14. Way 1, 3 and 4 disobey the separation assumption, and way 5, 6 and 8 disobey the connection assumption. Using bilinear interpolation, ZMC method only validates way 2. Like most of existing MC methods, ZMC method prohibits edges from intersecting inside cell face and solves ambiguous cases by manifold surface patches. While existing MC methods modify zero sample values to convert non-manifold surfaces into manifold ones, ZMC depicts the original non-manifold topology correctly using zero vertices, zero edges and zero faces. Due to the connectivity of volumetric data, with zero vertices only ZMC method supports at most 2 contacting surfaces incident on a zero vertex, such as Fig. 2.17(a). With both zero vertices and zero edges, ZMC supports partitioning a space into at most 4 parts incident on a zero edge, such as Fig. 1.2. And with zero vertices, zero edges and zero faces, ZMC can partition a space into at most 8 parts with 12 zero faces incident a zero vertex, such as Fig. 2.19(d).

ZMC method supports less non-manifold surfaces than MC methods for non-manifold surfaces [24][26]. Nevertheless, ZMC method keeps zero vertices to represent an isosurface more accurately than existing MC methods when the isosurface

passes through cell vertices. And ZMC method preserves the non-manifold topology when surfaces intersect or contact at cell vertices.

2.5 Experiments and Discussions

In previous sections we presented the zero-crossing marching cubes (ZMC) method, and discussed various ambiguous cases and non-manifold surfaces. We proved in theory that ZMC method can solve all the ambiguous cases of cells with positive, negative and zero vertices. In this section, we use simulations to test all the ambiguous cases and prove the correctness of ZMC method in a series of experiments on synthetic data. We will present experiments on measured data at next chapter.

2.5.1 Case Verification

The theorem of vertex degree in Section 2.3.2 guarantees that we can find patch edges for all 6561 cases with zero vertices by exploiting cycles in one cell. In the experiments we verify the result of ZMC method on the 6561 cases. Each case is indexed by $P = \sum_{i=0}^{7} 3^i \cdot p_i$, where $p_i = 0, 1, 2$ $(i = 0, 1, ..., 7)$ corresponds to zero, positive and negative sample values respectively. The generated mesh for case P, ranging from 0 to 6560, is then rendered by Matlab and saved as pictures in JPEG files, which are available online [45]. Although generating meshes for the 6561 cases is very tedious for human, checking the pictures by hand is still doable. In each case, the generated mesh satisfies the separation and connection assumptions without dangling edges. ZMC method generates patches for the 6561 cases correctly.

To show the advantage of the proposed ZMC method, we compare it with an existing MC method implemented by Lewiner et al. [46]. Lewiner's implementation is based on Chernyaev's technique to solve the ambiguity problem on the cell face [2]. It modifies zero sample values at cell vertices to small positive values, which converts a case with zero vertices into one of the 256 original cases. The complete mapping relationship between the 256 original cases and the 6561 cases with zero vertices is presented in [45], in which the original 256 cases are indexed in the way similar to

P. Let $q_i = 0, 1$ $(i = 0, 1, ..., 7)$ corresponds to negative and positive sample values respectively. The 256 original cases are indexed by $Q = \sum_{i=0}^{7} 2^i \cdot q_i$. For example, case $Q = 227$ may be converted from 31 cases with zero cell vertices, 7 of which are shown in Fig. 2.15 along with the original case $Q = 227$. The mesh presentation of the case $Q = 227$ changes obviously after the modification on zero sample values. It illustrates representation error of existing MC methods on implicit manifold surfaces that pass cell vertices.

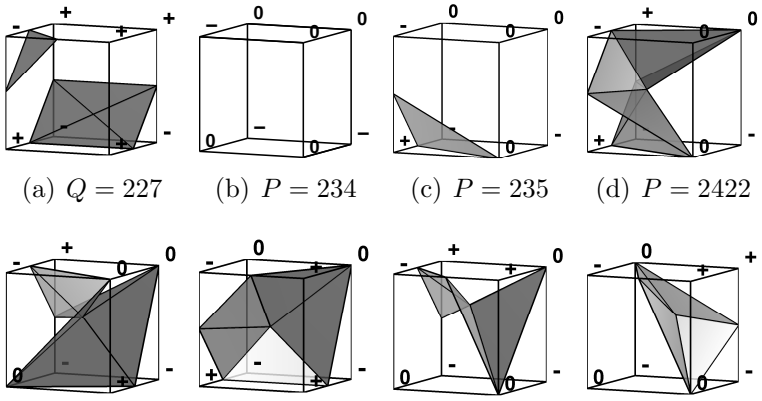

(a) $Q = 227$ (b) $P = 234$ (c) $P = 235$ (d) $P = 2422$

(e) $P = 2424$ (f) $P = 481$ (g) $P = 2664$ (h) $P = 1206$

Figure 2.15: One original case $Q = 227$ and its corresponding cases with zero vertices.

We also check ZMC method over ambiguous cases that are solved by comparing the product of positive and negative sample values in case 11, 12 or 13. Based on the comparison result, we choose from two possible results of an ambiguous face. Let $r_i = 0, 1$ $(i = 0, 1, ..., 5)$ represents the two results of an ambiguous face i. The index number $R = \sum_{i=0}^{5} 2^i \cdot r_i$ ranges from 0 to 63. For example, case $P = 2422$ in Fig. 2.15(d) has two ambiguous faces of case 11 and 13. To enumerate its ambiguous cases, let the two positive sample values be D_1, D_2 or D_3, and the three negative sample values be $-D_1$, $-D_2$ or $-D_3$, where $D_3 > D_2 > D_1 > 0$. With $3^{2+3} = 243$

enumerations, we find 2 ambiguous cases for case $P = 2422$. For the 6561 cases with zero vertices, we find total 8447 ambiguous cases, which are indexed by P and R [45].

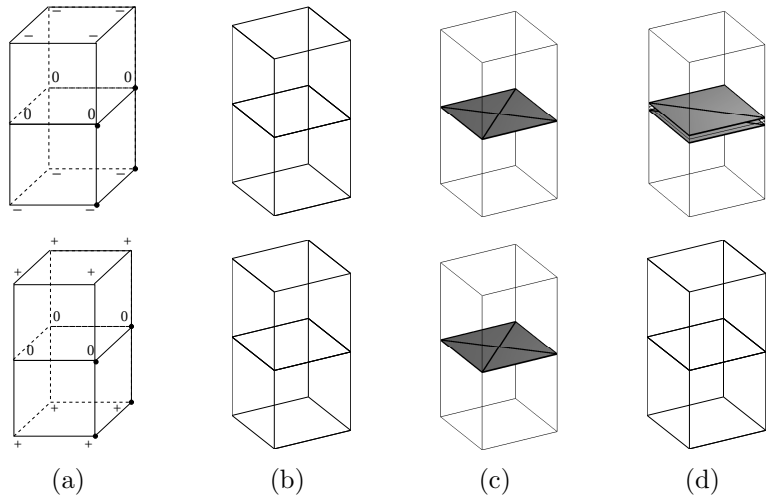

Figure 2.16: Topologies comparison on case 12 in Fig. 2.6: (a) Original topology (b) ZMC (c) Modified ZMC (d) Lewiner's implementation.

For the case rule of zero face, we test ZMC method by enumerating all the different combinations of two adjacent cells incident on the cell face of case 11 or case 12 in Fig. 2.6. ZMC method works correctly on all these enumerations with results in [45]. On example of two cells incident on a cell face of case 12, is shown in Fig. 2.16. ZMC method gives no zero face since the zero face are not on the boundary of two regions with different signs. For the modified case rule of zero face in Section 2.4, ZMC generates one zero face. ZMC method gives consistent results when the cell vertices besides the zero face in the two adjacent cells are positive or negative. In comparison, Lewiner's MC implementation outputs two planes for the top case of Fig. 2.16. But it generates no plane when the sample values are multiplied by -1 in the bottom case of Fig. 2.16. It shows preference to positive values since it changes zero sample values to positive ones.

2.5.2 Non-manifold Surface

We compare Lewiner's implementation and ZMC method over the cases in Fig. 2.17. For the case shown in top row of Fig. 2.17, Lewiner's method reports eight times of case 2 of Fig. 2.8 and generates 16 triangles. When the sample values are multiplied by -1 as shown in the bottom case of Fig. 2.17, Lewiner's method reports eight times of case 1 of Fig. 2.8 and generates 8 triangles. To illustrate, we enlarge its small positive value to 0.05 and get the result in Fig. 2.17(c). Note this enlargement does not change the topologies of constructed meshes or the number of generated triangles. The proposed ZMC method consistently preserves the original topology as shown in Fig. 2.17(b).

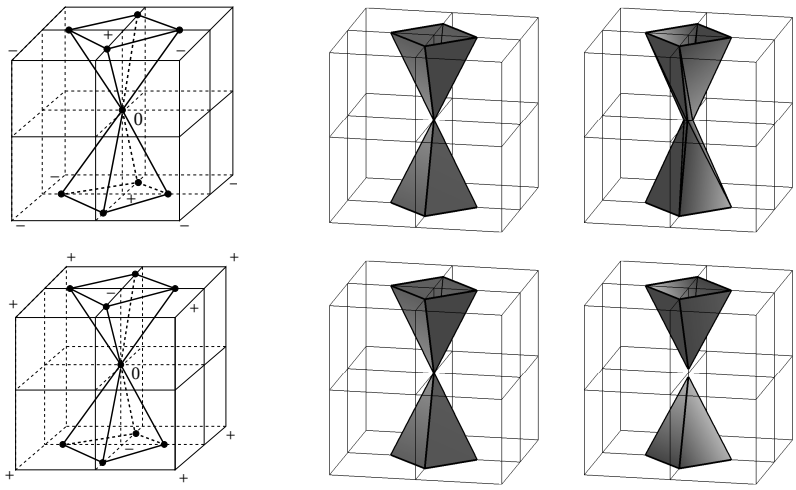

(a) Original Topology (b) ZMC (c) Existing MC

Figure 2.17: Topologies comparison between ZMC and the Lewiner's MC implementation on cases 2 in Fig. 2.7(a).

The example of non-manifold surfaces in Fig. 2.13, volume and square, are constructed by Lewiner's implementation in Fig. 2.18. Comparing with Fig. 2.13(a), the sphere is converted into a bowl and a half sphere in Fig. 2.13(a). And the square in Fig. 2.13(b) is removed in Fig. 2.18(b). Note the enlargement causes coarse sphere

surfaces but does not change the topologies of the surfaces constructed by Lewiner's implementation. In contrast, ZMC method preserves the sphere with two contacting half spheres In Fig. 2.13(a). And it correctly depicts a whole sphere and square in Fig. 2.13(b).

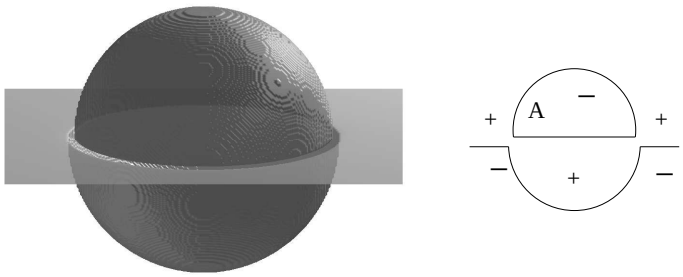

(a) A sphere is converted into a bowl and a half sphere.

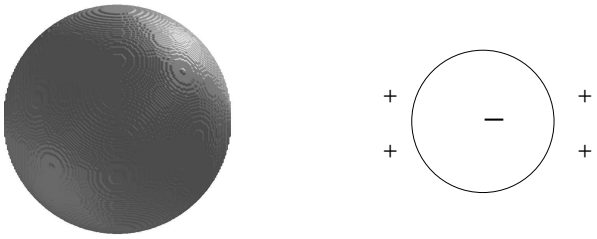

(b) The square is removed.

Figure 2.18: Depicting non-manifold surfaces by existing MC methods.

2.5.3 Synthetic Data

To illustrate that ZMC can construct isosurfaces correctly, we synthesize volume data with known underlying functions and use them as input. The results are accordant with the underlying functions as shown in Fig. 2.19.

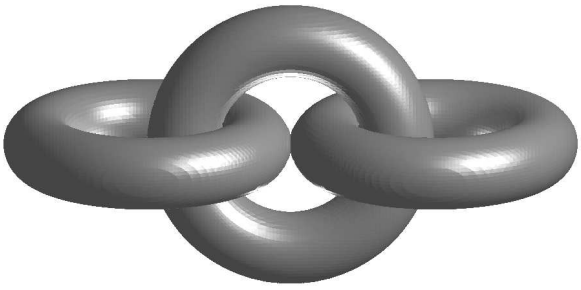

(a) Three torus

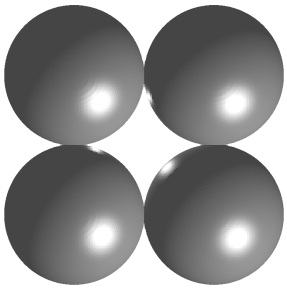

(b) Four spheres

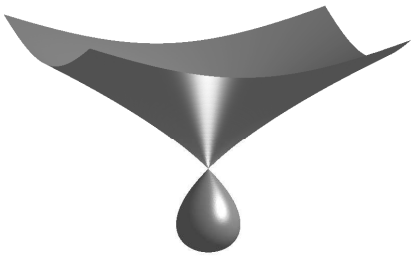

(c) Drip

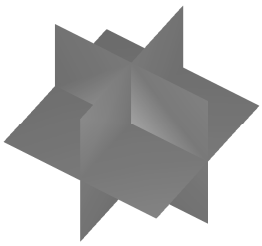

(d) Case

Figure 2.19: Examples constructed by ZMC.

CHAPTER 3

VISUALIZING IMAGE SEGMENTATION

In Chapter 2, we presented the ZMC method and verify it on simulated cases and synthetic data. In this chapter we apply ZMC method on measured data, 3D image segmentation results. ZMC method was motivated by the need to visualize 3D image segment results from our new level set method. As level sets may pass through grids, or cell vertices, existing methods modify zero-valued data [28], which introduces topological changes as discussed in Section 1.2.1. Without changing data values, ZMC method preserves original topology better and exhibits comparable performance with existing MC methods on large volumetric data set.

In this chapter, we briefly introduce the background of an extensively used image segmentation method, level set, and our improved 3D level set method. To visualize 3D segmentation results, we apply ZMC method and conduct a series of experiments to compare its performance with existing MC methods.

3.1 Level Set Method

Propelled by growing computing power, 3D image processing techniques find increasing applications in medical domain, such as computer aided diagnose (CAD) and computer aided surgery. As a key technology, 3D image segmentation became a popular topic of medical image processing. Accurate 3D geometric information of organic structures is crucial for early disease diagnose and treatment. However, segmentation of some organic structures, such as lung bronchia and nodules, is a challenging task due to their complex topologies. We proposes a new automatic 3D image segmentation method for these structures based on level set method.

Level set method, proposed by Osher and Sethian, has been extensively studied and widely used in image segmentation [47]. Many variations have been proposed to improve the level set method. One branch of level set methods, fused the various regional statistics like intensity distribution, can enhance segmentation capabilities. For example, Baillard et al. incorporated pixel-classification based on intensity distribution into the level set speed function [48]. Their automatic method gave impressive segmentation results on brain images. To estimate distribution of incomplete data, Dempster et al. proposed an expectation-maximization (EM) framework [49], which has been adopted in many later approaches such as [50]. And a stochastic EM (SEM) algorithm, was proposed by Masson and Pieczynski to reduce the dependence on initialization of the EM method [51]. However, both the EM and SEM method do not guarantee the global optimal estimation and or eliminate the dependency of estimation results on initialization. The estimation error in intensity distribution can make segmentation results instable as shown in the later sections of this chapter. We investigate the effects of the estimation error and propose a new calibrating mechanism to combine gradient information and intensity distribution into segmentation process. By searching the maximal overlap of image gradient with the boundaries determined by intensity distribution, the proposed method can locate the boundaries of interested objects more stably.

The central idea of level set is to represent boundaries of different regions by a moving front $\gamma(t)$, which converges to the desired boundaries from its initial position. The moving front $\gamma(t)$ is a zero level set of a higher dimensional function $\psi(x,t), x \in \Re^N$, and represents a closed hyper-surface. It is propagated along its normal direction by updating $\psi(x,t)$ according to some criteria. The $\Re^N$space is then divided by the moving front, into the region Ω enclosed by $\gamma(t)$ and the outside region $\overline{\Omega}$, which satisfy: $\psi(x,t) < 0, x \in \Omega; \psi(x,t) = 0, x \in \gamma(t); \psi(x,t) > 0, x \in \overline{\Omega}$. The evolution equation for $\psi(x,t)$ is given as

$$\psi_t + F|\nabla\psi| = 0, \tag{3.1}$$

where F is the speed function of the moving front. A typical speed function is in the form of:

$$F = \hat{k}_I(F_A + F_G), \tag{3.2}$$

where $\hat{k}_I = 1/(1 + |\nabla G_\sigma * I(x)|^m)$ reflects the stopping criteria by image gradient, F_A is an advection term independent of the moving front's geometry, and F_G is a speed term dependent on the geometry such as local curvature.

The speed function should decrease to zero quickly when the front meets object boundaries. It suggests a large m in $\hat{k}_I$ if using image gradient as the only stopping criteria. Nevertheless, with a large m the front is likely to stop at regions with middle gradient, which may be noise or textures, instead of object boundaries in an image. On the other side, with a small m level set may leak into object boundaries whose gradient is low.

3.2 Intensity and Gradient Combined Level Set

Using intensity distribution into the level set speed function, instead of image gradient, eliminates the need to adjust m, thus makes segmentation automatic. It can detect object boundaries with low gradient or reduce noise effect in gradient. However, an accurate and stable estimation of intensity distribution is difficult to get from a finite set of 3D image data. The EM or SEM method does not guarantee convergence, or find the global optimum, whose results depend on the initialization. Consequently, the segmentation result based on intensity distribution may be instable. For example, by running the SEM algorithm twice on a 3D lung image of size $80 \times 80 \times 28$, we get two estimation results of its intensity distribution, as shown in Fig. 3.1(a) and 3.1(c). Note the estimation results around the left peak are differ-

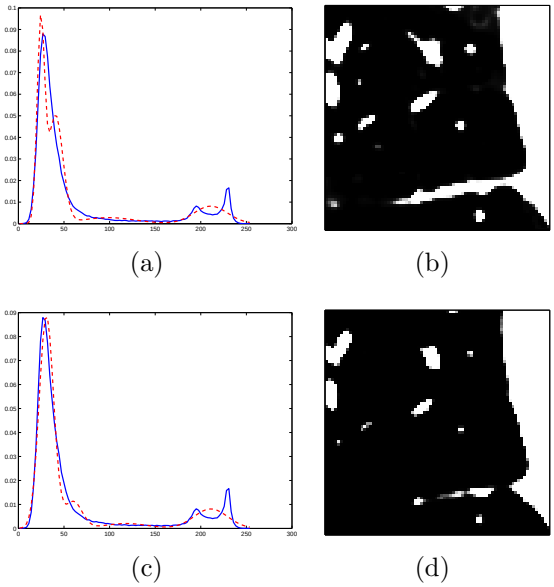

(a) (b)

(c) (d)

Figure 3.1: Instable segmentation results in (b) and (d), resulted from Two estimation of intensity distribution of a 3D image in (a) and (c) respectively. The blue line is the intensity histogram while red line the estimation result.

ent in the two figures. Fig. 3.1(b) and 3.1(d) show the corresponding results of the level set segmentation on a slice at $z = 10$. The inside region in Fig. 3.1(d) "shrinks" compared with that in Fig. 3.1(b), resulting some structures to break or disappear. The original image of the slice and its gradient are shown in Fig. 3.2(a) and Fig. 3.2(b) for reference. Checking intensity values of different parts in Fig. 3.1, we find the left peak corresponds largely to the background, the right two peaks corresponding to lung walls, and the middle flat part corresponding to the organic structures we are interested on, such as bronchia, vessels and the boundaries of lung walls. As their intensity values are not distinctive from those of the background, a small disturbance on the estimation result of intensity distribution, will change the segmentation result of the low intensity structures obviously.

To reduce the "shrink" or "expand" effect on segmentation results, we propose to use gradient information to calibrate the estimation of intensity distribution in the following. We compute the overlap of image gradient with the boundaries determined by intensity distribution through introducing a probability offset to in-

tensity distribution. The maximum overlap indicates the optimal boundaries of the interested objects.

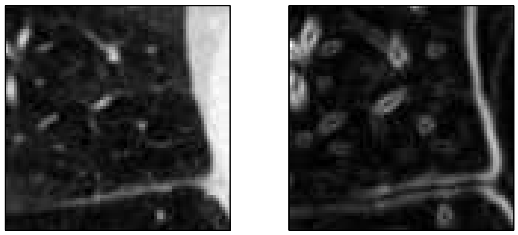

(a) Original Image (b) Gradient

Figure 3.2: One slice at $z = 10$ in the 3D image in Fig. 3.1.

To restate the problem without losing generality, here we use a mixed Gaussian distribution model,

$$P(u) = \sum_{k=1}^{n} \pi_k P(u \left| \lambda_k; \mu_k, \sigma_k \right.), \tag{3.3}$$

where π_k is the prior probability of class λ_k with $\sum_{k=1}^{n} \pi_k = 1$, and μ_k, σ_k are the mean and variance of the Gaussian distribution of the intensity. We then get the intensity distribution inside the region Ω,

$$P_{in}(u) = \sum_{k|\lambda_k \in \Omega} \pi_k P(u \left| \lambda_k; \mu_k, \sigma_k \right.). \tag{3.4}$$

And the intensity distribution of the outside region $\overline{\Omega}$, $P_{out}(u)$, can be obtained in a similar way. Normally for pixel x on region boundaries with $u = I(x)$, we have

$$P_{out}(I(x)) - P_{in}(I(x)) = 0. \tag{3.5}$$

The final boundaries, where level set front actually stops, coincident largely with those predicted by (3.5) in practice. As previously discussed, segmentation result by

level set methods based on intensity distribution requires an accurate estimation of intensity distribution, while the global optimum of the estimation is not guaranteed by existing EM methods.

To evaluate the estimation result of intensity distribution, we introduce a probability offset w into equation (3.5) and define,

$$\phi(x, w) = P_{out}(I(x)) - P_{in}(I(x)) - w, \tag{3.6}$$

where the boundaries satisfy $E(x, w) = \{x|\phi(x, w) = 0\}$. The value of w indicates the reliability of segmentation results by intensity distribution. For example, a negative w causes the segmentation result of inside region Ω to shrink, indicating the probability of the inside region Ω has been overestimated. Actually, $\phi(x, w)$ is a hyper-surface similar to the definition of $\psi(x, t)$ in level sets, in which $\phi(x, w) = 0$ represents object boundaries like level sets $\psi(x, t) = 0$ do. Define $d(x, w)$ as the minimum distance from x to object boundaries and the according boundary detector is,

$$Y_e(x, w) = e^{-d^2(x,w)}, \tag{3.7}$$

where $Y_e(x, w) = 1$ for x on the boundaries and decreases exponentially with distance $d(x, w)$. Different from the intensity-based boundary detector in [48], $Y_e(x, w)$ takes the position x into consideration, indicating voxels in the center of an object are less likely to be boundaries. As we expect the boundaries defined by intensity distribution to overlap with image gradient as much as possible, define an objective function as,

$$S(w) = \int_x (\nabla G_\sigma * I(x)) Y_e(x, w) dx. \tag{3.8}$$

The global overlap between the boundaries defined by the intensity distribution and gradient is maximized, when

$$\hat{w} = \arg\max_{w} S(w)\,. \tag{3.9}$$

Note that existing intensity distribution models assume $\hat{w} = 0$. Furthermore, to adjust boundaries locally, we define a factor $\hat{k}_P = 1 - Y_e(x, \hat{w})$ in the level set speed function representing the boundaries defined by intensity distribution. The final speed factor $\hat{k}$ combining both $\hat{k}_I$ and $\hat{k}_P$ can be designed in many ways. Generally, $\hat{k}$ is assigned a low value when both $\hat{k}_I$ and $\hat{k}_P$ are of low values, and a high value when both $\hat{k}_I$ and $\hat{k}_P$ are of high values. Otherwise, $\hat{k}$ is a balanced value between $\hat{k}_I$ and $\hat{k}_P$. To weight $\hat{k}_I$ and $\hat{k}_P$ automatically, we adopt a fuzzy logic table similar to that in [52].

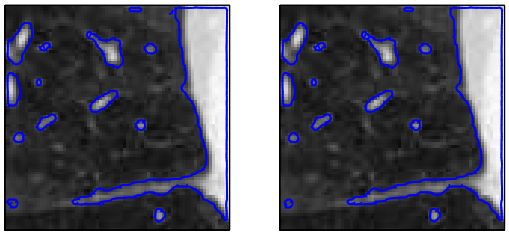

(a) The result of Fig. 3.1(a)

(b) The result of Fig. 3.1(c)

Figure 3.3: Final 3D segmentation results by combining gradient information and intensity distribution on the slice at $z = 10$.

To find $\hat{w}$ for equation (3.9), we search scope $[-w_{SC}, w_{SC}]$ in multiple resolutions, and the scope w_{SC} is computed by,

$$w_{SC} = C \cdot \int_u |\frac{P(u) - H(u)}{H(u)}|^2 du \tag{3.10}$$

where C is an empirical constant and $H(u)$ the normalized histogram at intensity u. Actually, w_{SC} prevents $\hat{w}$ converging to the boundaries of neighboring objects inside or outside the current object.

The final segmentation results by the proposed method based on the two estimation of intensity distribution in Fig. 3.1(a) and 3.1(c) are shown in Fig. 3.3(a) and 3.3(b) respectively. The difference between the two results is almost indiscernible. Compared with Fig. 3.1(b) and Fig. 3.1(d), some noise in the gradient is filtered out and the right side of the lung wall is preserved well where its gradient is low.

Lin et al. proposed to combine the distribution of both image gradient and intensity [53]. But they did not consider estimation error in intensity and gradient distributions.

The advantage of our method comes from using gradient information to calibrate the instable segmentation results, found by level set methods based on instable estimation of intensity distribution. It is helpful especially when the intensity distribution is non-Gaussian, such as Rayleigh or Poisson distribution, where using Gaussian model to estimate the intensity distribution may introduce large estimation error.

3.3 Experimental Results and Analysis

3.3.1 Visualize Segmentation Results

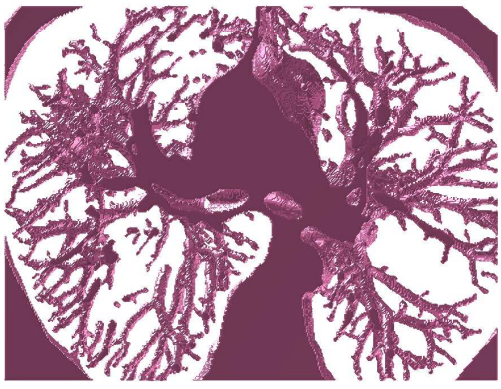

Figure 3.4: Segmentation results of a 3D lung image data. 3D boundary surface reconstructed.

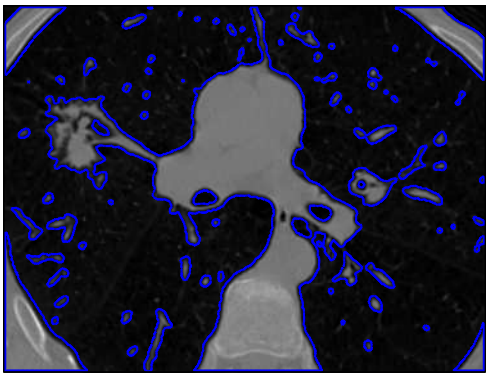

Figure 3.5: Segmentation results: 2D contour on one slice at $z = 26$ in blue lines.

We test the proposed method on a series of CT lung scans downloaded from the National Cancer Institute [54]. A narrow band level set method is implemented to improve speed [47]. Time step is chosen adaptively to satisfy the Courant-Friedrichs-Levy restriction to make segmentation stable. A user only needs to specify a box containing the interested organic structures, or the region of interest (ROI). Using a ROI with $290 \times 380 \times 62$ voxels as the initial front surface, we get the segmentation result with spacing 0.68, 0.68, and 0.63 mm along X, Y, Z axes.

To visualize the segmentation result, we construct a 3D boundary surface in Fig. 3.3.1 using ZMC method. The thin structures like bronchia and fine surface details are well captured. Note that some bronchia are not connected to the major bronchial tree in this part of lungs. This is not resulted from the segmentation or reconstruction error.

Another advantage of ZMC method is that 2D contours have already been generated by patch edges within each patch. By collecting patch edges on every plane, we can get the 2D contour at specified position, as shown for one slice at $z = 26$ in Fig. 3.3.1. Ho et al. also constructed surfaces by finding 2D segments in their CMS method [55]. But the CMS method does not consider zero cell vertices, hence it inherits the topological artifacts of existing MC algorithms.

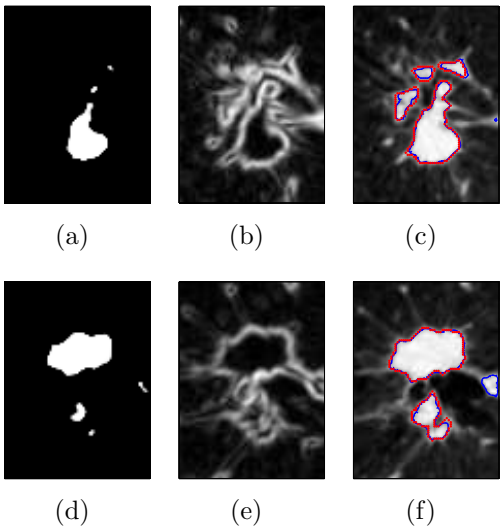

Figure 3.6: Segmentation results on nodule slices at $z = 24$ and 33. (a) and (d) are the segmentation results by intensity distribution; (b) and (e) are the gradient; And (c) and (f) are the final result by the proposed method in **blue** lines. The **red** lines are the nodule cores manually marked by physicians.

From Fig. 3.3.1 and Fig. 3.3.1, it is easy to detect a nodule with many connections in the left lung. We can re-assign the ROI to segment the nodule core. Fig. 3.6(a) and 3.6(d) show the segmentation results by the intensity distribution on slices at $z = 24$ and 33 respectively. The gradient is shown in Fig. 3.6(b) and 3.6(e). Fig. 3.6(c) and Fig. 3.6(f) show the segmentation results by the proposed method for comparison. The inside regions of the nodule core were initially underestimated by the intensity distribution, but calibrated by the gradient in the final results as shown by the blue line. To compare with ground truth, we overlap the segmentation results with the manual results by physicians in red contour [54]. From Fig. 3.6(c) and 3.6(f), the two contours coincide very well. Note that it is difficult to segment the nodule core by gradient information alone since the gradient around the nodule core is not distinctive from that around the outline of the nodule.

In the experiments, we find that final segmentation results are decided largely after the global calibration by $\hat{w}$, indicating the role of local adjustment by the fuzzy logic table is limited. In other words, $\hat{w}$ causes the boundary defined by intensity

distribution to shrink or expand globally to overlap with image gradient as much as possible, which is essential to make final segmentation results stable. Nevertheless, the proposed method can not "correct" segmentation results when the SEM method gives an estimation of intensity distribution that largely deviates from the true distribution. In practice, we run SEM method several times to select the best estimation with the minimal w_{SC} value.

The estimation of intensity distribution of the ROI with $290 \times 380 \times 62$ voxels takes about 29 seconds while the level set segmentation takes 15 minutes. The algorithm has been run automatically over a total of 23 data sets and the results have been validated by experienced physicians. Quantitative evaluation will be conducted in the near future for the purpose of nodule classification.

3.3.2 Performance Comparison

As ZMC method processes more cases than existing MC methods, it is slower than Lewiner's implementation, which constructs isosurfaces by a pre-computed lookup table. To speed up the construction process, we store the ZMC results of all the 8447 ambiguous cases in Section 2.5.1 in a lookup table indexed by P and R. For a specific case, instead of searching cycles, we compute its index number P and R and retrieve the patches from the table. The running time depends on the size of volumetric data, i.e. the number of voxels, and the specific isosurface. We use a series of volumetric data of different sizes from [54] and compare the running time of ZMC method with Lewiner's MC implementation, as shown in Table 3.1. From the table, ZMC is a fast algorithm, which can generate about one million triangles per second in the experiments. Its efficiency is comparable to that of Lewiner's implementation. Note ZMC method produces around 70% more triangles than Lewiner's implementation do. The difference is due to a new common vertex added each patch with four edges or more during triangulation. An alternative method to reduce the number of triangles is to use an existing patch vertex as the common triangle vertex.

For example, the alternative method gives two triangles for a quadrangle instead of four. Nevertheless, triangles generated by the alternative method depend on which common vertex to use. And the alternative method may give a triangle on a cell face, i.e. zero face in one cell, when three of the patch vertices are zero cell vertices. It causes duplication or discrepancy among adjacent cells incident on the zero face triangle. Further processing on this case and an adaptive approach in the future can reduce the number of triangles.

	Dimension	**Voxel Number** (10^6)	**Triangle Number** (10^6)	**Time (s)**
MC	210×320×36	2.33	0.31	0.45
ZMC			0.50	0.59
MC	512×512×28	7.05	1.12	1.42
ZMC			1.86	1.73
MC	512×512×62	15.93	1.58	2.78
ZMC			2.62	3.34
MC	512×512×103	26.63	4.36	5.5
ZMC			7.67	7.34
MC	512×512×150	38.91	5.88	7.56
ZMC			10.42	9.88

Table 3.1: Running time of ZMC and Lewiner's Implementation. Time are in seconds.

To get statistics of the 13 cases, we count their occurrence among the cells that contain patches. Fig. 3.7 show the percentage of the occurrence of the 13 cases in the third experiment with integer-valued samples of table 3.1. It indicates the cases with zero vertices, case 2 and case 5, take 2% and 4%. Actually, the percentage of the 13 cases varies dramatically with volumetric data and experimental conditions. All the experiments are carried out on an AMD Anthlon 64bit 3700+ processor with 2G RAM.

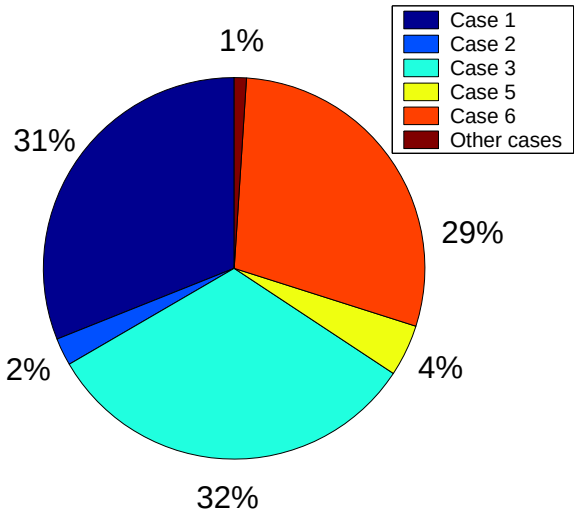

Figure 3.7: Percentage of the 13 cases in one experiment. The other cases include case 4 0.18%, case 7 0.02%, case 8 0.01%, case 9 0.08%, case 10 0.28%, case 11 0.06%, case 12 0.0004% and case 13 0.39%.

CHAPTER 4

SPHERICAL NORMAL IMAGE

In Chapter 2 and 3 we discussed methods to construct surface of a 3D model from volumetric data. As more and more 3D models are available, it is desired to retrieve 3D models with specific shapes efficiently. In a library, books are indexed into various classes so that people can access a specific book quickly. Similarly, a way to index 3D models is the key for shape classification and matching. Unfortunately, 3D models do not carry keywords with themselves, like titles, authors or subjects of books. Geometric features of 3D models are used instead for representation and classification purpose.

In this chapter, we discuss the shape classification process using a new feature, spherical normal image (SNI). It applies for sphere-like 3D models without holes or handles, which are genus-zero objects. The process involves pose alignment, conformal mapping, feature extraction using surface normals, and classification using self-organizing map (SOM). The overall approach is shown in Fig. 4.1.

In the feature extraction step, SNIs are generated and used to index 3D models. We use a spherical harmonic (SH) representation of SNI to facilitate classification process. We conduct experiments to test the effectiveness of SNI as a shape descriptor and compare it with other geometric features like curvature and geometry images. Multi-resolution support and the choice of classifiers are also discussed.

4.1 Pose Alignment

Traditional shape recognition methods that are based on geometric features follow the strategy of registration and recognition. The registration eliminates the

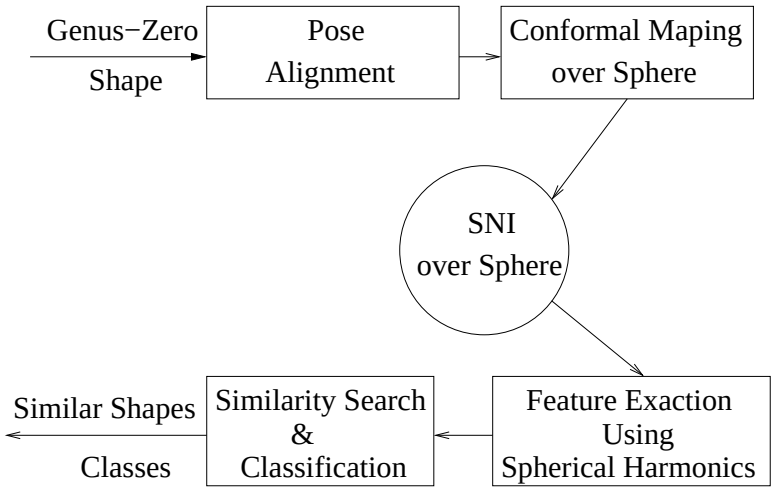

Figure 4.1: The procedure of genus-zero shape classification.

variance of feature vectors caused by different poses. Factors to be considered usually include scaling, translation, and rotation. Translation is usually removed by shifting the center of a mesh to the origin, and scaling is removed through normalization. As for rotation, different methods have been proposed.

Hebert et al. proposed a pre-processing stage in which data structures of all possible rotations of samples in a library are generated and stored [34]. This method saves the time of pose alignment during online retrieval and enables partial comparison of similar surfaces. Nevertheless, it requires an extra large storage of samples at each possible rotation up to the resolution of a mesh. Kazhdan et al. used a rotation invariant feature to avoid the rotation process [7]. Vranić compared the shape comparison methods using principle component analysis (PCA) in pose alignment and the methods without rotation processing, and concluded that the PCA based methods have better performance [37].

The PCA method finds a set of orthogonal principle axes, on which projects of original variables have the maximum variance. Principle axes are eigenvectors of a covariance matrix of variables:

$$Cov = \frac{1}{N}\sum_{k=1}^{N}(\vec{V}_k - E(\vec{V}_k)) \times (\vec{V}_k - E(\vec{V}_k))^T, \tag{4.1}$$

where $(\vec{V}_1, \vec{V}_2, \cdots, \vec{V}_k, \cdots, \vec{V}_N)$ are the original variables and $E(\vec{V}_k)$ is the average. Projects of the variable, or new variables, are generated by rotating the variable around the average to the principle axes.

PCA method is efficient since it only involves eigenvector operations on the matrix. However, two problems must be dealt with to apply PCA method in pose alignment. First, if mesh vertices are used directly to calculate principle axes, the result is sensitive to tessellation and resolution of the mesh. Second, PCA method does not distinguish directions of principle axes.

For the first problem, Novotni et al. used mass distribution of the object, a volumetric property, in the pose alignment [56]. Saupe and Vranić replaced the average with the gravity center $\vec{C}$ in their continuous PCA method (CPCA) [57]. Original point set I is then translated to get a new point set,

$$I_1 = I - \overrightarrow{C} = \{\overrightarrow{U} \,|\, \overrightarrow{U} = \overrightarrow{V} - \overrightarrow{C}, \overrightarrow{V} \in I\}. \tag{4.2}$$

And the covariance matrix is modified to be,

$$C = \frac{1}{S}\int_{I_1} \vec{U} \times \vec{U}^T du, \tag{4.3}$$

where S is the surface area. As for the second problem, the directions of principle axes are specified by multiplying the rotated result with a diagonal matrix,

$$F = diag(sign(f_x), sign(f_y), sign(f_z)), \tag{4.4}$$

where

$$f_x = \frac{1}{S}\int_{I_2} sign(V_x) V_x^2 dv, \tag{4.5}$$

and f_y, f_z are obtained in a similar way.

We adopt the CPCA method in our pose alignment process, which works well with most of the shapes collected from the Internet.

4.2 Conformal Mapping

To analyze geometric features of a 3D object, it is convenient to map the object surface onto a region of a plane or sphere first. Surface analysis is then carried over the plane or sphere domain. For a closed surface, mapping it onto a sphere, if possible, yields less distortion than onto a plane.

Hebert et al. used a self-defined mapping in which a regular mesh initially on a sphere is deformed to wrap a 3D object [34] . It captures the outline of the 3D object and supports non-zero genus object with holes or handles. However, it introduces shape estimation error during surface reconstruction as original mesh is deserted. Moreover, a regular mesh on sphere does not contain any geometric information itself. Only nodes associated with its vertices contain geometric features of the reconstructed mesh.

In contrast, conformal mapping is one-to-one and angle preserving. A mapped mesh and the original mesh differ only in scaling factor in terms of the first fundamental form. In other words, shape is preserved locally in the sense that distances and areas are only changed by a scaling factor [58]. Conformal mapping is used in many applications such as texture mapping, remeshing and visualization. Many algorithms have been proposed to calculate conformal mapping [59] [58]. Eck et al. computed the conformal map of a 3D mesh by minimizing harmonic energy [59],

$$E_{harm}[h] = \frac{1}{2} \sum_{\{i,j\} \in Edges(D)} k_{i,j} ||h(i) - h(j)||^2, \tag{4.6}$$

where D is the 3D mesh and h is the conformal map. It can be interpreted as the energy of a configuration of springs with one spring placed along each edge of D. And the spring constants $k_{i,j}$ is defined as,

$$k_{i,j} = -\frac{1}{2}(\cot \angle\alpha + \cot \angle\beta), \tag{4.7}$$

where α, β are the two angles opposite to an edge $\{i, j\}$ in the two faces sharing the edge. Gu and Yau proposed a non-linear algorithm to minimize the harmonic energy [60]. If h is harmonic, the tangential component of the Laplacian at any point v of a surface is zero, and constraints are added to make the result unique [61].

We adopt Gu and Yau's algorithm to compute a conformal map over a sphere, which is a six dimensional Mobius transformation group [60]. It translates the mass center of a mesh to the origin to guarantee a unique mapping. For a non-convex shape in which a vector starting from the origin may intersect a surface more than once, the conformal mapping can converge to a valid mesh on a sphere without overlapping. Thus we avoid the ambiguity problem associated with EGI approaches. Nevertheless, a conformal map over a sphere is limited to genus-zero shapes only. As for non-zero genus shapes, they have to be cut open and mapped onto a plane [60].

4.3 Spherical Normal Image

Normal vectors have been used as geometric features in many shape analysis approaches. They contain rich geometric information of the object. Tasdizen et al. used normal vectors to smooth and reconstruct the original 3D object [62]. Gaussian map based Extended Gaussian Image (EGI) is another example of using normal vectors. EGI is translation-independent and has been widely used for classification [41]. The constraints of EGI, however, lie in its mapping properties of ambiguity and self-occlusion on non-convex objects. In other words, different non-convex shapes may be mapped to the same EGI, and part of the surface may not contribute to EGI mass on the sphere. Fig. 4.2 shows 2D contours of two 3D objects on the left and right, with their common EGI in the middle.

To solve this problem, distributed EGI and complex EGI have been developed to include more geometric information into EGI [63].

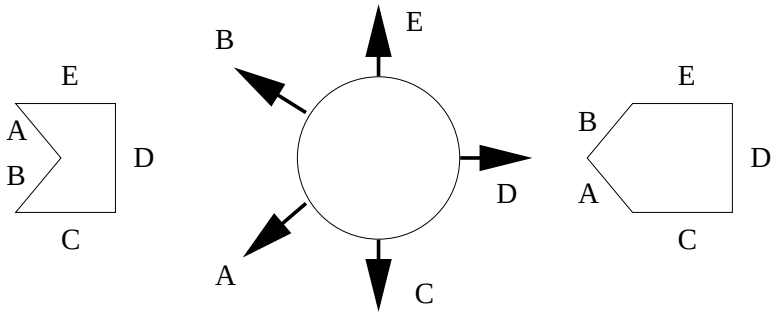

Figure 4.2: A non-convex object maps to the same EGI as a convex object, shown in 2D contour.

In our approach, we take normal vectors $\vec{N} = \{N_x, N_y, N_z\}$ as the geometric feature and store them in a conformal map over a unit sphere. SNI is generated by interpolating grids of longitude and latitude. We use Gnomonic mapping to interpolate a grid point P inside a spherical triangle ABC,

$$P = \frac{uA + vB + wC}{||uA + vB + wC||}, \tag{4.8}$$

where $0 \leq u, v, w \leq 1$ and $u + v + w = 1$. And P is given the same normal vector as that of the original triangle ABC. To illustrate, we show $\{N_x, N_y, N_z\}$ as $\{R, G, B\}$ color for shape models in Fig. 4.3.

Compared with geometry image, SNI incurs less distortion by mapping a closed surface onto a sphere [39]. Without cutting meshes open, it also avoids the variance resulted from different cutting paths among similar shape models. Compared with the spherical parameterization proposed by Praun and Hoppe, which minimizes stretch between an original mesh and the mapped mesh on a sphere [64], SNI is based on a conformal map that preserves angles and local shapes. And SNI does not need mapping from a sphere to a polyhedron or a unit square in [64], since further classification on the SNI is carried out directly over the sphere without unfolding.

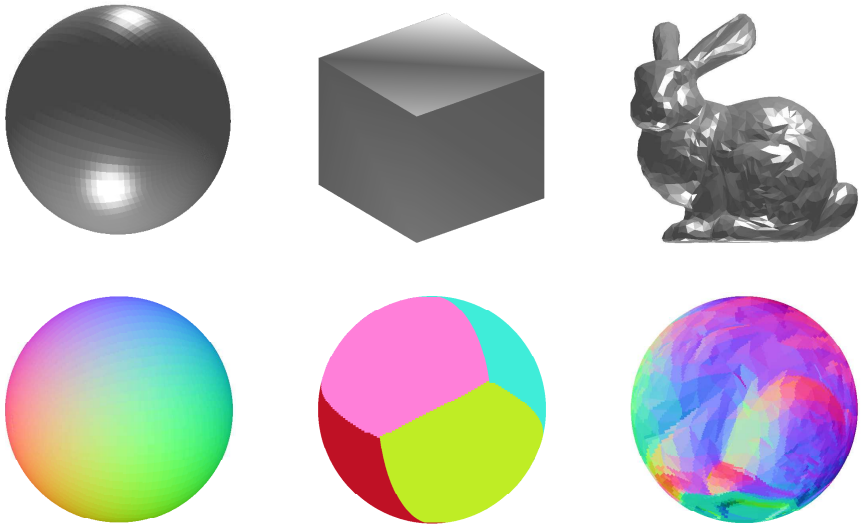

(a) Ball (b) Cube (c) Bunny

Figure 4.3: Original Models and their SNI.

4.4 Spherical Harmonic Representation

In section 4.3 we generated a new feature, spherical normal image (SNI), to represent a genus-zero shape. It is important that SNI preserves the crucial shape information of a 3D model, so that we can use it to discriminate various 3D models and find similar matches. In this section, a spherical harmonic representation of SNI is used to facilitate classification. And we also discuss multi-resolution support for coarse-to-fine classification.

Geometric features mapped onto the sphere, such as curvatures and normal vectors, have been used in similarity comparison of 3D objects in many recognition algorithms [34] [41]. They require the calculation of a composite distance between substantial corresponding vertices of objects mapped on sphere.

For shape classification, indexing geometric features on a sphere can facilitate comparison process. Schudy and Ballard used spherical harmonics (SH) to fit a surface as a function over a sphere [65]. In our approach, the geometric feature stored in a conformal map over a sphere, is regarded as a radial function $f : S^2 \rightarrow \Re$. It can be expanded as a linear combination of SH:

$$f(\theta,\phi)=\sum_{l=0}^{\infty}\sum_{m=-l}^{l}C_l^m Y_l^m(\theta,\phi), \tag{4.9}$$

where $Y_l^m(\theta,\phi)$ is the SH and the coefficients C_l^m are uniquely determined by

$$C_l^m=\int_0^{\pi}\int_0^{2\pi}Y_l^{m*}(\theta,\phi)f(\theta,\phi)\sin\theta d\phi d\theta. \tag{4.10}$$

The original spherical function is therefore decomposed by a feature vector of coefficient C_l^m. Fig. 4.4 illustrates the amplitudes of SH functions for $K=0,1,2,3$ [3].

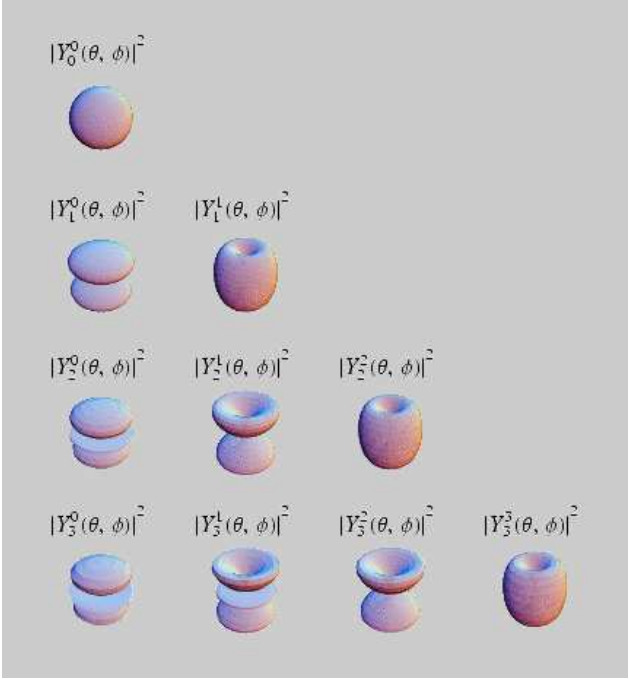

Figure 4.4: The amplitudes of SH function for $K=0,1,2,3$ [3].

We use SH decomposition of SNI to facilitate shape classification process. The feature vector is constituted by SH coefficients C_l^m. In practice, we use the amplitudes of C_l^m in the feature vector and exclude those with $m<0$ because of symmetries between C_l^m and C_l^{-m}. As $N_x^2+N_y^2+N_z^2=1$, the SH representation of N_z

is regarded as a redundancy and omitted. Therefore, the dimension of the feature vector is $(K+2)(K+1)$, where K is the highest order of SH. Feature vectors of a ball, cube and bunny with $K=1$ are shown in Table 4.1.

		Ball	**Cube**	**Bunny**
N_x	C_0^0	0.00243288	2.62533e-17	0.558153
	C_1^0	0.00178926	6.59502e-17	0.09185
	C_1^1	1.24949	0.8149	0.661967
N_y	C_0^0	0.000376667	5.03471e-17	0.297591
	C_1^0	0.000429478	8.03768e-17	0.0311241
	C_1^1	1.5204	1.19423	1.001

Table 4.1: The feature vectors of a ball, cube and bunny with $K=1$

Residual error Err is introduced by the truncation of higher orders of SH in practice,

$$Err(K) = \sum_{l=K+1}^{\infty} \sum_{m=-l}^{l} C_l^m Y_l^m(\theta, \phi), \tag{4.11}$$

which decreases with the increase of the value of K, the highest degree of SH. Using finite SH coefficients C_l^m is equivalent to apply a low pass filtering, whose level is controlled by the K value.

In computing spherical harmonics, Li and Hero compared methods of singular value decomposition (SVD) and FFT [35]. SVD methods can be applied to arbitrarily distributed sampling points, while FFT methods require uniform sampling on latitude θ and longitude ϕ. Nevertheless, both methods give similar estimation accuracy on same sampling data sets. Moreover, the complexity of SVD methods is approximated as $O(N^3)$, while that of FFT methods is $O(Nlog^2N)$ [66], where N is the number of sampling points.

However, it is the complexity of online computation of coefficients C_l^m, not that of computing spherical harmonics, determines response time of online retrieval.

We use a SVD method to compute SH offline and only need to compute SH coefficients C_l^m for online retrieval to shorten response time. In appendix C we show that both SVD and FFT methods have same complexity in online computation.

Multi-resolution meshes are desired for a coarse-to-fine classification. Dense meshes contain highly detailed geometric information, which might be redundant for coarse classification. They also incur excessive computation in the stage of mapping and feature extraction. Coarse meshes with basic geometric features are used for first level classification; denser meshes with more detailed geometric features for further classification.

Zhang and Hebert proposed a multi-scale classification approach [67]. It adopts smoothed discrete curvature as local geometric feature. By varying the level of surface smoothing, it compares the general shape similarity of two objects. This method, however, loses many geometric features by smoothing surfaces in low scale. Without smoothing the original surface, progressive mesh approach proposed by Hoppe satisfies the need of multi-resolution support better [68]. It uses a simple mesh M_0 to represent an arbitrary mesh $\hat{M}$, together with a sequence of edge split records. To optimize the original mesh, an energy metric is introduced,

$$E(M) = E_{dist}(M) + E_{spring}(M) + E_{scalar}(M) + E_{disc}(M), \tag{4.12}$$

where $E_{dist}(M)$ equals to the sum of squared distances from points $X = \{x_1, \cdots, x_n\}$ to the mesh, $E_{spring}(M)$ is the sum of spring energy placed on each edge, $E_{scalar}(M)$ measures scalar attributes, and $E_{disc}(M)$ measures geometric accuracy of its discontinuity curves. Then it adopts edge collapse to minimize the energy.

We adopt the progressive mesh in our approach. And the size of feature vector is scalable to multi-resolution meshes, i.e. a shorter feature vector is used in coarse classification and longer vector in fine classification. This scalability is achieved by varying the highest SH order K.

4.5 Self Organizing Map

After feature vectors are obtained, we adopt a self-organizing map (SOM) to classify 3D shape models [4]. Classifier selection is usually determined by sample data available and the specific application. Our research is focused on feature extraction that is not limited to specific classifiers. Nevertheless, we have to check classification performance to improve the design of feature extraction process. We adopt self-organizing map (SOM) due to following reasons: (1) our shape meshes are collected from the Internet, which are not pre-classified; (2) the definition of shape class is subjective or fuzzy, for example, how to classify the sphere, cube, cone, tetrahedron and cylinder?

Self-organizing map is an excellent tool in exploratory phase of data mining [4]. It is a two-level approach, of which the first level is a large set of prototypes – much larger than the expected number of clusters. The prototypes are then combined to form actual clusters as shown in Fig. 4.5 [4].

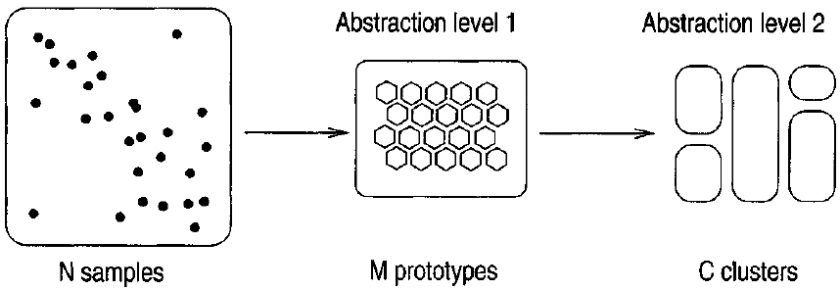

Figure 4.5: Two abstraction levels of SOM method. The first level is the set of prototype vectors. Using SOM to cluster the first level to get the second level. [4]

Usually the prototypes are arranged in 2D grid and each of them is represented by a prototype vector $\overrightarrow{M_i} = [M_{i1}, \cdots M_{id}]$, where d is the input vector dimension. At each training step, distance between sample data $\overrightarrow{X}$ and all the proto-

type vectors are computed. The best-matching unit (BMU), b, is the one with prototype vector closest to $\overrightarrow{X}$,

$$||\vec{X} - \overrightarrow{M}_b|| = \min_i\{||\overrightarrow{X} - \overrightarrow{M}_i||\}. \tag{4.13}$$

And then the BMU and its topological neighbors are moved closer to the input vector in the input space,

$$\overrightarrow{M}_i(t+1) = \overrightarrow{M}_i(t) + \alpha(t)h_{bi}(t)[\overrightarrow{X} - \overrightarrow{M}_i(t)], \tag{4.14}$$

where $\alpha(t)$ is an adaptation coefficient and $h_{bi}(t)$ is neighborhood prototypes centered on the BMU. The $h_{bi}(t)$ is computed as,

$$h_{bi}(t) = \exp(-\frac{||\vec{R}_b - \overrightarrow{R}_i||^2}{2\sigma^2(t)}), \tag{4.15}$$

where $\sigma(t)$ is a coefficient like $\alpha(t)$, and $\overrightarrow{R}_b$ and $\overrightarrow{R}_i$ are positions of prototype b and i on the SOM grid.

To visualize SOM result, the most widely used method is distance matrix. The unified distance matrix, U-matrix, shows distance between prototype vectors of neighboring map units. It can be visualized by gray shade or color. We adopt U-matrix in our experiments.

4.6 Experiments and Discussions

We collect 3D models from various sources on the Internet, with acknowledgment to SAMPL in Ohio State University [69], Princeton Shape Benchmark [70], Vranić's 3D Model Database [71] and Stanford 3D Scanning Repository [72]. Unfortunately, current 3D model benchmark [70] is not applicable to our approach due to the limit of genus-zero objects at present.

We extract feature vectors of 214 models with the highest SH order $K = 16$, and use a SOM Matlab toolbox [73] to get the result of 12×6 prototypes in Fig. 4.6.

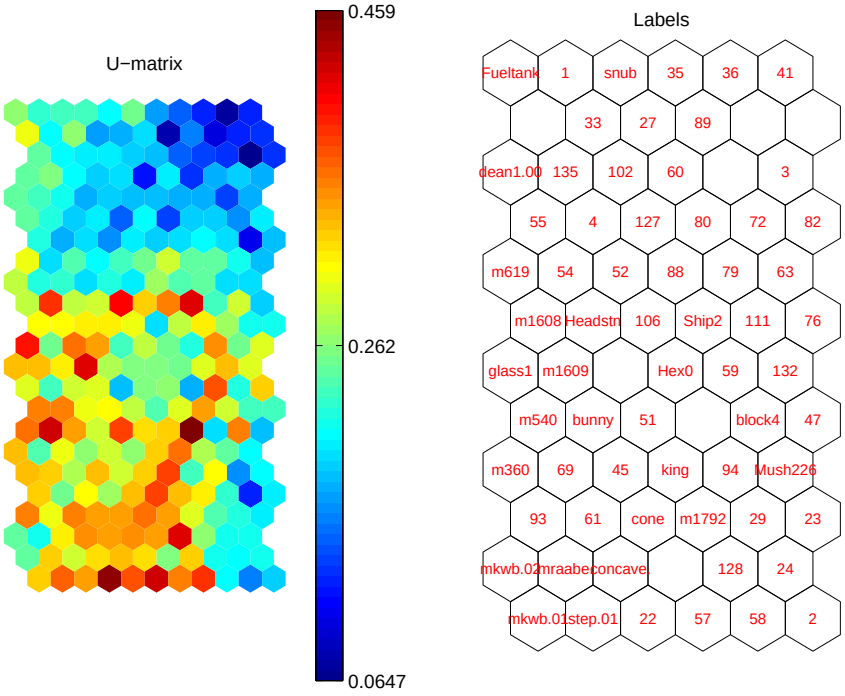

Figure 4.6: Shape classification result by SOM.

The left side of Fig. 4.6 is a U-matrix marked by different colors, while the right side are prototypes with different labels. Blank label means no feature vector presents in the prototype. As U-matrix displays distance between prototype vectors, feature vectors with smaller distance means more similarity between the according 3D shape models. And similar shape models should be clustered into the same or close prototypes. By checking into prototypes, we find our method picks up similar 3D models very well as shown in Fig. 4.7.

To compare the results of different feature vectors, we generate spherical curvature images (SCI) and spherical geometry images (SGI) in a way similar to SNI as shown in Fig. 4.8. Curvature inside a mesh polygon is computed by interpolating curvature at polygon vertices. And SGI is computed by interpolating normalized $\{X, Y, Z\}$ coordinates at polygon vertices. The method using SCIs requires dense meshes and classifies cubes and balls into one prototype, whose SCIs resemble with symmetries along X, Y, Z axes and large areas of constant curvature value. In con-

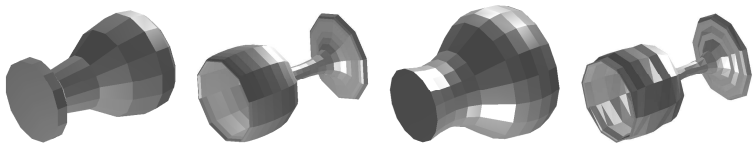

(a) Models in prototype labeled 'glass1'

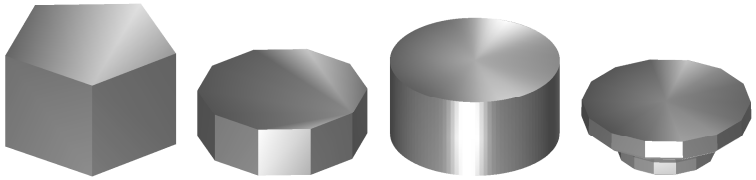

(b) Models in prototype labeled '23'

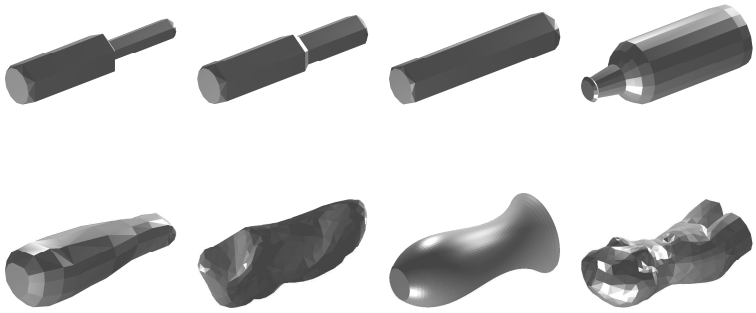

(c) Models in prototype labeled 'Hex0'

Figure 4.7: The 3D models in the prototypes.

trast, methods using SGIs and SNIs do not depend so much on mesh resolution and can discriminate cubes and balls correctly. The method using SGIs yields occasional "bad" classification compared with that using SNI. For example, a glass is found in the prototype of cubes because its SGI is not distinctive from those of cubes.

The result of pose alignment can affect feature vectors and final classification results. For example, for cuboids of $1:1:1$ ratio in different initial poses, the PCA method gives inconsistent rotations as shown in Fig. 4.9(a). Cuboids with $5:1:1$ ratio are given inconsistent rotations along X axes in Fig. 4.9(b). Only those with different ratio along X, Y, Z axes in Fig. 4.9(c) are registered consistently. The pose variance of objects after registration decreases with asymmetries along X, Y, Z axes

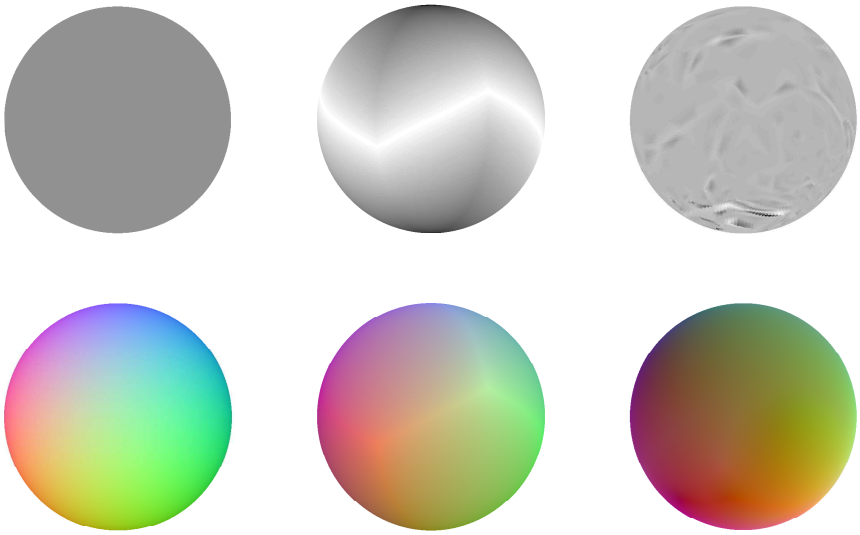

(a) Ball (b) Cube (c) Bunny

Figure 4.8: SCI (top) and SGI (bottom).

increase, which is an artifact of registration using PCA methods. Nevertheless, the effect of rotation on feature vectors is limited as shown in the experiments. The feature vectors of seven cubes are clustered into the prototypes labeled as '1', '33', and '135', which are very close according to the U-matrix in Fig. 4.6.

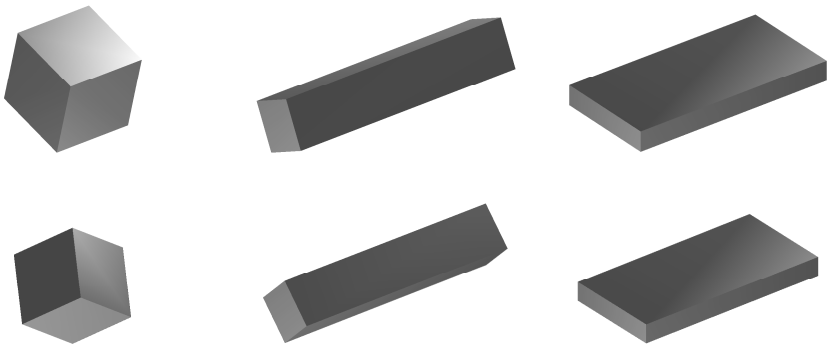

(a) 1 : 1 : 1 (b) 5 : 1 : 1 (c) 10 : 5 : 1

Figure 4.9: The pose alignment results of cuboids.

As for multi-resolution representation, we have generated different resolution meshes of same objects using Hoppe's algorithms [68], such as bunnies in Fig. 4.10(a) and 4.10(b). The multi-resolution meshes of same objects are clustered into same prototypes. It demonstrates that our method is robust to mesh resolution.

The SH representation is also used by Kazhdan et al. in their voxelized model with $64 \times 64 \times 64$ grids [7]. Fig. 4.10(c) shows the voxelized bunny of $15,377$ cubes from the bunny of $4,000$ triangles in Fig. 4.10(a). Though using a much larger data size, Fig. 4.10(c) loses many fine details of Fig. 4.10(a) before SH representation, which is also addressed in [37]. Based on a surface based model, the proposed method needs much smaller data size to present at least same level of surface details.

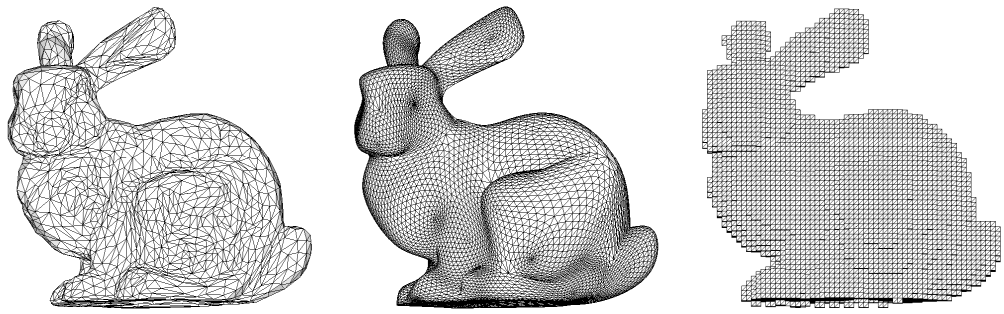

(a) Original Surface (b) High Resolution (c) Voxelized Model

Figure 4.10: Bunnies with different resolutions.

CHAPTER 5

GENERAL SHAPE ANALYSIS

In Chapter 4 we discussed shape classification by the spherical normal image (SNI) based method. SNI preserves local geometric features using conformal mapping on unit sphere and is unique to each 3D shape. The proposed SNI based method discriminates collected shapes well in the experiments. However, due to the limit of conformal mapping on sphere, SNI only applies to genus-zero objects, which are sphere-like without holes or handles. To apply the SNI based method to general shapes, we need to convert them to genus-zero objects first. Sphere-like mesh wrapped onto the original object is a possible solution [34]. Nevertheless, shape estimation error is introduced during reconstruction of original surface.

In this chapter, we are going to analyze general 3D shapes. We will review classification methods for general shapes briefly. A new shape descriptor based on 4D hyperspherical harmonics (HSH) is proposed and compared with existing descriptors. The shape classification process using proposed 4D HSH descriptor involves voxelization, conversion grids from Cartesian coordinates to Polar coordinates, feature extraction and classification using support vector machine (SVM), as shown in Fig. 5.1. We also discuss shape matching and conduct experiments to classify and retrieve 3D shapes from shape benchmarks.

5.1 Introduction

As discussed in Section 1.2.2, many methods have been proposed for shape classification and matching. To apply these methods to general shapes, however, geometric features or processes should not be limited to specific classes of shapes.

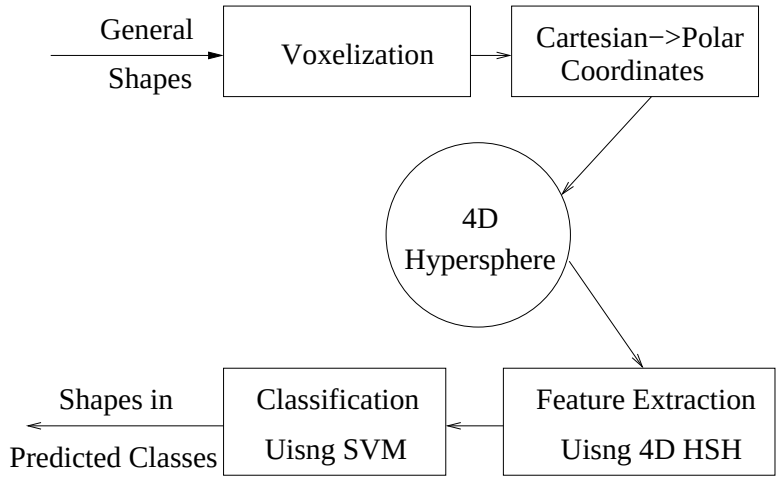

Figure 5.1: The procedure of general shape classification using 4D HSH and SVM.

For example, many spherical parameterization based methods require objects to be genus-zero, which are closed surfaces without holes or handles [64].

We will briefly introduce popular shape classification and matching methods for general shapes in the following sections.

5.1.1 Shape Distribution

Shape distribution methods use statistic geometric properties which can apply to general shapes [5]. For example, distance D_2 refers to the distance between two random points on a 3D object. The D_2 histogram is then used as a shape descriptor in discriminating different 3D shapes.

However, shape distribution based methods do not discriminate well objects with similar gross shape but vastly different detailed shape properties [31]. Fig. 5.2 illustrates shape distribution of two classes of shapes, tanks and cars [5]. As their gross shapes are similar, their shape distributions are difficult to be discriminated.

Extended Gaussian Image (EGI), which uses the histogram of normal vectors, is known to be ambiguous to non-convex objects, as shown in Fig. 4.2.

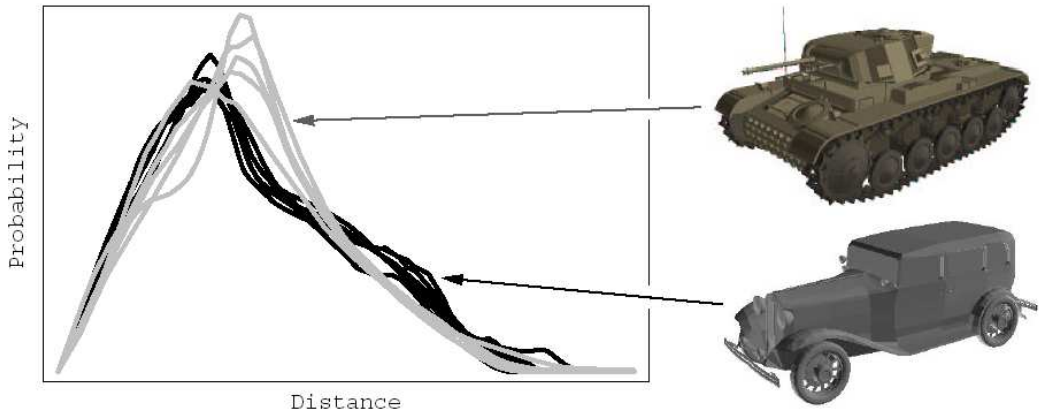

Figure 5.2: Shape distribution of 5 tanks (gray) and cars (black). The figure is from [5].

5.1.2 Concentric Spheres Model (CSM)

Kazhdan et al. proposed a concentric sphere model and used rotation invariant SH representation as the geometric feature for shape classification [7] [74]. They first converted a given surface model into a volume model in $2R \times 2R \times 2R$ voxel grid. A voxel is assigned value one if it intersects with the given surface, otherwise it is assigned a value zero. Then the volume is intersected with R concentric spheres. An illustration of the voxelization and intersection procedure is shown in Fig. 5.3 by Vranić [6].

Recall from equation (4.9), the intersection of the volume with each sphere can be viewed as a spherical function represented by SH. The amplitudes of SH representation are used as the final shape descriptor,

$$SH(f) = \{||f_0(\theta,\phi)||, ||f_1(\theta,\phi)||, ...\}, \tag{5.1}$$

where f_l is the frequency component of f,

$$f_l(\theta,\phi) = \sum_{m=-l}^{l} C_l^m Y_l^m(\theta,\phi). \tag{5.2}$$

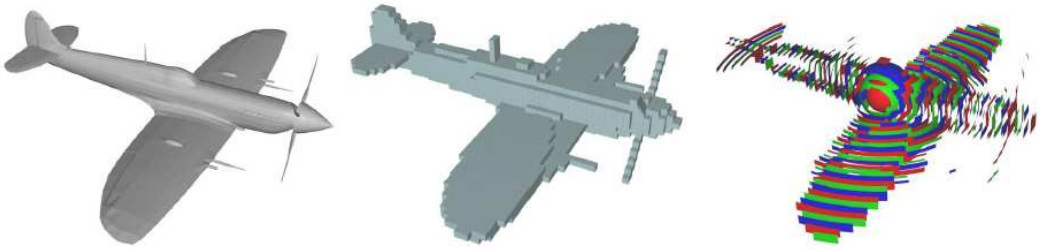

Figure 5.3: The voxelization and intersection procedure of concentric spheres model (CSM). Figure on the left is the original surface based model, while that in the middle is voxel based model. And the figure on the right is the result after intersection with concentric spheres model. The figure is from [6].

With the definition in equation (5.1), the shape descriptor is independent of the orientation of the spherical function,

$$SH(R(f) = SH(f), \tag{5.3}$$

where R can be any rotation matrix [7]. In other words, we do not need to eliminate rotation invariance in pose alignment since same objects in different rotation have same shape descriptors. This rotation invariant property gives concentric spheres model an advantage over methods requiring rotation elimination.

5.2 4D Spherical Harmonics Model

The concentric spheres model cuts a 3D object along radii into spheres. It raises a problem that, if inner parts are rotated around the center, the shape descriptor will not change at all. This is because the shape descriptor uses amplitudes of SH representation which are rotation invariant according to equation (5.3). For example, two different shapes in Fig. 5.4 have same shape descriptors [7]. The rotation invariant property makes concentric spheres model ambiguous to shapes with rotation of internal parts.

As rotation invariant property is desirable, we propose to eliminate this ambiguity by treating a 3D object as a whole without cut along radii. Instead of using

Figure 5.4: The right object is obtained by applying a rotation to the inter part of the plane on the left. The figure is from [7].

concentric spheres model, we map the 3D object to a 4D unit sphere for analysis. Accordingly we need 4D hyperspherical harmonic (HSH) to decompose the 3D object and derive its shape descriptor.

5.2.1 Voxelization

Before we explore mapping relations between 3D and 4D space, let us examine the voxelization step in Fig. 5.1 first. As most of current available 3D models are represented by polygonal meshes, which are surface based. The concentric spheres model (CSM) based shape descriptor and the proposed 4D HSH shape descriptor both require voxel based models. In other words, analysis is carried out on fixed number of voxels, not polygons. We need to convert surface based model into voxel based model, which is called the voxelization process.

The voxelization process is in reversed direction of surface construction process we discussed in Chapter 2, in which we construct surface based models from volumetric data. Many voxelization methods have been proposed for various usage [75] [76]. Schroeder and Lorensen proposed to compute distance function for the generation of swept surfaces and volumes using implicit modeling [77]. Dachille and Kaufman limited the computation to voxels close to triangular meshes [78]. And Nooruddin and Turk used voxelization techniques to simplify and repair polygonal meshes [79].

As we only need to assign value one to voxels intersecting an input surface, a simplified voxelization method can be adopted. We test each polygon in a surface based 3D model to mark those voxels that have vertices at the both sides of the polygon. To speed up the process, we only consider voxels that are close to the polygon, similar to the distance criteria in [78]. Moreover, if the polygonal mesh is coarse, we need to subdivide the mesh into smaller ones.

In our experiments, we convert surface models into voxel grids with size of $64 \times 64 \times 64$, the same size as the one used in experiments of concentric spheres models [80]. Fig. 5.5 illustrate the voxelization results of surface based models.

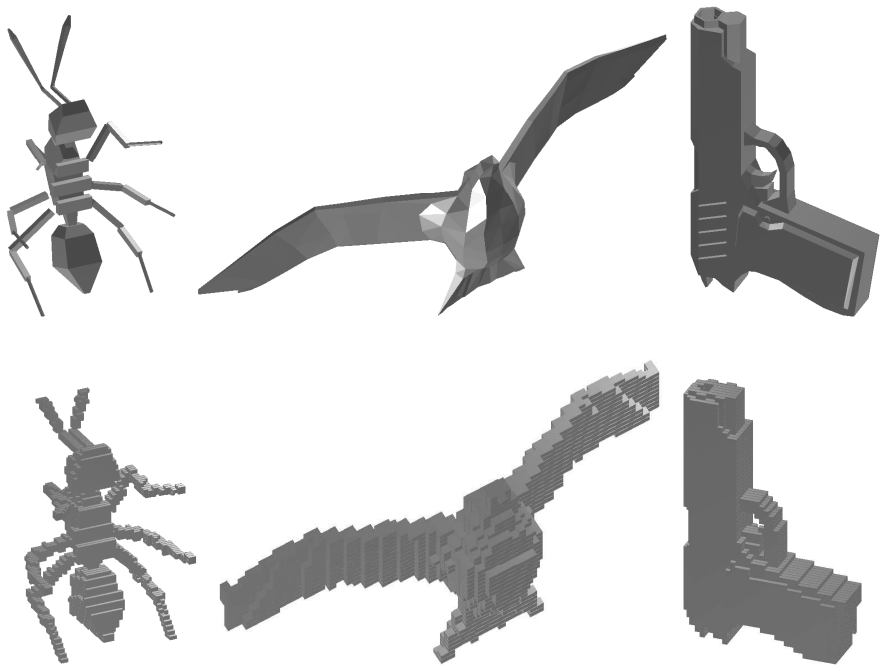

Figure 5.5: Surface based models and voxel based models.

Unlike concentric spheres models (CSM) shown in Fig. 5.3, we do not cut the object along radii to compute intersections of the objects with spheres.

5.2.2 Coordinates Conversion

Similar to 3D unit sphere, a 4D unit sphere satisfies $r = 1$ where r is the distance to origin in 4D space. To understand 4D objects and space intuitively, Murata and Hashimoto proposed an interactive environment [81]. In high dimensional space spherical harmonics, or hyperspherical methods, have been explored to analyze n-body quantum systems [82] [83]. Matheny et al. adopted 4D spherical harmonics for time-dependent shape recovery and representation [84]. The 4th dimension in their approach is time, not the 4th space dimension in our case.

Similar to 3D spherical coordinates, 4D hyperspherical coordinates r, θ_0, θ and ϕ, are connected to Cartesian coordinates as,

$$\begin{aligned} x &= r\sin\theta_0\sin\theta\cos\phi \quad & y &= r\sin\theta_0\sin\theta\sin\phi \\ z &= r\sin\theta_0\cos\theta & z_0 &= r\cos\theta_0 \end{aligned} \tag{5.4}$$

where θ_0 and z_0 are the $4th$ dimensional coordinates. To compute hyperspherical coordinates, we have,

$$\begin{aligned} r^2 &= x^2 + y^2 + z^2 + z_0^2 \quad & \theta_0 &= ar\cos\frac{z_0}{r} \\ \theta &= \arctan\frac{\sqrt{x^2+y^2}}{z} & \phi &= \arctan\frac{y}{x} \end{aligned} . \tag{5.5}$$

5.2.3 Feature Exaction using 4D HSH

Similar to spherical functions represented by 3D harmonics in equation (4.9), a hyperspherical function on 4D unit sphere can be decomposed as,

$$f(\theta,\phi,\theta_0) = \sum_{\lambda=0}^{\infty}\sum_{l=0}^{\lambda}\sum_{m=-l}^{l} C_{\lambda,l}^{m} Y_{\lambda,l}^{m}(\theta,\phi,\theta_0), \tag{5.6}$$

where $Y_{\lambda,l}^{m}(\theta,\phi,\theta_0)$ is the 4D harmonics. It can be computed using 3D harmonics $Y_l^m(\theta,\phi)$ as,

$$Y^m_{\lambda,l}(\theta,\phi,\theta_0) = N_{\lambda,l} C^{l+1}_{\lambda-l}(\cos\theta_0)\sin^l\theta_0 Y^m_l(\theta,\phi), \tag{5.7}$$

where

$$N_{\lambda,l} = (-1)^\lambda i^l (2l)!! \sqrt{\frac{2(\lambda+1)(\lambda-l)!}{\pi(\lambda+l+1)!}}, \tag{5.8}$$

and Gegenbauer polynomial $C^\alpha_\lambda(u)$ is computed as,

$$C^\alpha_\lambda(u) = \sum_{t=0}^{[\lambda/2]} \frac{(-1)^t\Gamma(\lambda+\alpha-t)}{t!(\lambda-2t)!\Gamma(\alpha)}(2u)^{\lambda-2t}, \tag{5.9}$$

in which Gamma function $\Gamma(n) = (n-1)!$ [83][85].

Similarly the shape descriptor is defined as,

$$HSH(f) = \{||f_{0,0}(\theta,\phi,\theta_0)||, ||f_{1,0}(\theta,\phi,\theta_0)||, ...\}, \tag{5.10}$$

where $f_{\lambda,l}$ is the frequency component of f,

$$f_{\lambda,l}(\theta,\phi,\theta_0) = \sum_{m=-l}^{l} C^m_{\lambda,l} Y^m_{\lambda,l}(\theta,\phi,\theta_0). \tag{5.11}$$

Note that rotation in 3D space only involves θ and ϕ. Therefore the new shape descriptor is still independent of rotation in 3D space as depicted by equation (5.3).

In practice, the highest degree of HSH, K, is not infinite but truncated to some finite value. Residual error is therefore introduced,

$$Err(K) = \sum_{\lambda=K+1}^{\infty} \sum_{l=0}^{\lambda} \sum_{m=-l}^{l} C^m_{\lambda,l} Y^m_{\lambda,l}(\theta,\phi,\theta_0), \tag{5.12}$$

which decreases with the increase of the highest degree of HSH, K. And the length of 4D HSH shape descriptor is $(K+1)(K+2)/2$.

To compute 4D HSH coefficients $C_{\lambda,l}^{m}$, we adopt an approach similar to that in Section 4.4. The process uses singular value decomposition (SVD) to shorten online retrieval response time as presented in Appendix D.

5.3 Support Vector Machine (SVM)

To evaluate the effectiveness of different shape descriptors, we need a classifier to classify 3D shape samples into classes and then compare the results. In Section 4.5 we used self-organizing map (SOM) as the classifier. The main reason for this selection is that no pre-classified data is available for genus-zero shapes. Fortunately, several shape benchmarks provide pre-classified samples for general shapes [70] [71] [86]. Therefore we can select a classifier that takes advantage of the pre-classified samples. In our experiments, we adopted support vector machine (SVM) as the classifier.

SVM is a relatively new classification technique introduced by Vapnik et al. in early 1990s [87] [88]. It has become one of the most popular classifiers due to its superior performance in many applications. And it is an alternative to polynomial, radial basis function and multi-layer perception classifiers.

The main idea of SVM is to maximize the margin between the classes with a boundary. An example of linear classifier on two linearly separable classes is shown in Fig. 5.6. The boundary in Fig. 5.6(b) is better with a larger margin between the two classes.

SVM is derived from classical empirical risk minimization approach. Let us look at a two classes recognition example. The task of a learning process is to construct an appropriate set of decision functions $f_{\lambda}(x)$: $\Re^N \rightarrow \{-1, 1\}$, so as to minimize the expected overall risk,

$$R(\lambda) = \int |f_{\lambda}(x) - y| P(x, y) dx dy \tag{5.13}$$

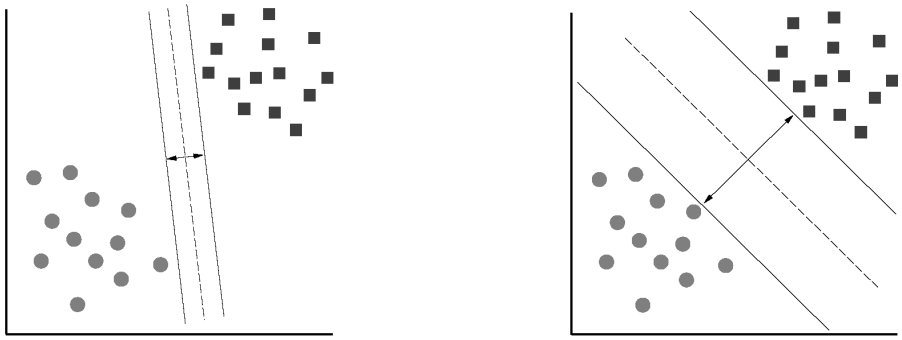

(a) (b)

Figure 5.6: (a) A separating hyperplane with a small margin. (b) A separating hyperplane with a larger margin. Solid dots and squares represent data in two classes. Dotted lines stand for the hyperplane boundary [8].

where $P(x, y)$ is the distribution of a feature vector $x \in \Re^N$ and its class $y \in \{-1, 1\}$. As distribution $P(x, y)$ is normally unknown, instead we compute an approximation of $R(\lambda)$, or empirical risk,

$$R_{emp}(\lambda) = \frac{1}{l} \sum_{i=1}^{l} |f_\lambda(x_i) - y_i|. \tag{5.14}$$

where (x_i, y_i), $i = 1, 2, ..., l$ are a set of known samples.

The validity of the empirical risk minimization approach requires that, when the empirical risk R_{emp} converges to minimum, the expected overall risk should converge to minimum. Vapnik and Chervonenkis gave an upper bound of expected overall risk, which holds with probability $1 - \eta$,

$$R_\lambda(\lambda) \leq R_{emp}(\lambda) + \sqrt{\frac{h(\ln \frac{2l}{h} + 1) - \ln \frac{\eta}{4}}{l}}, \tag{5.15}$$

where h is a non-negative integer called Vapnik Chervonenkis (VC) dimension [88]. From the bound, it is clear that to minimize expected overall risk R, besides a small empirical R_{emp} we also need to select an appropriate value of VC-dimension h.

The structural risk minimization (SRM) techniques proposed by Vapnik is to minimize both VC-dimension and empirical risk. Nevertheless SRM is very difficult to apply directly. One reason is VC-dimension is difficult to compute. Instead Vapnik associated VC-dimension with the margin of a linear classifier and proposed SVM algorithm to implement the SRM. Starting from linear classifier on linear separable problem, the SVM method provides a linear classifier on non-separable problem and then a non-linear classifier on non-separable problem [88] [8].

Originally the SVM method targets at two classes situation. To apply the SVM to multiple classes situation, one approach is to select any two classes and use SVM method to classify a given feature vector. After all the combinations of two classes have been tested, the feature vector is assigned to the class with highest number of SVM classification hits.

5.4 Shape Matching

The shape matching process of a query 3D shape model is to retrieve in the database for similar 3D shapes as the input. Similar to shape classification process in Fig. 5.1, the matching process differs only in the last step as shown in Fig. 5.7. The matched shape models are ranked by shape similarity.

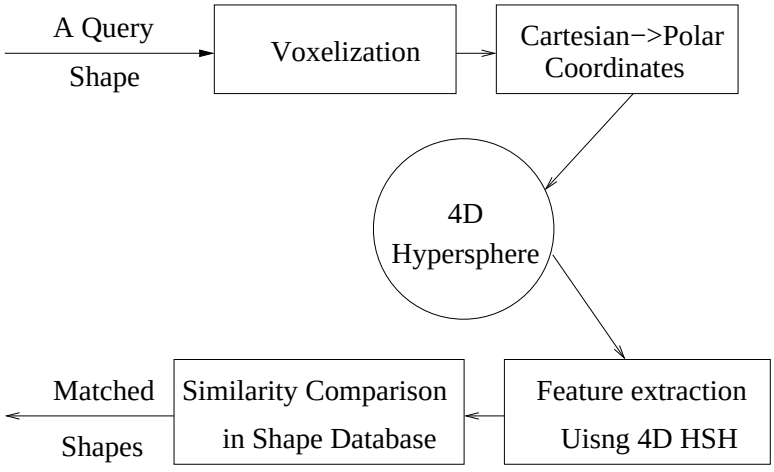

Figure 5.7: The procedure of general shape matching using 4D HSH.

Shape similarity comparison is based on the distance of 3D shapes. The more similar two shapes are, the shorter the distance is. For two 3D shapes A, B, aligned in the same coordination system, the sum of squared distances (SSD) from A to B is,

$$SSD_{AB} = \sum_{p \in A} dist_m^2(p, B), \tag{5.16}$$

where $dist_m(p, B)$ is the shortest distance from point p to B. SSD from B to A is defined similarly.

Direct computation of SSD between two 3D shapes involves a complicated integration over each point on the models. Instead, we compare shape similarity based on the distance of two shape descriptors. As shape descriptors are multiple dimensional vectors, we compute their L_2 difference as the distance,

$$\hat{D}_{AB} = ||HSH(f) - HSH(g)||^2 = \sum_{\lambda=0}^{\infty} \sum_{l=0}^{\lambda} (||f_{\lambda,l}|| - ||g_{\lambda,l}||)^2, \tag{5.17}$$

where f and g are hyperspherical (HSH) functions of model A and B respectively. Note that the L_2 difference between shape descriptors are a low bound of the L_2 difference between their HSH functions,

$$\hat{D}_{AB} \leq \sum_{\lambda=0}^{\infty} \sum_{l=0}^{\lambda} (||f_{\lambda,l} - g_{\lambda,l}||)^2 = ||f(\theta, \phi, \theta_0) - g(\theta, \phi, \theta_0)||^2. \tag{5.18}$$

It is simple to use L_2 difference between shape descriptors as distance. However, it disregards class information of the input shape and shapes in database. To take advantage of the class information, we propose a weighted distance,

$$WD_{AB} = W_{AB} \cdot ||HSH(f) - HSH(g)||^2, \tag{5.19}$$

where weight W_{AB} is assigned a smaller value if A and B belong to same class, or a larger one otherwise.

5.5 Experiments and Discussions

With more and more 3D models are available online, many 3D shape databases collected these shapes for various purpose [70] [69] [71] [86]. We use Princeton Shape Benchmark (PSB) which provides about 1,800 pre-classified shape samples [70]. It also provides some utilities for presentation and analysis.

5.5.1 Rotation Invariant

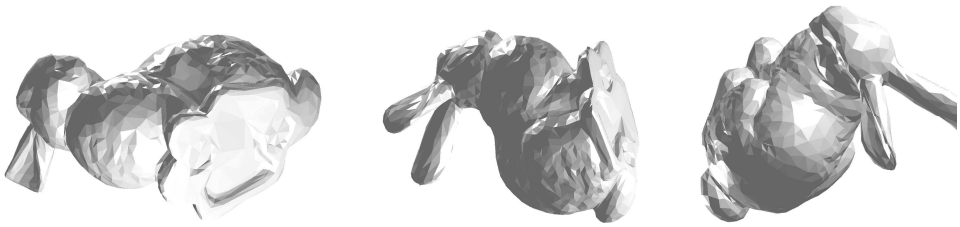

(a) Bunny 1 (b) Bunny 2 (c) Bunny 3

Figure 5.8: Bunny in three rotations.

To illustrate 4D HSH shape descriptor is rotation invariant, we generate bunny in three rotations as shown in Fig. 5.8. Their shape descriptors, HSH_1, HSH_2 and HSH_3 are presented in three columns in Table 5.1 and 5.2. From the table HSH_1, HSH_2 and HSH_3 are very close.

5.5.2 Shape Classification

To evaluate the effectiveness of 4D HSH shape descriptors, we select shape descriptors based on concentric spheres model (CSM) for comparison in the experiments.

To compare classification performance between different shape descriptors, it is important to use shape descriptors of the same length. Generally speaking, if other parameters are the same, the longer a shape descriptor is, the more discriminative it is.

The length of 4D HSH shape descriptor is $L_1 = (K_1 + 1)(K_1 + 2)/2$, where K_1 is the highest degree of 4D HSH. The length of CSM based shape descriptor is $L_2 = R \times (K_2 + 1)$, where K_2 is the highest degree of 3D SH and R is the number of concentric spheres. In our experiments, $K_1 = 8$, and $L_1 = 45$, so we set $R = 9$ and $K_2 = 4$, or $R = 5$ and $K_2 = 8$, in order to get $L_1 = L_2$. In the shape classification, we also use random vectors at the length of L_1 with elements value uniformly distributed over $[0, 1]$ for comparison.

We test the proposed 4D HSH shape descriptors on two sets of pre-classified sample data in Princeton Shape Benchmark [70]. The benchmark provides a training group of 907 samples and a testing group of 907 samples without overlap. Set 1 classifies samples into two coarse classes, artificial objects and natural objects. Actually classification in set 1 is not based on shape and we use it for comparison. Set 2 contains seven classes, vehicles, animals, households, buildings, furniture, and plants, which are shape-based. We generate shape descriptors of training shapes and use them to train a SVM classifier with a Gaussian kernel. The SVM classifier is implemented using a Matlab toolbox provided by Canu et al [89].

To verify the SVM implementation, we use it to analyze UCI Adult Census Data [90]. The UCI Adult Census Data is widely used as a benchmark for pattern classification and data mining tasks. It classifies adults with annual income into two classes, those with income greater than $\$50,000$ and those with less income. The first class takes 24.78% among all the samples while the other class takes 75.22%. There are $30,162$ samples as the training set and $15,060$ samples as the test set with 14 attributes including age, work class, education and occupation. For a test sample, if the prediction by the SVM classifier is in accordance with its pre-classified result,

we take it as a "correct" classification. The correct classification rate (CCR) is defined as the ratio of correct classified samples among all the test samples. Using 100 training samples to train the SVM classifier with a linear kernel, we get CCR = 82% for 15,060 test samples. We also use another SVM implementation SVM^{light} for comparison [91] [92] [93]. The CCR is 83% with a similar configuration. The experiment result is also in accordance with that by Li [94].

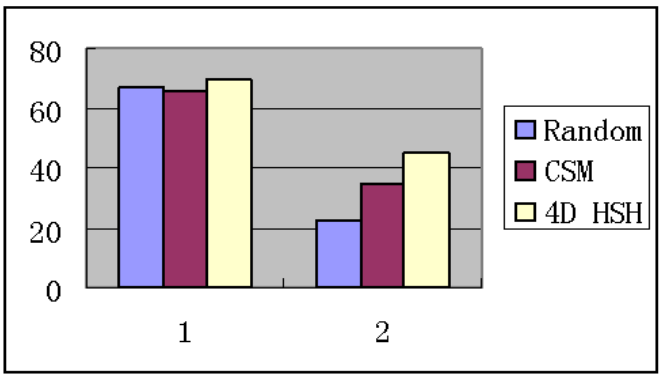

Figure 5.9: Classification performance on random, concentric spheres model (CSM), and 4D HSH shape descriptors. Y axis indicates correct classification rate in percents.

In the shape classification experiments, we generate shape descriptor for a test shape model and use it as input to SVM classifier. The CCR of the random, concentric spheres model (CSM) and 4D HSH shape descriptors on set 1 and 2 are illustrated in Fig. 5.9.

Obviously, the CCR decreases with the number of classes increases in the data set. In Fig. 5.9 the CCR for set 2 with seven classes is lower than that for set 1 with two classes. For set 1, CSM and 4D HSH shape descriptors have similar CCR as the random descriptor because they do not contain much information to decide whether objects are natural or artificial. For set 2, the CSM shape descriptor gives CCR= 34.95%, 55% higher than that of random descriptor. And the 4D HSH de-

scriptor gives CCR =45.90%, 29% higher than that of CSM descriptor. The 4D HSH shape descriptor performs better than CSM descriptor at the same length.

5.5.3 Shape Matching

An example of shape matching is illustrated in Fig. 5.10. With an input vehicle model, we retrieve top 11 matched models from the database using the proposed 4D HSH shape descriptor. From Fig. 5.10 the proposed method finds shapes in the same shape class as the input shape from the database successfully.

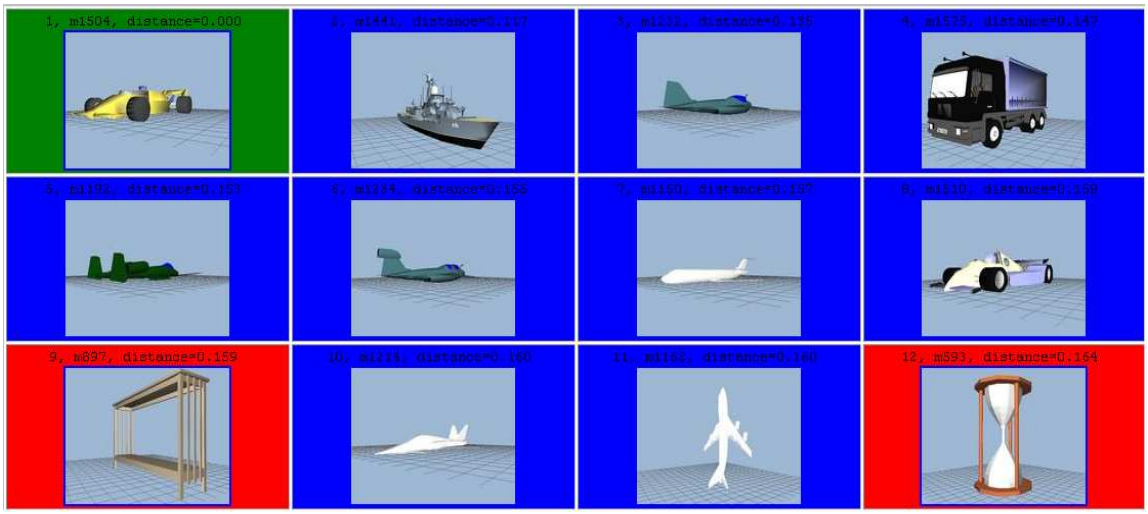

Figure 5.10: An input model and its top 11 matched models. The upper left with green frame is the input model, while the others are retrieved from database. Retrieved models with blue frame are in the same class as the input model, while those with red frame are not.

For an input 3D model in class C, suppose we retrieve M 3D models from the database which are most similar to the given model. Obviously, if the number of models retrieved M increases, we are more likely to get 3D models from the class C, while we might also get 3D models in other classes. To evaluate shape matching performance, we adopted the precision-recall curved as that in [7] [80]. The curve

plots "precision" in y direction, which is the ratio of M models that are in class C, and "recall" in x direction, which is the ratio of models in class C that are in the retrieved M models. For example, (0.2, 1.0) means the top shape match is in the same class as the input shape to reach precision 1.0, and the recall of 0.2 means the matched shape takes 20% of shapes in the input shape class. And (0.4, 0.5) indicates that 50% of retrieved shapes are in the same class of input shape while 40% of shapes in the input shape class are retrieved. An ideal matching result is a horizontal line at $y = 1$ indicating all the retrieved M models are in class C. Normally, precision decreases with recall increases. For two curves indicating two shape descriptors, the one at upper right means high precision for the same recall thus indicates better retrieval performance.

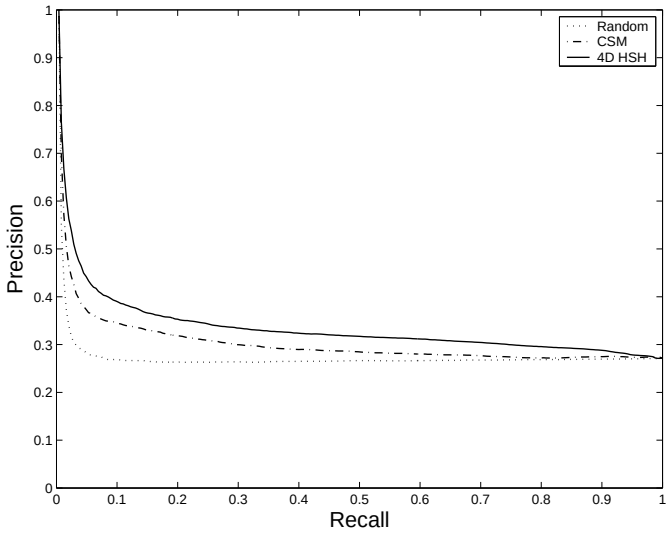

Figure 5.11: Recall and Precision curve of random, concentric spheres model (CSM), and 4D HSH shape descriptors for the vehicle class in Set 2. X axis is recall while Y axis indicates precision.

Using L_2 difference of shape descriptors as the distance between 3D shapes, we compute recall and precision values of each classes and all classes average in Set

2 for random, CSM and 4D HSH shape descriptors. Fig. 5.11 shows the recall and precision curve for vehicle class while the average for all classes is presented in Fig. 5.12.

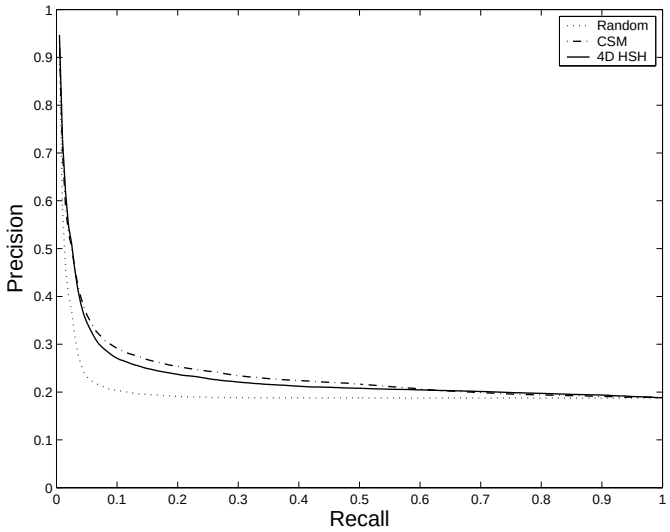

Figure 5.12: Recall and Precision curve of random, concentric spheres model (CSM), and 4D HSH shape descriptors for all classes average. X axis is recall while Y axis indicates precision.

From the recall and precision curve of vehicle classes in Fig. 5.11, 4D HSH shape descriptor performs better than CSM and random descriptors. At the average of all classes in figure 5.12, the precision of CSM shape descriptor at recall of 0.1 is 0.29, 45% higher than that of random (0.20). The precision of 4D HSH shape descriptor is 0.27 at the recall of 0.1, which is 93% of that of CSM descriptor.

4D HSH shape descriptor is rotation invariant Like CSM shape descriptor. However, with limited highest degree of HSH, K, estimation error is introduced. To improve shape matching performance, we conduct pose alignment to eliminate rotation invariance for a given shape before voxelization. The corresponding recall and precision curve shows small improvement in Fig. 5.13. For example, at recall of 0.1,

the precision of 4D HSH descriptor after shape registration is 0.30, 11% higher than that of 4D HSH descriptor without registration. It also suggests that using pose alignment to improve shape matching performance of rotation invariant shape descriptors is limited.

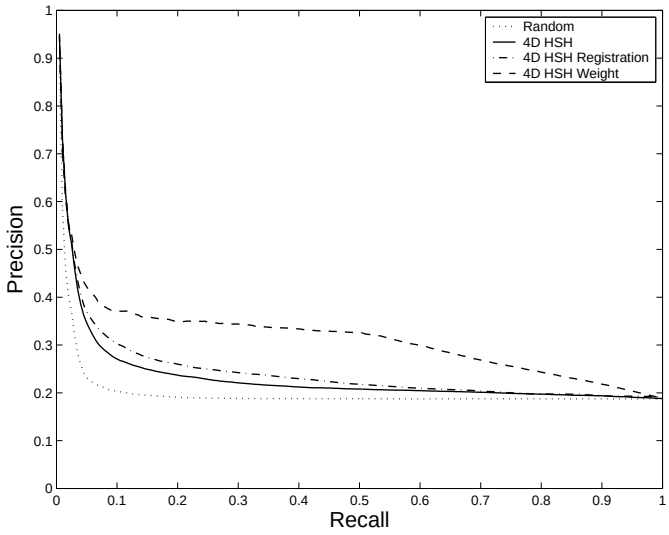

Figure 5.13: Recall and Precision curve of for all classes with improvement by pose alignment. X axis is recall while Y axis indicates precision.

To improve the matching performance, we integrate classification results into the distance measurement. And the precision and recall curve favors shorter distance between shapes in the same class while longer distance between shapes from different classes. From equation (5.19), we assign distance weights based on SVM classifier prediction. If two shapes are predicted to be in the same class, we use a smaller weight to shorten their distance, or a larger weight enlarge their distance otherwise. The corresponding recall and precision curve shows obvious improvement as in Fig. 5.13. For example, at recall of 0.1, the precision of the weighted distance 4D HSH descriptor is 0.37, 37% higher than that of 4D HSH descriptor without weight. Fig. 5.15 shows another example of input model and its top 19 matches.

From the calculation of recall and precision, the recall and precision curve is directly depend on the definition of class. Different class definition will generate totally different curve for the same distance measurement. For example, the same distance measurement in Fig. 5.12 using class definition in Set 1 instead of Set 2 will generate recall and precision curve in Fig. 5.14.

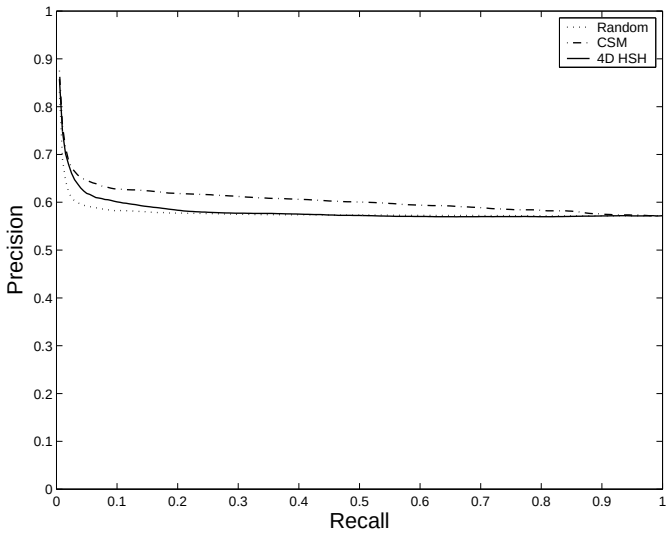

Figure 5.14: Recall and Precision curve of random, concentric spheres model (CSM), and 4D HSH shape descriptors for shapes in Set 1. X axis is recall while Y axis indicates precision.

Note in our comparison with CSM shape descriptors, we limit its size L to 45, the same as that of 4D HSH shape descriptors. As $L = R \times (K + 1)$, we use either $R = 9, K = 4$ or $R = 5, K = 8$, while in practice $L = 512$ with $R = 32$ and $K = 15$ [70]. The correct classification rate (CCD) is 43% for CSM shape descriptor when $L = 512$ in our experiments. Besides 3D SH representation, we did not use other optimization method in [7] [70]. As a result, our results including recall and precision curves are different from those in [70].

The limit of shape descriptor length for 4D HSH lies in the way we compute 4D HSH. SVD method is used to compute 4D HSH coefficients $C_{\lambda,l}^{m}$ as presented in Appendix D. We need to compute a pseudo inverse matrix Y^{-1}, which is of size $\frac{(K+1)(K+2)(2K+3)}{6} \times N$. The computation complexity grows quickly with (θ, ϕ, θ_0) grid size and K. For example, for a $(\theta_i, \phi_i, \theta_{0i})$ grid of size $20 \times 20 \times 20$ and $K = 8$, the size of Y is 8000×285. It takes about 31 minutes on a Pentium 4 $3.2GHZ$ machine with $1G$ RAM. Though this step can be completed offline once for all, it still limits the size of $(\theta_i, \phi_i, \theta_{0i})$ grid, K and the length of 4D HSH shape descriptor L, which is of size $\frac{(K+1)(K+2)}{2}$. To reach $L = 512$ as used in [70], we need $K = 30$. As a result, the size of Y with the same grid size as 20 becomes 8000×10416, which is very expensive to compute using SVD. To generate longer shape descriptor, we may need new method to compute 4D HSH coefficients $C_{\lambda,l}^{m}$.

Bunny 1	Bunny 2	Bunny 3
0.076193	0.07879	0.073858
1.30e-15	1.19e-15	5.51e-16
0.018489	0.009033	0.02647
0.124278	0.138426	0.139562
1.41e-16	1.36e-16	3.23e-16
0.082299	0.057327	0.04291
7.91e-16	9.20e-16	9.45e-16
0.022186	0.022135	0.064738
1.92e-16	2.30e-16	2.58e-16
0.058485	0.035637	0.022967
0.043827	0.053012	0.065833
1.23e-16	2.01e-16	1.69e-16
0.176636	0.147784	0.124835
2.48e-16	3.49e-16	2.49e-16
0.053117	0.027294	0.019093
1.03e-16	1.35e-16	7.13e-17
0.062476	0.065215	0.054934
2.70e-16	1.86e-16	4.28e-16
0.097268	0.115669	0.086085
2.48e-16	2.72e-16	2.35e-16
0.060385	0.028561	0.019968
0.036754	0.045865	0.042053
1.11e-16	7.42e-17	4.50e-17
0.105129	0.105256	0.096116
2.45e-16	4.72e-16	2.44e-16
0.093227	0.095061	0.073732
3.22e-16	3.57e-16	3.80e-16
0.053585	0.020531	0.008509
1.68e-17	8.45e-17	2.47e-17
0.041575	0.026067	0.061419
1.33e-16	1.89e-16	3.51e-16
0.164736	0.306086	0.242287
1.86e-16	2.21e-16	2.69e-16
0.147944	0.130425	0.155474

Table 5.1: HSH of bunny in different rotations. The highest degree of HSH $K = 8$. (To be continued.)

Bunny 1	Bunny 2	Bunny 3
3.42e-16	3.08e-16	2.56e-16
0.070811	0.035231	0.024339
0.057386	0.068294	0.079115
4.29e-17	6.61e-17	4.54e-17
0.089229	0.166505	0.13794
1.86e-16	2.76e-16	2.04e-16
0.135417	0.144117	0.114726
2.17e-16	3.59e-16	3.30e-16
0.104316	0.0908	0.068864
3.66e-16	3.63e-16	2.55e-16
0.074985	0.030685	0.013303

Table 5.2: (Continue) HSH of bunny in different rotations. The highest degree of HSH $K = 8$.

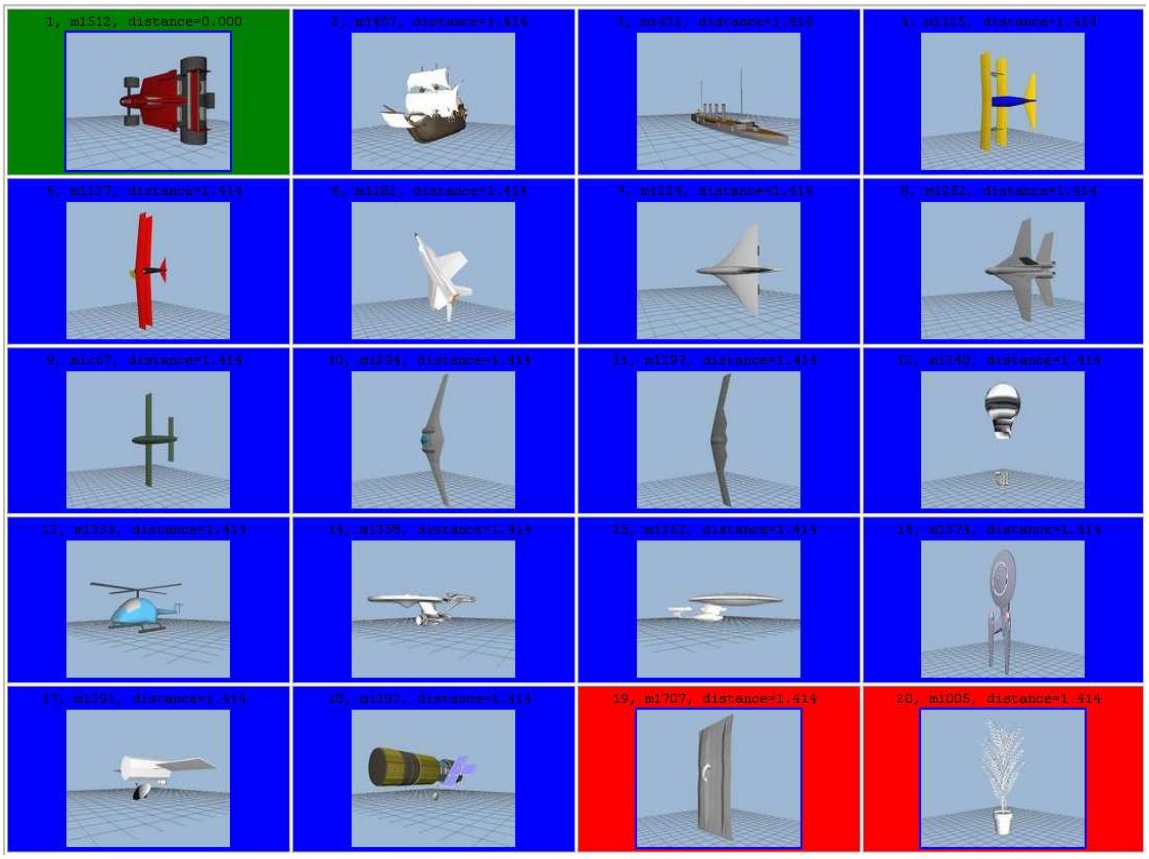

Figure 5.15: An input model and its top 19 matched models. The upper left with green frame is the input model, while the others are retrieved from database. Retrieved models with blue frame are in the same class as the input model, while those with red frame are not.

CHAPTER 6

CONCLUSION AND FUTURE WORK

6.1 Surface Construction

In this dissertation we proposed a generalized marching cubes method for isosurface construction. Existing MC methods do not allow cell vertices whose sample values equal threshold, or zero cell vertices. Modifying sample values at such vertices may introduce problems including topological changes, representation error and preference on positive or negative values. The proposed ZMC method allows zero values to prevail cell vertices after thresholding. It constructs an isosurface by exploring cycles in cells. Comparing with existing MC methods, the proposed method has the following advantages. It best preserves the original topology and improves representation accuracy of isosurfaces that pass cell vertices, since it does not modify sample values. And it avoids enumerating a large number of cases introduced by zero cell vertices. The simulation results show that ZMC method preserves topology better than existing MC methods on zero cell vertices and some non-manifold surfaces. And the efficiency of ZMC method is comparable to that of existing MC methods in constructing isosurfaces. The ZMC program along with the experimental data is available in [45].

To produce smoother or more accurate isosurfaces, future research includes interpolating nonplanar polygonal patches or fitting them by spline surfaces. It is also desirable to make the ZMC algorithm adaptive to geometric features to reduce the number of triangles and preserve sharp features.

6.2 Shape Classification and Matching

For 3D shape classification, we proposed a new approach based on spherical normal images (SNI). SNI incorporates local features by conformal mapping over a unit sphere and is unique to each shape without ambiguity. We also use spherical harmonics (SH) to facilitate the shape classification process. And we use the SVD method to compute SH offline to shorten the response time of online retrieval. Experimental results show that the proposed method using SNI can discriminate collected shapes very well and performs better than that using spherical curvature images and spherical geometry images. The SNI based method is also robust to mesh resolution and pose variance.

The limit of genus-zero shape is determined by the conformal map over sphere. To apply the SNI method to non-zero genus objects, we need to convert them to genus-zero objects first. Sphere like mesh wrapped onto the original object is a possible solution [34].

For shape classification and matching of general shapes, we proposed a new shape descriptor based on 4D hyperspherical harmonics (HSH). Shape descriptors based on concentric spheres model (CSM) cut a 3D shape along radii, which are ambiguous to components with internal rotation. The proposed 4D HSH descriptor maps a 3D object to a 4D unit sphere without cut. It avoids the ambiguity caused by internal rotation. And we use SVD to compute HSH offline to shorten online retrieval response. Support vector machine (SVM) is used to classify general shapes in Princeton Shape Benchmark [70]. Experiments show that the 4D HSH shape descriptor performs better than CSM descriptor at the same vector length on the preclassified shape set. As for shape matching, the 4D HSH shape descriptor retrieves similar shapes in the same class as the input shape successfully. And we proposed weighted distance using classification results. The 4D HSH shape descriptor with weighted distance demonstrates shape matching improvement by 37%.

The limit of the proposed 4D HSH method lies in the complexity of our SVD method to compute 4D HSH. The complexity grows quickly with regard to grid size and highest order of HSH. Thus it limits the length of shape descriptor, which is important to improve shape discriminative power.

In the future we would find new method to compute 4D HSH with less complexity so that longer shape descriptors can be used in shape classification and matching. We also want to try new geometric features or combine existing shape descriptors to improve classification and matching performance.

APPENDIX A

PROCEDURE TO SOLVE ZERO EDGE CASES

To distinguish case 4, 8, 11 and 12, we define a character function T_i, $i = 4, 8, 11$ and 12, which gives non-zero value only to the corresponding case respectively. Let x, y be the sample values besides a zero edge,

$$T_4(F) = \begin{cases} xy \cdot sign(x) & xy > 0 \\ 0 & xy \leq 0 \end{cases}, \tag{A.1}$$

$$T_8(F) = \begin{cases} x + y & xy = 0 \\ 0 & xy \neq 0 \end{cases}, \tag{A.2}$$

$$T_{11}(F) = \begin{cases} \max(x, y)/\min(x, y) & xy < 0 \\ 0 & xy \geq 0 \end{cases}, \tag{A.3}$$

$$T_{12}(F) = \begin{cases} 1 & |x| + |y| = 0 \\ 0 & |x| + |y| \neq 0 \end{cases} \tag{A.4}$$

Case 4, 8 and 11

Consider the combinations of case 4, 8 and 11 first, i.e. $T_{12}(A) + T_{12}(B) = 0$, where A, B are incident on a zero edge α. If A is of case 4 or 8, only α may apply according to Fig. 2.9. We need α to separate positive and negative cell vertices in A, B when B is of case 4 or 8 with a different sign from A,

$$\begin{aligned} S_A(\alpha) = &\{A, B | T_4(A)T_4(B) < 0\} \\ &\cup \{A, B | T_4(A)T_8(B) < 0\} \\ &\cup \{A, B | T_8(A)T_4(B) < 0\} \\ &\cup \{A, B | T_8(A)T_8(B) < 0\}. \end{aligned} \tag{A.5}$$

If A is of case 11, only β or γ applies according to Fig. 2.9. By definition, β is used to separate a positive cell vertex from the rest of A when B is of case 4 or 8 with a negative sign, or of case 11 when the product of positive samples is less than that of negative ones,

$$
\begin{aligned}
S_A(\beta) = &\{A, B | T_{11}(A) \neq 0, T_4(B) < 0\} \\
&\cup \{A, B | T_{11}(A) \neq 0, T_8(B) < 0\} \\
&\cup \{A, B | 0 < T_{11}(A) T_{11}(B) < 1\}.
\end{aligned} \tag{A.6}
$$

Similarly, γ is used to separate a negative cell vertex from the rest of A when B is of case 4,8 with a positive sign, or of case 11 when the product of positive samples is no less than that of negative ones,

$$
\begin{aligned}
S_B(\gamma) = &\{A, B | T_{11}(A) \neq 0, T_4(B) > 0\} \\
&\cup \{A, B | T_{11}(A) \neq 0, T_8(B) > 0\} \\
&\cup \{A, B | T_{11}(A) T_{11}(B) \geq 1\}.
\end{aligned} \tag{A.7}
$$

To get the results in Fig. 2.10, we enumerate all the combinations of case 4, 8, and 11 and solve $S_A(\alpha)$, $S_A(\beta)$ and $S_A(\gamma)$ using equation (A.5), (A.6) and (A.7).

Case 12

Then consider the combinations with case 12, i.e $T_{12}(A)+T_{12}(B) \neq 0$. If only B is of case 12, i.e. $T_{12}(A) = 0, T_{12}(B) \neq 0$, we search along the direction vertical to α for the next cell face C that is not of case 12. We treat cell vertices besides zero edges α, δ adjacent, to solve α, β, and γ similar to equation (A.5) $\sim$ (A.7). If A is of case 4 or 8, only α or δ may apply according to Fig. 2.9. Either α or δ is chosen to separate positive and negative cell vertices in A, C when C is of case 4 or 8 with a different sign from A. Subdividing $S_A(\alpha)$ into two parts and replacing B with C, we have

$$
\begin{aligned}
S_A^*(\alpha) = &\{A, C | T_4(A) T_4(C) < 0,\ |T_4(A)| < |T_4(C)|\} \\
&\cup \{A, C | T_8(A) T_8(C) < 0,\ |T_8(A)| < |T_8(C)|\} \\
&\cup \{A, C | T_8(A) T_4(C) < 0\},
\end{aligned} \tag{A.8}
$$

$$
\begin{aligned}
S^*_C(\delta) = &\{A, C | T_4(A)T_4(C) < 0,\ |T_4(A)| \geq |T_4(C)|\} \\
&\cup \{A, C | T_8(A)T_8(C) < 0,\ |T_8(A)| \geq |T_8(C)|\} \\
&\cup \{A, C | T_4(A)T_8(C) < 0\},
\end{aligned} \tag{A.9}
$$

where we choose α when the absolute value of the product of sample values besides the zero edge in A is less than that in C, or when A is of case 8 and C is of case 4. If A is of case 11, $S^*_A(\beta)$ and $S^*_A(\gamma)$ can be directly derived by replacing B with C in $S_A(\beta), S_A(\gamma)$ of equation (A.6), (A.7) respectively. If A is of case 12, i.e. $T_{12}(A) \neq 0$, we search in both directions vertical to α for the next two cell faces not of case 12. Without loosing generality, let $T_{12}(B) + T_{12}(D) = 0$, $S_A(\alpha)$ can be computed based on Property 1 as $S_A(\alpha) = S_B(\alpha)$.

To get the result in Fig. 2.11, we enumerate all the configurations with a cell face of case 12, and solve $S^*_A(\alpha)$ and $S^*_C(\delta)$ using equation (A.6) $\sim$ (A.9).

APPENDIX B

PROOF OF THE THEOREM OF VERTEX DEGREE

Firstly, it is easy to verify the degree of a surface vertex that is not zero cell vertex is two, since it is shared by two cell faces, in each of which one patch edge is connected to the vertex. And the degree of surface vertex in Fig. 2.11 is either zero or two.

Secondly, we show that the degree of surface vertex is at most two for the cases with zero cell vertices in Fig. 2.7(a) and Fig. 2.10. In Fig. 2.7(a), the only possibility for the degree of surface vertex to reach three is at zero cell vertices with three adjacent cell faces. However, if one zero cell vertex connects to three patch edges like case 5 or 9, it will cause a contradiction in which the cell vertices at two sides of a patch edge are of the same sign. So the degree of surface vertex is at most two in cases in Fig. 2.7(a). In Fig. 2.10, we only need to verify the degree of zero cell vertices that possibly connect more than one patch edge is at most two. Such zero cell vertices, called *multi-edge vertices* for convenience, exist in sub-case 4.d, 11.b, 11.c.1, 11.c.2, 8.e, 8.g and 8.h. From cases 2 and 7 in Fig. 2.7(a), a zero cell vertex connects to no patch edge if its two adjacent cell vertices are of the same sign. So a multi-edge vertex connects to no patch edge in its third adjacent cell face (not displayed) in sub-cases 11.c.1, 11.c.2, 8.e or 8.g in Fig. 2.10. Since only two cell vertices are not known in Fig. 2.10, we get the degree of the multi-edge vertex is two by enumerating nine combinations of the two unknown cell vertices in the sub-cases 4.d, 11.b and 8.h. So the degree of surface vertex is at most two in cases in Fig. 2.10.

Finally we show that the degree of a zero cell vertex is not one. We only need to check zero cell vertices that connect only one patch edge in Fig. 2.7(a) and Fig. 2.10, connect at least one patch edge in other adjacent cell faces. Such zero cell vertex is called *single-edge* vertex for convenience. From case 5 and 9 of Fig. 2.7(a), a zero cell vertex connects to only one patch edge on one cell face if its two adjacent cell vertices are of different signs. Similarly it connects to at least one patch edge in its other adjacent cell faces, if its third adjacent cell vertex (not displayed) is positive or negative. If its third adjacent cell vertex is a zero cell vertex, only two other un-

known cell vertices (not displayed) that affect its degree are left. We get the degree of a single-edge vertex is two by enumerating nine combinations of the two unknown cell vertices. In Fig. 2.10, the degree of a zero cell vertex in sub-cases 4.c, 4.e, 11.e.1, 11.e.2 is two since its two adjacent cell vertices are of different signs. Since only two unknown vertices (not displayed) are left in Fig. 2.10, by enumerating nine combinations of the two unknown cell vertices, we get the degree of the single-edge vertex is two in sub-case 4.d, 11.b, 11.d, 8.e, 8.g and 8.h.

In conclusion, the degree of surface vertex in one cell by the case rules of bilinear interpolation and zero edge is either zero or two.

APPENDIX C

COMPLEXITY OF ONLINE COMPUTING FOR SPHERICAL HARMONICS COEFFICIENTS

Let sample surface values $R = (r(\theta_1, \phi_1), \cdots, r(\theta_i, \phi_i), \cdots, r(\theta_N, \phi_N))$, the coefficients $C = (C_0^0, C_1^{-1}, C_1^0, C_1^1, \cdots, C_K^{K-1}, C_K^K)$ and the matrix of spherical harmonics,

$$Y = \begin{pmatrix} Y_0^0(\theta_1, \phi_1) & Y_1^{-1}(\theta_1, \phi_1) & \cdots & Y_K^K(\theta_1, \phi_1) \\ Y_0^0(\theta_2, \phi_2) & Y_1^{-1}(\theta_2, \phi_2) & \cdots & Y_K^K(\theta_2, \phi_2) \\ \cdots & \cdots & \ddots & \cdots \\ Y_0^0(\theta_i, \phi_i) & Y_1^{-1}(\theta_i, \phi_i) & \cdots & Y_K^K(\theta_i, \phi_i) \\ \cdots & \cdots & \ddots & \cdots \\ Y_0^0(\theta_N, \phi_N) & Y_1^{-1}(\theta_N, \phi_N) & \cdots & Y_K^K(\theta_N, \phi_N) \end{pmatrix}. \tag{C.1}$$

From equation (4.9) we get $R^T = YC^T$, which is,

$$C^T = Y^{-1}R^T, \tag{C.2}$$

where Y^{-1} is the pseudo inverse matrix of Y.

Once the positions (θ_i, ϕ_i) of the sampling points R are pre-known (i.e. latitude θ and longitude ϕ are distributed uniformly), and the number of sample points N and the highest order of spherical harmonics K are fixed (normally $N >> (K+1)^2$), Y^{-1} can be computed as an over-determined system by SVD method offline once for all. The online computation, with regard to R of different 3D shapes, involves only complex matrix multiplication in $O(N)$. Note that R must be sampled at the fixed (θ_1, ϕ_1), $\cdots$, (θ_i, ϕ_i), $\cdots$, (θ_N, ϕ_N), instead of arbitrary points. And the fixed sampling points can be computed in $O(N)$.

On the other hand, FFT method estimates spherical harmonic coefficients using the sampling theorem [66]:

Let $f \in L^2(S^2)$ have bandwidth B. Then for $0 \leq |m| \leq l < B$,

$$\hat{f}(l,m) = \frac{\sqrt{2\pi}}{2B} \sum_{j=0}^{2B-1} \sum_{k=0}^{2B-1} a_j^{(B)} f(\theta_j, \phi_k) e^{-im\phi_k} P_l^m(\cos\theta_j), \tag{C.3}$$

where P_l^m is the associate Legendre function, the sample points are chosen from the equiangular grid: $\theta_j = \pi(2j+1)/4B$, $\phi_k = 2\pi k/2B$, and the weights $a_j^{(B)}$ play a role analogous to the $\sin\theta$ factor in the integrals.

In terms of online computation, FFT method involves multiplication and addition proportional to the number of sampling points N because all except the sample surface value $f(\theta_j, \phi_k)$ in (C.3) can be computed offline.

In sum, the complexity online computation is approximated as $O(N)$ for both SVD and FFT methods.

APPENDIX D

COMPUTING 4D HYERSPHERICAL HARMONICS (HSH) COEFFICIENTS

The process to compute 4D HSH coefficients $C^m_{\lambda,l}$ is very similar to that of coefficients C^m_l of 3D SH. We just outline the formulas. Let sample voxel values $R = (r(\theta_1, \phi_1, \theta_{01}), \cdots, r(\theta_i, \phi_i, \theta_{0i}), \cdots, r(\theta_N, \phi_N, \theta_{0N}))$, the coefficients $C = (C^0_{0,0}, C^0_{1,0}, C^{-1}_{1,1}, C^0_{1,1}, C^1_{1,1}, \cdots, C^{K-1}_{K,K}, C^K_{K,K})$ and the matrix of spherical harmonics,

$$Y = \begin{pmatrix} Y^0_{0,0}(\theta_1, \phi_1, \theta_{01}) & Y^0_{1,0}(\theta_1, \phi_1, \theta_{01}) & \cdots & Y^K_{K,K}(\theta_1, \phi_1, \theta_{01}) \\ Y^0_{0,0}(\theta_2, \phi_2, \theta_{02}) & Y^0_{1,0}(\theta_2, \phi_2, \theta_{02}) & \cdots & Y^K_{K,K}(\theta_2, \phi_2, \theta_{02}) \\ \cdots & \cdots & \ddots & \cdots \\ Y^0_{0,0}(\theta_i, \phi_i, \theta_{0i}) & Y^0_{1,0}(\theta_i, \phi_i, \theta_{0i}) & \cdots & Y^K_{K,K}(\theta_i, \phi_i, \theta_{0i}) \\ \cdots & \cdots & \ddots & \cdots \\ Y^0_{0,0}(\theta_N, \phi_N, \theta_{0N}) & Y^0_{1,0}(\theta_N, \phi_N, \theta_{0N}) & \cdots & Y^K_{K,K}(\theta_N, \phi_N, \theta_{0N}) \end{pmatrix}. \tag{D.1}$$

From equation (5.11) we get $R^T = YC^T$, which is,

$$C^T = Y^{-1}R^T, \tag{D.2}$$

where Y^{-1} is the pseudo inverse matrix of Y.

We sample $(\theta_i, \phi_i, \theta_{0i})$ uniformly over 4D unit sphere, with $\theta_i \in [0, \pi]$, $\phi_i \in [0, 2\pi]$, and $\theta_{0i} \in [0, \pi]$. Another way to sample $(\theta_i, \phi_i, \theta_{0i})$ is to convert voxels from Cartesian coordinates to Polar coordinates directly using equation (5.5).

We use Mathematica function $SphericalHarmonicY$ to compute 3D spherical harmonics, and get 4D hyperspherical harmonics using equation (5.7), (5.8) and (5.9) [95].

For N sample points and the highest degree of HSH K, the size of matrix Y is $N \times \frac{(K+1)(K+2)(2K+3)}{6}$. Normally $N >> \frac{(K+1)(K+2)(2K+3)}{6}$, we need to compute Y^{-1} by singular value decomposition (SVD). For example, for a $(\theta_i, \phi_i, \theta_{0i})$ grid of size $20 \times 20 \times 20$ and $K = 8$, the size of Y is 8000×285. This step can be com-

pleted offline once for all hyperspherical functions, which is sampled at fixed position $(\theta_i, \phi_i, \theta_{0i})$.

REFERENCES

[1] W. E. Lorensen and H. E. Cline, "Marching cubes: A high-resolution 3D surface construction algorithm," in *Proceedings of the 14th annual conference on computer graphics and interactive techniques*, 1987, pp. 163–169.

[2] E. V. Chernyaev, "Marching cubes 33: Construction of topologically correct isosurfaces," CERN, Geneva, Switzerland, Tech. Rep. CN/95-17, 1995.

[3] "Spherical harmonic," MathWorld. [Online]. Available: http://mathworld.wolfram.com/SphericalHarmonic.html

[4] J. Vesanto and E. Alhoniemi, "Clustering of the Self-Organizing Map," *IEEE Transactions on Neural Networks*, vol. 11, pp. 586–600, 2000.

[5] R. Osada, T. Funkhouser, B. Chazelle, and D. Dobkin, "Shape distributions," *ACM Transactions on Graphics*, vol. 21, pp. 807–832, 2002.

[6] D. V. Vranić, "3D model retrieval," Ph.D. dissertation, University of Leipzig, 2004.

[7] M. Kazhdan, T. Funkhouser, and S. Rusinkiewicz, "Rotation invariant spherical harmonic representation of 3D shape descriptors," in *Eurographics Symposium on Geometry Processing(2003)*, 2003, pp. 156–165.

[8] E. Osuna, R. Freund, and F. Girosi, "Support vector machines: Training and applications," Artificial Intelligence Laboratory, Massachusetts Institute of Technology, Tech. Rep. AIM-1602, 1997. [Online]. Available: citeseer.ist.psu.edu/osuna97support.html

[9] G. M. Nielson and B. Hamann, "The asymptotic decider: Resolving the ambiguity in marching cubes," in *Proceedings of Visualization '91*, 1991, pp. 29–38.

[10] B. K. Nataranjan, "On generating topologically consistent isosurfaces from uniform samples," *The Visual Computer*, vol. 11, no. 1, pp. 52–62, 1994.

[11] S. V. Matveyev, "Approximation of isosurface in the marching cubes: Ambiguity problem," in *IEEE Visualization*, 1994, pp. 288–292.

[12] G. M. Nielson, "On marching cubes," *IEEE Transaction on Visualization and Computer Graphics*, vol. 9, no. 3, pp. 283–297, 2003.

[13] A. Lopes and K. Brodlie, "Improving the robustness and accuracy of the marching cubes algorithm for isosurfacing," *IEEE Transaction on Visualization and Computer Graphics*, vol. 9, no. 1, pp. 16–29, 2003.

[14] H. Theisel, "Exact isosurfaces for marching cubes," *Computer Graphics Forum*, vol. 21, no. 1, pp. 19–31, 2002.

[15] L. P. Kobbelt, M. Botsch, U. Schwanecke, and H.-P. Seidel, "Feature sensitive surface extraction from volume data," in *ACM SIGGRAPH 2001*, 2001, pp. 57–66.

[16] T. Ju, F. Losasso, S. Schaefer, and J. Warren, "Dual contouring of hermite data," in *29th annual conference on Computer graphics and interactive techniques*, 2002, pp. 339–346.

[17] R. Shekhar, E. Fayyad, R. Yagel, and J. F. Cornhill, "Octree-based decimation of marching cubes surfaces," in *IEEE Visualization 1996*, 1996, pp. 335–342.

[18] R. Westermann, L. Kobbelt, and T. Ertl, "Real-time exploration of regular volume data by adaptive reconstruction of iso-srufaces," *The Visual Computer*, vol. 15, no. 2, pp. 100–111, 1999.

[19] J. Wilhelms and A. V. Gelder, "Octrees for faster isosurface generation," *ACM Transactions on Graphics*, vol. 11, no. 3, pp. 201–227, 1992.

[20] C. Montani, R. Scateni, and R. Scopigno, "A modified lookup table for implicit disambiguation of marching cubes," *The Visual Computer*, vol. 10, no. 6, pp. 353–355, 1994.

[21] ——, "Discretized marching cubes," in *Proceeding of the Visualization '94.* Congress, 1994, pp. 281–287.

[22] A. Cuno, C. Esperanca, A. Oliveira, and P. R. Cavalcanti, "Fast polygonization of variational implicit surfaces," in *XVII Brazilian Symposium on Computer Graphics and Image Processing*, 2004, pp. 258–265.

[23] A. V. Gelder and J. Wilhelms, "Topological considerations in isosurface generation," *ACM Transactions on Graphics*, vol. 13, no. 4, pp. 337–375, 1994.

[24] J. Bloomenthal and K. Ferguson, "Polygonization of non-manifold implicit surfaces," in *ACM SIGGRAPH 1995*, 1995, pp. 309–316.

[25] A. Hubeli and M. Gross, "Multiresolution methods for nonmanifold models," *IEEE Transactions on Visualization and Computer Graphics*, vol. 7, no. 3, pp. 207–221, 2001.

[26] H.-C. Hege, M. Seebas, D. Stalling, and M. Zockler, "A generalized marching cubes algorithm based on non-binary classifications," Zuse Institute Berlin (ZIB), Tech. Rep. SC 97-05, 1997.

[27] S. Yamazaki, K. Kase, and K. Ikeuchi, "Non-manifold implicit surfaces based on discontinuous implicitization and polygonization," in *Geometric Modeling and Processing - Theory and Applications*, 2002, pp. 138–147.

[28] X. Han, C. Xu, and J. Prince, "A topology preserving level set method for geometric deformable models," *IEEE Transactions on Pattern Analysis and Machine Intelligence*, vol. 25, no. 6, pp. 755–768, June 2003.

[29] D. C. Banks and S. Linton, "Counting cases in marching cubes: Toward a generic algorithm for producing substitopes," in *IEEE Visualization 2003*, 2003, pp. 51–58. [Online]. Available: http://www.dcs.st-and.ac.uk/research/publications/BL03.php

[30] "Eulerian circuit," MathWorld. [Online]. Available: http://mathworld.wolfram.com/EulerianCircuit.html

[31] J. W. Tangelder and R. C. Veltkamp, "A survey of content based 3D shape retrieval methods," in *Proceedings Shape Modeling International*, 2004, pp. 145–156.

[32] R. J. Campbell and P. J. Flynn, "A survey of free-form object representation and recognition techniques," *Computer Vision and Image Understanding*, vol. 81, pp. 166–210, 2001.

[33] N. Iyer, K. Lou, S. Jayanti, K. Y., and K. Ramani, "Three dimensional shape searching: State-of-the-art review and future trends," *Computer Aided Design*, 2004.

[34] M. Herbert, K. Ikeuchi, and H. Delingette, "A spherical representation for recognition of free-form surfaces," *IEEE Transactions on Pattern Analysis and Machine Intelligence*, vol. 17, pp. 681–690, 1995.

[35] J. Li, "Three dimensional shape modeling: Segmentation, reconstruction and registration," Ph.D. dissertation, Electrical Engineering, the University of Michigan, 2002.

[36] D. Saupe and D. V. Vranić, "3D model retrieval with spherical harmonics and moments," in *Proceedings of the DAGM 2001*, B. Radig and S. Florczyk, Eds., 2001, pp. 392–397.

[37] D. V. Vranić, "An improvement of rotation invariant 3D shape descriptor based on functions on concentric spheres," in *ICIP 2003*, vol. 3, 2003, pp. 757–760.

[38] D.-Y. Chen, X.-P. Tian, Y.-T. Shen, and M. Ouhyoung, "On visual similarity based 3D model retrieval," in *Eurographics Computer Graphics Forum*, vol. 22, 2003, pp. 223–233.

[39] X. Gu, S. J. Gortler, and H. Hoppe, "Geometry Images," in *Proceedings of SIGGRAPH*, 2002, pp. 355–361.

[40] H. Laga, H. Takahashi, and M. Nakajima, "Geometry image matching for similarity estimation of 3D shapes," in *Proceedings of the Computer Graphics International (CGI'04)*, 2004, pp. 490–496.

[41] H.-s. Wong, K. K. Cheung, and H. H. Ip, "3D head model classification by evolutionary optimization of the Extended Gaussian Image representation," *Pattern Recognition*, vol. 37, pp. 2307–2322, 2004.

[42] J. Corney, H. Rea, D. Clark, J. Pritchard, M. Breaks, and R. MacLeod, "Coarse filters for shape matching," *IEEE Computer Graphics and Applications*, vol. 22, no. 3, pp. 65–74, 2002.

[43] S. Biasotti, S. Marini, M. Mortara, and G. Patané, "An overview on properties and efficacy of topological skeletons in shape modeling," in *SMI '03: Proceedings of the Shape Modeling International 2003*. Washington, DC, USA: IEEE Computer Society, 2003, p. 245.

[44] "Topology," MathWorld. [Online]. Available: http://mathworld.wolfram.com/Topology.html

[45] S. Liu and J. Li, "Enumerating all the marching cubes cases with zero cell vertices," SECS in Oakland University. [Online]. Available: http://www.secs.oakland.edu/~sliu2/MC/mc.htm

[46] T. Lewiner, H. Lopes, A. W. Vieira, and G. Tavares, "Efficient implementation of marching cubes' cases with topological guarantees," *Journal of Graphics Tools*, vol. 8, no. 2, pp. 1–15, 2003.

[47] R. Malladi, J. A. Sethian, and B. C. Vemuri, "Shape modeling with front propagation: A level set approach," *IEEE Transactions on Pattern Analysis and Machine Intelligence*, vol. 17, no. 2, pp. 158–175, Feb 1995.

[48] C. Baillard, C. Barillot, and P. Bouthemy, "Robust adaptive segmentation of 3D medical images with level sets," INRIA, Tech. Rep. RR-4071, 2000.

[49] A. Dempster, N. Laird, and D. Rubin, "Maximum likelihood from incomplete data via the EM algorithm," *Journal of Royal Statistical Society*, vol. 3, pp. 1–38, 1976.

[50] A. Tsai, W. Wells, S. Warfield, and A. Willsky, "Level set methods in an EM framework for shape classification and estimation," in *MICCAI (1) 2004*, 2004, pp. 1–9.

[51] P. Masson and W. Pieczynski, "SEM algorithm and unsupervised statistical segmentation of satellite images," *IEEE Transaction on Geoscience and Remote Sensing*, vol. 31, no. 3, pp. 618–633, 1993.

[52] C. Ciofolo, C. Barillot, and P. Hellier, "Combining fuzzy logic and level set methods for 3D MRI brain segmentation," in *IEEE International Symposium on Biomedical Imaging (ISBI)*, 2004, pp. 161–164.

[53] P. Lin, C.-X. Zeng, Y. Yang, and J.-W. Gu, "Statistical model based on level set method for image segmentation," in *The Fourth International Conference on Computer and Information Technology*, 2004, pp. 143–148.

[54] "Lung Image Database Consortium (LIDC) Materials," National Cancer Institute. [Online]. Available: http://imaging.cancer.gov/reportsandpublications/ReportsandPresentations/LungImaging

[55] C.-C. Ho, P.-L. Lee, Y.-Y. Chuang, B.-Y. Chen, and M. Ouhyoung, "Cubical marching squares: Adaptive feature preserving surface extraction from volume data," in *EUROGRAPHICS*, vol. 24, 2005.

[56] M. Novotni and R. Klein, "A geometric approach to 3D object comparison," in *Proceedings of the 5th ACM SIGMM international workshop on Multimedia information retrieval*, 2003, pp. 39–45.

[57] D. V. Vranić, D. Saupe, and J. Richter, "Tools for 3D-object retrieval: Karhunen-Loeve transform and spherical harmonics," in *Proceedings of the IEEE 2001 Workshop Multimedia Signal Processing*, J.-L. Dugelay and K. Rose, Eds., 2001, pp. 293–298.

[58] S. Haker, S. Angenent, A. Tannenbaum, R. Kikinis, G. Sapiro, and M. Halle, "Conformal surface parameterization for texture mapping," *IEEE Transactions on Visualization and Computer Graphics*, vol. 6, pp. 240–251, 2000.

[59] H. Hoppe, T. DeRose, and T. Duchamp, "Multiresolution analysis of arbitrary meshes," in *Computer Graphics (SIGGRAPH'95 Proceedings)*, 1995, pp. 173–182.

[60] X. Gu and S. T. Yau, "Computing conformal structures of surfaces," in *Communication of Information and Systems*, vol. 2, 2002, pp. 121–146.

[61] C. Gotsman, X. Gu, and A. Sheffer, "Fundamentals of spherical parameterization for 3D meshes," *ACM Transactions on Graphics*, vol. 22, pp. 358–363, 2003.

[62] T. Tasdizen and R. Whitaker, "Geometric surface processing via normal maps," *ACM Transactions on Graphics*, vol. 22, no. 4, pp. 1012–1033, Oct. 2003.

[63] K. Ikeuchi and M. Hebert, "Spherical representations: from EGI to SAI," Computer Science Department, Carnegie Mellon University, Tech. Rep. CMU-CS-95-197, 1995.

[64] E. Praun and H. Hoppe, "Spherical parameterization and remeshing," in *Proceedings of ACM SIGGRAPH*, 2003, pp. 340–349.

[65] R. B. Schudy and D. H. Ballard, "Towards an anatomical model of heart motion as seen in 4-D cardiac ultrasound data," in *Proceedings of the 6th Conference on Computer Applications in Radiology and Computer-Aided Analysis of Radiological Images*, 1979.

[66] D. M. J. Healy, D. Rockmore, P. J. Kostelec, and S. S. B. More, "FFTs for the 2-sphere - improvements and variations," *The Journal of Fourier Analysis and Applications*, vol. 9, pp. 341–385, 2003.

[67] D. Zhang and M. Hebert, "Multi-scale classification of 3D objects," Robotics Institute, Carnegie Mellon University, Tech. Rep. CMU-RI-TR-96-39, 1996.

[68] H. Hoppe, "Progressive meshes," in *SIGGRAPH 96*, 1996, pp. 99–108.

[69] "3D Database," Signal Analysis and Machine Perception Laboratory (SAMPL). [Online]. Available: http://sampl.eng.ohio-state.edu/~sampl/data/3DDB/Models/index.htm

[70] P. Shilane, P. Min, M. Kazhdan, and T. Funkhouser, "Princeton Shape Benchmark." [Online]. Available: http://shape.cs.princeton.edu/benchmark/

[71] D. V. Vranić, "3D MODEL DATABASE." [Online]. Available: http://merkur01.inf.uni-konstanz.de/CCCC/dbsel.html

[72] "The Stanford 3D Scanning Repository," Stanford University Computer Graphics Laboratory. [Online]. Available: http://www-graphics.stanford.edu/data/3Dscanrep/

[73] "SOM toolbox for Matlab," SOM Toolbox team in CIS HELSINKI UNIVERSITY OF TECHNOLOGY. [Online]. Available: http://www.cis.hut.fi/projects/somtoolbox/

[74] M. M. Kazhdan, "Shape representations and algorithms for 3D model retrieval," Ph.D. dissertation, The Department of Computer Science in Princeton University, 2004.

[75] J. Huang, R. Yagel, V. Filippov, and Y. Kurzion, "An accurate method for voxelizing polygon meshes," in *IEEE Symposium on Volume Visualization*, 1998, pp. 119–126. [Online]. Available: citeseer.ist.psu.edu/article/huang98accurate.html

[76] M. W. Jones, "The production of volume data from triangular meshes using voxelisation," *Computer Graphics Forum*, vol. 15, no. 5, pp. 311–318, 1996.

[77] W. J. Schroeder, W. E. Lorensen, and S. Linthicum, "Implicit modeling of swept surfaces and volumes," in *VIS '94: Proceedings of the conference on Visualization '94*. Los Alamitos, CA, USA: IEEE Computer Society Press, 1994, pp. 40–45.

[78] F. Dachille and A. Kaufman, "Incremental triangle voxelization," in *Graphics Interface 2000*, May 2000, pp. 205–212. [Online]. Available: citeseer.ist.psu.edu/dachille00incremental.html

[79] F. S. Nooruddin and G. Turk, "Simplification and repair of polygonal models using volumetric techniques," *IEEE Transactions on Visualization and Computer Graphics*, vol. 9, no. 2, pp. 191–205, 2003.

[80] T. Funkhouser, P. Min, M. Kazhdan, J. Chen, A. Halderman, and D. Dobkin, "A search engine for 3D models," *ACM Transactions on Graphics*, vol. 22, pp. 83–105, 2003.

[81] M. Murata and S. Hashimoto, "Interactive environment for intuitive understanding of 4d object and space," in *International Conference on Multimedia Modeling*, 2000, pp. 383–401.

[82] K. A. Mitchell and R. G. Littlejohn, "Derivation of planar three-body hyperspherical harmonics from monopole harmonics," *Phys. Rev. A*, vol. 56, no. 1, pp. 83–99, Jul 1997.

[83] J. Avery, *Hyperspherical Harmonics and Generalized Sturmians*. Dordrecht, Netherlands: Kluwer Academic Publishers, 2000.

[84] A. Matheny and D. B. Goldgof, "The use of three- and four-dimensional surface harmonics for rigid and nonrigid shape recovery and representation," *IEEE Trans. Pattern Anal. Mach. Intell.*, vol. 17, no. 10, pp. 967–981, 1995.

[85] A. V. Meremianin, "Multipole expansions in four-dimensional hyperspherical harmonics," *Journal of Physics A Mathematical General*, vol. 39, pp. 3099–3112, Mar. 2006.

[86] M. Ouhyoung, D.-Y. Chen, and J.-S. Yeh, "NTU 3D model benchmark." [Online]. Available: http://3d.csie.ntu.edu.tw/~dynamic/benchmark/index.html

[87] B. E. Boser, I. Guyon, and V. Vapnik, "A training algorithm for optimal margin classifiers," in *Computational Learning Theory*, 1992, pp. 144–152. [Online]. Available: citeseer.ist.psu.edu/boser92training.html

[88] V. N. Vapnik, *The nature of statistical learning theory*. New York, NY, USA: Springer-Verlag New York, Inc., 1995.

[89] S. Canu, Y. Grandvalet, V. Guigue, and A. Rakotomamonjy, "SVM and kernel methods Matlab toolbox," Perception Systemes et Information, INSA de Rouen, Rouen, France, 2005. [Online]. Available: http://asi.insa-rouen.fr/~arakotom/toolbox/index.html

[90] R. Kohavi and B. Becker, "UCI adult database," also known as Census Income Database. [Online]. Available: http://mlearn.ics.uci.edu/MLSummary.html

[91] T. Joachims, "Learning to classify text using support vector machines," Ph.D. dissertation, Cornell University, 2002.

[92] ——, *Making large-Scale SVM Learning Practical. Advances in Kernel Methods - Support Vector Learning*. MIT Press, 1999.

[93] ——, "SVM^{Light}," an implementation of Support Vector Machines (SVMs) in C. [Online]. Available: http://svmlight.joachims.org/

[94] M. Li, "Confidence-based classifier design and its applications," Ph.D. dissertation, Oakland University, 2005.

[95] "Spherical harmonic," Mathematica. [Online]. Available: http://functions.wolfram.com/HypergeometricFunctions/SphericalHarmonicYGeneral/

PUBLICATIONS

[1] Shaojun Liu, Jia Li, and Xiaojun Jing, "Surface Construction using Tricolor Marching Cubes," in *International Conference on Computer Graphics Theory and Applications (GRAPP)*, 2006, pp. 319-324.

[2] Shaojun Liu and Jia Li, "Genus-Zero Shape Classification Using Spherical Normal Image," in *International Conference on Pattern Recognition (ICPR)*, 2006, pp. 126-129.

[3] Shaojun Liu and Jia Li, "Automatic Medical Image Segmentation Using Gradient and Intensity Combined Level Set Method," in *IEEE International Conference of the Engineering in Medicine and Biology Society (EMBS)*, 2006, pp. 3118-3121.

[4] Russel Deter, Jia Li, Wesley Lee, Shaojun Liu, Romeo Roberto, "Quantitative Assessment of Gestational Sac Shape: The Gestational Sac Shape Score," accepted to *Ultrasound in Obstetrics and Gynecology, Jan. 2007.*

[5] Shaojun Liu, Jia Li, "Constructing Topologically Correct Isosurfaces by Zero-Crossing Marching Cubes", submitted to *Computers & Graphcs.*

[6] Weihong Niu, Jia Li, Shaojun Liu, Timothy Talty, "Intra-vehicle UWB Communication Testbed", submitted to *Military Communications Conference (MILCOM) 2007.*